

X-Ray Near-Field Holography: Beyond Idealized Assumptions of the Probe

Dissertation

zur Erlangung des mathematisch-naturwissenschaftlichen

Doktorgrades

„Doctor rerum naturalium”

der Georg-August-Universität Göttingen

im Promotionsprogramm ProPhys

der Georg-August University School of Science (GAUSS)

vorgelegt von

Johannes Hagemann

aus Hildesheim

Göttingen, 2017

Mitglieder des Betreuungsausschusses:

Prof. Dr. Tim Salditt
Institut für Röntgenphysik,
Georg-August-Universität Göttingen

Prof. Dr. Russel Luke
Numerische und Angewandte Mathematik,
Georg-August-Universität Göttingen

Mitglieder der Prüfungskommission:

Referent: Prof. Dr. Tim Salditt
Institut für Röntgenphysik,
Georg-August-Universität Göttingen

1. Korreferent: Prof. Dr. Russel Luke
Numerische und Angewandte Mathematik,
Georg-August-Universität Göttingen

Weitere Mitglieder der Prüfungskommission:

Dr. Klaus Mann Prof. Dr. Stefan Dreizler
Laser Labor Göttingen Institut für Astrophysik,
Georg-August-Universität Göttingen

Prof. Dr. Claus Ropers Prof. Dr. Simone Techert
Institut für IV. Physikalisches Institut, Institut für Röntgenphysik,
Georg-August-Universität Göttingen Georg-August-Universität Göttingen

Tag der mündlichen Prüfung:

16. August 2017

Contents

Abstract	vii
1. Concepts of Near-Field X-ray Phase-Contrast Imaging	1
1.1. On the use of x-rays	1
1.2. Imaging modalities	4
1.3. Propagation and imaging artifacts	7
2. Probe Reconstruction for Holographic X-ray Imaging	13
2.1. Introduction	13
2.2. Experimental setup	15
2.3. MMP - algorithm	17
2.4. Results	19
2.5. Summary and outlook	25
3. The Fluence-Resolution Relationship in Holographic and Coherent Diffractive Imaging	27
3.1. Introduction	27
3.2. Numerical setup	31
3.3. Results	34
3.4. Summary and outlook	38
3.5. Appendix A: Direct back propagation	39
4. Reconstructing Mode Mixtures in the Optical Near Field	43
4.1. Introduction	43
4.2. Simulation model	45
4.3. Algorithm	49
4.4. Numerical experiment	50
4.5. Summary and outlook	54
4.6. Appendix A: Mode reconstructions from noisy measurements	54
4.7. Appendix B: Mode reconstructions from a reduced data set	55
4.8. Appendix C: Influence of the choice of M for reconstruction	58
4.9. Appendix D: Influence of the initial guess of λ_m for reconstruction	59

5. Divide and Update: Towards Single-Shot Object and Probe Retrieval for Near-Field Holography	63
5.1. Introduction	63
5.2. Algorithm	67
5.3. Results	69
5.3.1. Simulated data	69
5.3.2. Experimental data	73
5.4. Discussion and outlook	76
5.5. Appendix A: Simulation for parallel data acquisition scheme	78
5.6. Appendix B: Details of the shearlet suppression	79
6. Summary and Outlook	83
Appendix	85
A. How much Coherence is Needed for Near-Field Imaging?	85
A.1. Coherence model	85
A.2. Numerical simulation	87
A.3. Results	91
A.4. Summary	94
B. Iterative Reconstruction Algorithms	97
C. Matlab Routines	105
C.1. List of Routines	106
C.2. Implementation of RAAR	113
Bibliography	116
Authors Contribution	133
Own publications	135
Danksagung	137
Curriculum Vitae	139

Abstract

The work at hand considers the imperfect, often neglected, aspects of x-ray near-field phase-contrast propagation imaging, or in short: *x-ray near-field holography* (NFH). NFH is a x-ray microscopy technique able to yield high resolution, yet low dose imaging of a wide range of specimen. Derived from wave optical theory, propagation-based imaging methods rely on assumptions for the illuminating wave field. These are for example the assumptions of a perfect plane wave or spherical wave emanating from a point source or monochromaticity. Violation of the point source assumption implies for example at the same time the occurrence of a distorted wave front and a finite degree of coherence, both crucial for NFH. With the advances in x-ray focusing [1], instrumentation [2] and x-ray wave guiding [3, 4], NFH has become of high interest, since the barriers for practical implementation have been overcome. The idea of holography originates from electron microscopy [5] to overcome the lack of high-quality electron lenses. With holography the need for optics between the specimen and detector is circumvented. The drawback, however, is that the measurement obtained at the detector is not a direct image of the specimen under survey but a „propagated version“ of it, the so-called *hologram*. The problem with the optics is replaced by another problem, also referred to as the *phase problem*. The phase problem is caused by the fact that only the intensities of a wave field can be measured but not the phase information. The phase information is crucial for obtaining the image of the specimen and thus needs to be reconstructed. In recent years the methodology [6–9], sometimes also mythology [10], has been developed to reconstruct the specimen from the measured hologram.

For a long time, the standard approach to deal with deviations from the ideal assumptions in real world holography experiments has been to simply ignore these. The prime example for this is the method of the standard flat-field correction.

With the advent of advanced reconstruction schemes this has changed and the effect of the deviations can be taken into account. One of the most successful schemes is currently *ptychography* [11, 12]. With ptychography a simultaneous retrieval of the illumination’s and specimen’s wave field is possible. This has allowed to account for distorted wave fronts, i.e. wave fronts deviating from the ideal spherical

or equivalently plane waves. Ptychography was originally developed for far-field (Fraunhofer-regime) imaging, but it has been recently adapted to near-field imaging [13, 14].

The current work drives this development further by investigating the degrading effects on image quality and by incorporating these in the reconstruction process of NFH measurements.

Chapter 1 presents a further analysis of the non-ideal settings encountered in real experiments.

The main results of this thesis are presented as a compilation of four publications in the following chapters. In Chapter 2 the reconstruction of the full diverging wave front of the nano-focus setup GINIX at the beamline P10 at PETRAIII, DESY is presented. The reconstruction is carried out with two independent near-field-imaging schemes. The results are in good agreement and allow for a full characterization of the focal spot.

Chapter 3 surveys the important question: How many photons are needed to reach a certain resolution? In a numerical experiment, near- and far-field x-ray propagation imaging are compared in terms of their fluence-resolution relationship.

Chapter 4 extends the near-field reconstruction scheme developed in Chapter 2 to include the effects of partially coherent illumination. The scheme is extensively tested in numerical experiments. The results indicate a robust recovery of the modal structure of the illumination, in terms of partially coherent modes. Based on the reconstruction, practical quantities as the coherence length can be computed.

Chapter 5 describes a minimal ptychography algorithm, able to reconstruct illumination and specimen from two measurements. The algorithm has been tested in simulations and on experimental data obtained at the ESRF beamline ID16a.

The thesis closes in Chapter 6 with a summary and outlook.

1. Concepts of Near-Field X-ray Phase-Contrast Imaging

1.1. On the use of x-rays

The goal of microscopy and, in particular for this thesis, hard x-ray microscopy is to provide high resolution, high contrast quantitative images. X-ray microscopy has the potential for high resolution due to small wave length. With the penetration power of hard x-rays the internal structure of a specimen is accessible. In combination with computed tomography the internal 3d structure of a specimen can be visualized [15, 16]. But there are challenges coming ahead.

Whenever you perceive an image, this image is distorted to some degree. This starts with the illumination the image is being acquired with and ends with imperfections in your eye. The illumination is also called probing beam or just *probe* in this thesis. Consider a generalized imaging system of a source, optical elements and some detection device.

Ideally the probe is emitted by a point source, but this is never the case in the real world. The consequence is that not a pure spherical wave is emitted and effects of partial coherence arise. For imaging applications the probe is modified by optical elements. The uncertainties in the fabrication process of these element lead to deviations from the ideal profile. These give rise to phase distortions in the probe, which evolve to measurable intensity variations.

The interaction of probe and object is subjected to simplifying assumptions. In the context of this thesis object-probe-interaction is treated as a linear operation. This means any multiple scattering interactions are neglected. After passing through the specimen the probe carries information thereof. This wave field is then also called the *exit wave*.

The final stage in the imaging process is the detection of the exit wave. The process can be non-linear and of statistical nature.

Mathematically the imaging system can be described by

$$I = A(x) + \varepsilon, \quad (1.1)$$

where I is the measured intensity image, x the true complex valued object and ε some statistical distortion: noise. The distortion operator A can be seen as a function modeling the distortions in an effective way e.g. by blurring with a Gaussian filter. In a different way, A can be used to model the propagation through the optical system in a step-by-step approach. In this way it is possible to incorporate the (measured) properties of the optical elements in the image formation process. Section 1.3 illustrates the effects of A and ε on I . In order to reach best resolution, the effects of A and ε have to be considered.

The aim of this thesis is to develop strategies to take the effects of a distorted (Chapter 2), partially coherent probe (Chapter 4) into account. This is achieved by characterization of the probe. Characterization means, in particular for this thesis, carrying out the phase reconstruction for the probe, which yields access to the complete complex valued wave field. The influence of ε is further surveyed in Chapter 3.

The imaging scheme considered in this thesis is *propagation-based near-field phase-contrast imaging using nano-focused hard x-rays*.

Propagation-based imaging eliminates the need for additional optics between the specimen and the object. The wave field propagates according to free space propagation. The intensities of the propagated wave field, are measured by a detector. In order to enable this kind of image formation, the probe has to satisfy requirements on monochromaticity and coherence.

Two important cases, i.e. optical regimes have to be distinguished here:

- (i) Far-field coherent diffractive imaging (CDI) [17] which records the Fraunhofer diffraction pattern, i.e. the Fourier transformation.
- (ii) Near-field imaging or near-field inline holography (NFH) records the diffraction pattern in an intermediate optical regime [5, 18–20], the aforementioned hologram. The spatial frequencies in the wave field mix, but are not fully decoupled as in the far-field case.

In both cases, phase contrast, i.e. the contrast generated by the phase shift, not by the absorption of matter, can be exploited. This is of great advantage when hard x-rays are used. The nanometer resolution obtained with hard x-rays is based on the dualism of high penetration power paired with the large phase shift on nanometer length scales, see section 1.2. Still, it is only a weak interaction with matter. This

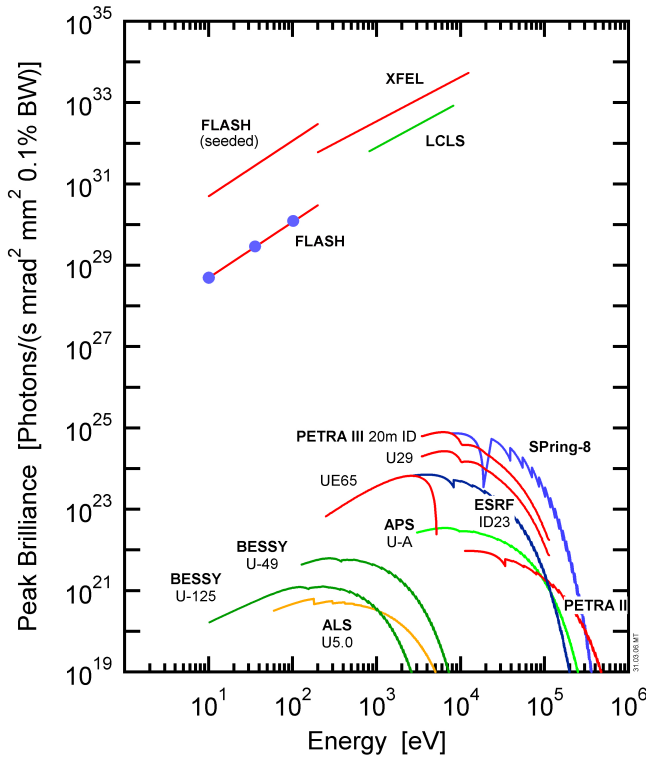


Figure 1.1: Peak brilliance as function of the photon energy for current synchrotrons and XFELs sources [25] (© DESY).

makes it more challenging to produce aberration free optics. The image formation process does not need optics, but in order to generate a magnification in NFH a diverging probe is necessary. The diverging probe is achieved by focusing the x-rays using for example Kirkpatrick-Baez (KB) mirrors [21] or compound refractive lenses (CRL) [22].

The need to reconstruct the probe gains more importance with the advent of the 4th generation x-ray sources. Focusing will not be limited by the available coherent flux [23], but rather by the optics in use. Understanding the optics by characterizing their effect on the beam is necessary both for providing hardware [24] or software solutions to improve imaging quality.

These new sources are x-ray free electron lasers (XFEL) [25–28] and the future upgraded 3rd generation synchrotron sources (PETRA IV at DESY, APS-U at Argonne National laboratory, EBS at ESRF,...). The first 4th generation synchrotron facility MAX IV (Lund, Sweden) has begun operation [29]. The 4th generation sources operate at the diffraction limit, thus their brilliance is extremely increased. The brilliance is a measure of quality for x-ray sources. Figure 1.1 shows the peak

brilliance (photons emitted in a given solid angle per beam area per second per 0.1% bandwidth) of different sources.

Since the capacity at the large scale facilities is limited, there have been efforts to transfer some of their capabilities back to the lab. The compact light source (CLS) [30] is a miniature version of a synchrotron. It is commercially available and the first research group operates this new kind of source [31]. In the same manner compact XFEL (CXFEL) are under development [32].

The increased brilliance enables the experimental access to even shorter length and time scales. This fosters the development of new experimental strategies as *diffract before destroy* [33]. Accordingly, the need for adapted beam characterization schemes grows, cf. Chapter 5.

1.2. Imaging modalities

X-ray microscopy can be realized in two ways with or without lenses. Before the lensless implementation for NFH is discussed we briefly review a lens-based x-ray microscope. Figure 1.2 shows the sketch for a transmission x-ray microscope (TXM) (a) and a lensless propagation-based x-ray microscopy setup with synchrotron radiation (b).

For the TXM, an objective lens is placed after the specimen S which forms the image I on the detector. The image formation follows ray optical principles. The objective lens is often implemented as a Fresnel zone plate (FZP) [34]. The resolution of FZPs is limited by the width of the outermost and smallest fabricated zone. FZPs are fabricated with lithographic methods, this limits the maximal achievable optical depths, due to limitations in the manufacturable aspect ratios. This gives in turn an upper bound for the energy range in which FZPs can be used. In order to accumulate a certain phase shift some optical thickness of the FZP is necessary. The optical thickness necessary for hard x-rays can thus hardly be achieved. A way to fabricate optical thick lenses is the use of layer deposition methods. The lenses produced this way are called multi layer Laue lenses (MLL) [35, 36]. Another drawback is, that FZPs/MLLs are partly absorbing, this means the signal at the detector gets attenuated.

Thus by removing the objective lenses from the beam's path one removes all artifacts and limitations introduced by these. NFH provides an implementation of this idea. In order to reach highest resolution with this technique, a diverging illumination has to be generated. For that a small as possible secondary source has to be

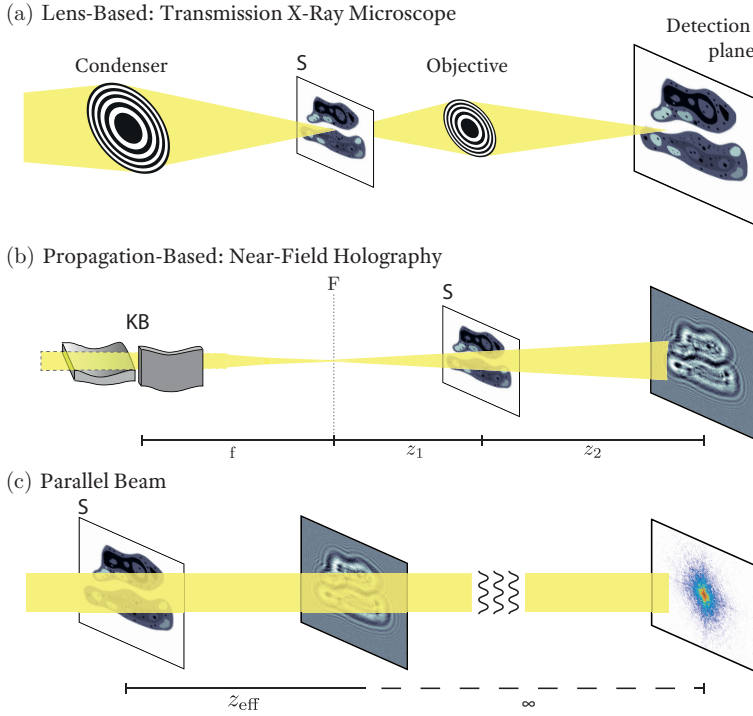


Figure 1.2.: Setup sketch for different microscope types. Lens-based x-ray transmission microscope (a) employing Fresnel zone plates as condenser and objective lenses. Near field holography setup (b) with highly focused x-rays by a Kirkpatrick-Baez (KB) mirror system. The parallel beam geometry (c) illustrates the near and far-field regime. The Fresnel scaling theorem indicates the equivalence between (b) and (g).

created for optimal approximation of a point source. This can be implemented by different focusing techniques as mirrors, notably in KB geometry [21, 37], or compound refractive lenses (CRL) [38]. Using these focusing devices introduces again distortions in the probe. CRLs yield a good beam in terms of distortions, but the intensity in the focused beam is currently not sufficient for high throughput imaging. On the other hand the gain in focusing with KBs is high, but the probe itself shows a contrast rich, structured background cf. Fig. 2.1 and Fig. 5.2. Another way to create an even smaller secondary source is the use of a waveguide (WG) [39], which acts as spatial and coherence filter. The probe's distortions are smaller than for CRLs, but this holds for the flux as well.

In the propagation-based near-field holography setup (b) **S** is placed in a distance z_1 behind the location of the secondary source, denoted as **F**. The detector is

placed in a distance z_2 behind S. The signal evolves now by free space propagation from S to the detection plane.

The propagation to the detection plane is treated within scalar wave theory. It is described by the Fresnel free space propagator

$$\mathcal{D}_{\text{Fr}}(\bullet) = \mathcal{F}^{-1}[\mathcal{F}[\bullet] \cdot H]. \quad (1.2)$$

H is the propagation filter

$$H = \exp\left((-i\pi)/(2\text{Fr})(k_x^2 + k_y^2)\right), \quad (1.3)$$

where $k_x = 2 n_x/N_x$ and $k_y = 2 n_y/N_y$ are spatial frequencies in Fourier space with $n_{x,y} \in [-N_{x,y}/2 \dots N_{x,y}/2]$, $N_{x,y}$ are the dimensions of the discretized image, \mathcal{F} the Fourier transformation and

$$\text{Fr} = \Delta x^2/(\lambda z) \quad (1.4)$$

is the Fresnel number with respect to one pixel of size Δx in the sample plane, wave length λ and the propagation distance z . The measurement at the detector is the hologram of S. The complete analysis is presented in standard texts [40–43] and especially for x-rays [44]. \mathcal{D}_{Fr} can be efficiently computed by a multiplication in Fourier space of the wave field in the starting plane of propagation with H , cf. (1.2).

The propagation filter H can be written in different forms e.g. implicitly or explicitly as a function of z . Also the definition of $k_{x,y}$ depends on the definition of the Fourier transformation in use – in the context of computer science the factor π is omitted. In this work H is written as function of Fr. This allows to consider the propagation in terms of optical regimes, independent from the actual parameter values of an experiment.

The (de-)magnification in (b) is controlled by z_1 and the object to detector distance z_2 in terms of the geometric magnification $M = (z_2 + z_1)/z_1$. This allows to control the field of view. Ideally, the resolution is limited by the size of the secondary source. But other influences, in particular vibrations in the setup, degrade the resolution.

While the TXM can work with incoherent x-rays, NFH needs at least partially coherent x-rays, so that the hologram can be formed. This is a stronger requirement on the illumination, but it also comes with the advantage that phase-contrast imaging is enabled by NFH in a natural way. Looking at the complex valued index

of refraction $n = 1 - \delta + i\beta$, the real part δ can be identified as the cause for the phase shift when a wave passes through a medium and the imaginary part β is responsible for the attenuation of the wave's amplitude. At typical energies for hard x-ray considered here, δ is multiple times (up to magnitudes) larger than β . For example at an energy of 8 keV ($\lambda = 0.015$ nm) carbon has $\delta = 7.15 \cdot 10^{-6}$ and $\beta = 1.19 \cdot 10^{-8}$ [45]. In classical absorption imaging, the attenuation caused by β is the contrast giving mechanism. For a thin specimen, likewise when the resolution element gets small, the attenuation is negligibly small. The phase shift is due to the larger δ not negligibly, but it is not directly accessible by the measurement, due to the high oscillation frequency of the x-rays. By propagation the phase shift gets encoded in measurable intensities. This effect is realized by the self interference of the wave field. For that to happen, a deterministic phase relation in the probe is necessary, which is guaranteed by a certain degree of coherence.

TXM can be extended to phase-contrast by inserting phase shifting plates in the back focal plane of the objective [46, 47] (Zernike phase-contrast). For this contrast mode TXM also requires a certain degree of coherence. A more detailed study of the coherence requirements for NFH can be found in Appendix A.

1.3. Propagation and imaging artifacts

The image formation process in NFH is described by the free space Fresnel propagator \mathcal{D}_{Fr} as given in Eq. (1.2). The numerical implementation of \mathcal{D}_{Fr} bears some pitfalls. For example the discrete Fourier transformation (DFT) is periodic. Wave fields subjected to propagation should thus be padded and windowed [48, Chapter 4.6] to reduce DFT artifacts. Another important aspect is the sampling of the exponential filter function Eq. (1.3). An overview of different propagation techniques and associated sampling is given in [49]. The sampling of Eq. (1.3) must be chosen such that the phase jump between two adjacent sampling points, i.e. two adjacent pixels, does not exceed π . Thus the sampling of H should be chosen as

$$\Delta x \geq \frac{\lambda z}{L}, \quad (1.5)$$

where L is the physical side length of the wave field in its starting plane of propagation. Writing $L = N\Delta x$ and using the definition of Fr yields

$$N \geq \frac{1}{\text{Fr}}. \quad (1.6)$$

Thus smaller Fr need more pixels N to properly propagate. If N gets prohibitively large for computation ($N \geq 20000$) one can make use of the properties of the convolution. Equation (1.2) can be equivalently written as a convolution \otimes in real space

$$\begin{aligned} \mathcal{D}_{\text{Fr}}(\bullet) &= \bullet \otimes h \\ &= \mathcal{F}^{-1} [\mathcal{F}[\bullet] \mathcal{F}[h]]. \end{aligned} \quad (1.7)$$

$\mathcal{F}[h]$ can be analytically computed and yields H . H is sampled in Fourier-space, on the other hand h is sampled in real space, Fourier transformed and then used for multiplication in Eq. (1.7). As a consequence, the sampling criterion changes to

$$\Delta x \leq \frac{\lambda z}{L} \quad \Rightarrow \quad N \leq \frac{1}{\text{Fr}}. \quad (1.8)$$

The large geometric magnifications occurring in NFH are not simply treated in the numerical implementation of the propagation. Some propagators can handle magnifications of $M \leq 2$ [50]. Thus in general the *Fresnel scaling theorem* [44, App. B] is applied which carries out the propagation with effective values for the propagation distance z_{eff} and pixel size Δx_{eff} , i.e. demagnified detector pixels Δx_{det} ,

$$z_{\text{eff}} = \frac{z_1 z_2}{z_1 + z_2} \quad \text{and} \quad \Delta x_{\text{eff}} = \frac{\Delta x_{\text{det}}}{M}. \quad (1.9)$$

This rescaling amounts to a transformation from diverging beam to parallel beam geometry as depicted in Fig. 1.2(c). In parallel beam geometry all divergence effects are lacking, since the rescaling removes the spherical wave component. Important wave field properties as the focus size can not be retrieved in the parallel beam geometry.

The sampling of the propagated wave field is important, as well. The data analysis in Chapter 2 is carried out in a non-standard way since the propagation is done in the lab frame. In this particular case the diverging probe of a nano focusing setup, i.e. the propagating wave field, has been reconstructed. The requirements on the sampling of H could be easily satisfied for the given Fr. The strong phase change makes it necessary to sample with a smaller pixel size. Implementing the propagation via the convolution, either using h or H , has the advantage of a numerically fast implementation. This is of great advantage for example in an iterative phase-retrieval process. On the other hand sufficient sampling must be ensured. The wave equation can be solved by other means as well, for example by finite differences [51] or advanced discretization of the transfer matrix [52].

These schemes can handle different samplings in source and target plane, but are numerically more costly.

Being sure, that the propagation is appropriately handled, we can turn to the different effects which degrade image quality. The image formation process is subjected to several sources of distortion. The following illustrates the effects of a distorted, polychromatic and partially coherent illumination and noise on a hologram.

Figure 1.3 shows the influence of noise for given fluence μ (the mean number of photons per pixel in the sample plane), finite coherence length ξ , finite spectral bandwidth λ and distortions in the illumination, modeled by Zernike polynomials Z [40] on the measured hologram $M_{\mathcal{X}}$, where \mathcal{X} denotes one or a combination of distortions. The parameter values have been chosen for illustration purposes. A detailed study for the influence of μ has been carried out in Chapter 3 and for ξ in Appendix A. Details on the simulation are given within the respective chapters. We start with a phantom (a) of a pure phase object from which we calculate the ideal hologram M_{id} (b) for $\text{Fr} = 10^{-3}$. The hologram M_{μ} spoiled by Poissonian noise for $\mu = 100$ ph/px is shown in (c). Close inspection shows the grainy structure introduced by the noise. The partly covered image illustrates the deviation of M_{μ} to M_{id} by division of both. The deviations exhibit the grainy structure as well. These are basically uncorrelated, pixel wise distortions. The finite coherence length $\xi=100$ px (d) has a blurring effect on M_{ξ} . We note that substructure in the fringes is missing and the finer, further out lying fringes lose their visibility, cf. Fig A.3. The deviations manifest themselves as a structured speckle like pattern. The influence of non monochromatic illumination is shown in (e) for $\Delta\lambda/\lambda = 10^{-2}$. Using the propagation of errors σ_{Fr} has been calculated, i.e. $\text{Fr} = 10^{-3} \pm 10^{-5}$. The interval $[\text{Fr} - 2\sigma_{\text{Fr}}, \text{Fr} + 2\sigma_{\text{Fr}}]$ has been equidistantly sampled in 41 steps. For each of these Fr a hologram has been calculated and weighted according to a normalized Gaussian distribution with $\sigma = \sigma_{\text{Fr}}$ before summing up. The distortions look similar as in (d) but less intense. A phase-distorted beam using the Zernike polynomials Z_J with $J = \{1, 4, 7, 8, 9\}$ modeling respectively piston, defocus, vertical coma, horizontal coma, and spherical aberration has been used to simulate M_Z (f). Each of these distortions has been treated as an incoherent contribution to the hologram, cf. Chapter 4. The deviations show more structure of deviating fringes than in (d) or (e). In panel (g) all distortions are applied to M_{id} to yield $M_{\lambda,\mu,\xi,Z}$. The Δ values next to the deviation plot denote the ℓ^2 -norm of the difference of $M_{\mathcal{X}}$ to the ideal hologram

$$\Delta = \sum_{\forall \text{ pixels}} \|M_{\mathcal{X}} - M_{id}\|^2. \quad (1.10)$$

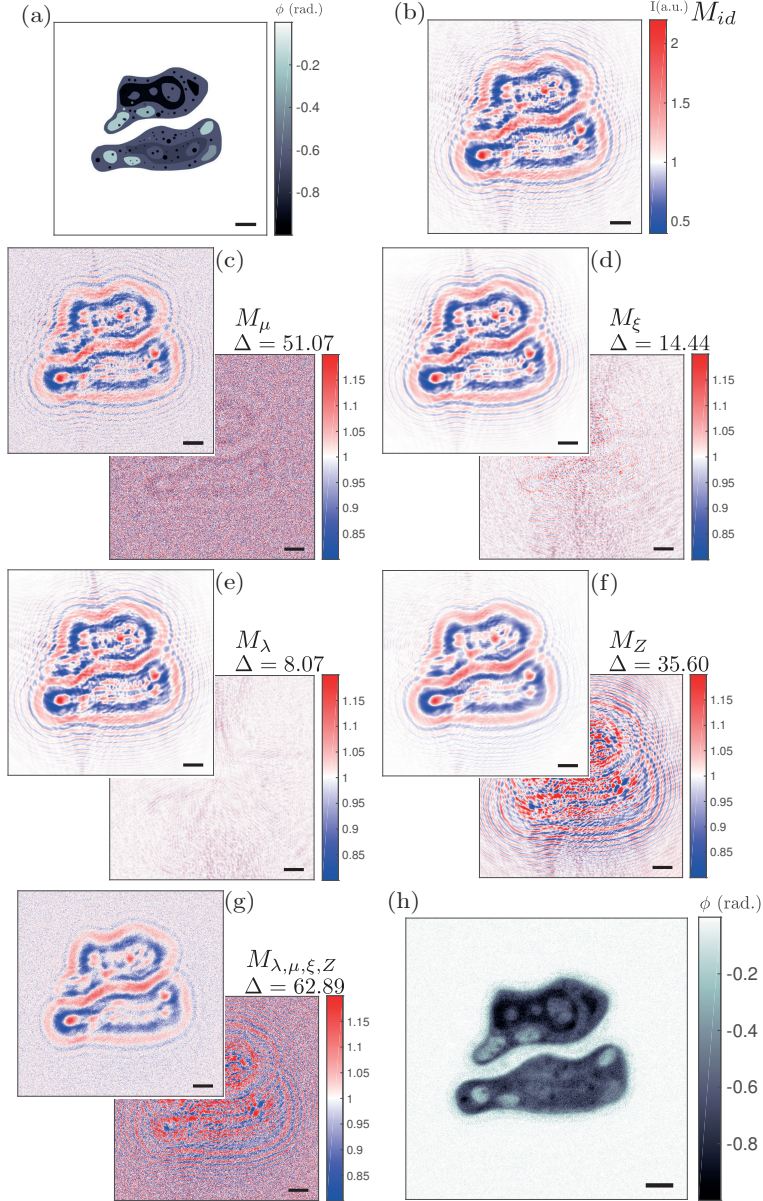


Figure 1.3.: Examples for imperfect holographic measurements. The phantom (a) is propagated with the Fresnel propagator \mathcal{D}_{Fr} to yield the ideal measurement of the hologram M_{id} (b). The deviation to M_{id} is illustrated by division of the corresponding $M_{\mathcal{X}}$ in the partly covered image shown in panels (c)–(g). Δ denotes the ℓ^2 -error to M_{id} . The following panels depict the influence of noise M_{μ} (c) for $\mu = 100$ ph/px, partial coherence M_{ξ} (d) with $\xi = 100$ px, non-monochromatic radiation M_{λ} (e) with $\Delta\lambda/\lambda = 10^{-2}$ and beam distortions M_Z (f) modeled with Zernike polynomials with $J = \{1, 4, 7, 8, 9\}$. The superposition of all distortions $M_{\lambda,\mu,\xi,Z}$ is shown in (g). The phase reconstruction of (g) is shown in (h) using an iterative phase-retrieval algorithm. The measurements are all shown on the same color bar corresponding to M_{id} (b). The scale bar indicates 50 px.

We note here a rather mild influence of ξ and λ . The beam distortions Z show a stronger impact. The largest source of image degradation stems in this setting from the noise induced by the small fluence μ . Increasing μ leads to a reduction of the error, cf. Chapter 3.

Finally, the effect on the phase reconstruction can be visualized. The phase reconstruction obtained by an iterative method calculated from $M_{\lambda,\mu,\xi,Z}$ is shown in (h). Note, the reconstruction has assumed ideal conditions, the non ideal state of the input has not been taken into account. Surprisingly, NFH still shows a recognizable reconstruction of the phantom (a). The reconstruction clearly suffers from the noise and missing contrast in the fringes, visible by the loss in resolution. This exemplifies already some of the results being presented later.

The Zernike polynomials, here used for beam distortions, are well suited to describe the overall properties of the illumination but not the fine scaled distortions encountered in NFH, see for example Fig. 2.1 and Fig. 5.2. These distortions stem from imperfections – height deviations of the ideal shape in the order of 1 nm and less – of the mirrors used for focusing. The height deviations act as pure phase objects. The phase shift develops in some measurable intensity by the same phase-contrast mechanism as before but now as an artifact. The actual measurement of the object’s hologram is spoiled by these artifacts. The standard approach to remove these artifacts is to divide the measurement of the object by the measurement of the illumination, i.e. the standard flat-field or empty-beam correction. The division is carried out in intensities, which obviously can not be correct, since it neglects the complex-valued nature of the wave field. The error of this division has been previously illustrated [53] and mathematically analyzed [54]. In the case of a point source the division is correct, but not for extended sources. The error gets larger for extended sources, where higher spatial frequencies can be present in the illumination. The result of the division is worst if large frequencies (fine details) are present in object and illumination.

2. Probe Reconstruction for Holographic X-ray Imaging

Johannes Hagemann, Anna-Lena Robisch, Markus Osterhoff and Tim Salditt
Reproduced from *Journal of Synchrotron Radiation* (2017), **24**, 498 – 505.

In x-ray holographic near-field imaging the resolution and image quality depends sensitively on the beam. Artifacts are often encountered due to the strong focusing required to reach high resolution. Here we present and compare two schemes for reconstructing the complex-valued and extended wavefront of x-ray nano-probes, primarily in the planes relevant for imaging (i.e. focus-, sample- and detection plane). Firstly, we use near-field ptychography based on scanning a test pattern laterally as well as longitudinally along the optical axis. Secondly, we dispense of any test pattern and reconstruct the wavefront only from data recorded for different longitudinal translations of the detector. For this purpose, we present an optimized multi-plane projection algorithm, which can cope with the numerically very challenging setting of a divergent wavefront emanating from a hard x-ray nanoprobe. The results of both schemes are in very good agreement. The probe retrieval can be used as a tool for optics alignment, in particular at x-ray nanoprobe beamlines. Combining probe retrieval and object reconstruction is also shown to improve the image quality of holographic near-field imaging.

2.1. Introduction

Preparation of the x-ray probe for coherent imaging applications is indispensable in order to reach high resolution and quantitative contrast. This includes control of focusing, coherence and wavefront. A particular case in point are the quasi-spherical wavefronts required for holographic full-field tomography [55–57]. In these high resolution experiments, propagation images are recorded in a divergent beam to achieve the required magnification. Hence nano-focusing [58] is required, even though the sample is placed in the defocus plane located several

milli- to centimeters behind the focal plane. In order to process the raw images in propagation imaging, before phase retrieval is applied, idealizing assumptions are made on the beam, such as point-source emission or distortion-free wavefront. The validity of such assumptions has recently been investigated, showing that they lead to reduced resolution and image quality [53, 54]. Aiming at more appropriate schemes to treat the data, recent work has introduced the concept of simultaneous reconstruction of probe and object to near-field (propagation) imaging [13, 14]. This was achieved by a suitable generalization and extension of the ptychographic algorithms initially developed for confined beams (typical for far-field diffractive imaging) [59–64]. In [13, 65], the object was scanned transversally in the extended wave field behind a wavefront diffuser, in order to increase the diversity of the probe. Thus, the wavefront modified and not the 'natural' probe of the setup is recovered. Contrarily, [14] used the diversity generated by lateral and longitudinal shifts of the object in the beam to recover the natural probe of the setup along with the object. Since beam reconstruction in one plane gives access to the wavefront in all other planes, based on numerical propagation, one may wonder why a near-field reconstruction is needed at all. Since a few years already, x-ray nano-focus optics have been characterized by far-field ptychographic means, scanning an object in or near the focal plane, see for example [61, 62]. While this is correct in principle, we show in this study that the small distortions in the probe which significantly hamper the image quality of full-field imaging can only be properly 'probed' in the defocus plane. Since the mirror height deviations are almost atomically flat, the focal field distribution differs only in the extreme tails up to 10 μm in the focal plane of the probe from the ideal intensity distribution. Therefore, probe reconstruction from far-field data measured with a detector with large pixel size e.g. 172 μm for a Pilatus (DECTRIS) detector, does not cover the field of view (FOV) in the focal plane to include the tails. Thus the propagation of such a reconstructed probe in the near-field does not accurately account for the characteristic fringes of the KB pattern, as measured with a high resolution detector in the near-field. Contrarily, near-field probe retrieval is perfectly able to accomplish this. To this end, we propose: If you measure in the defocal plane, reconstruct in the defocal plane. At the same time, we are interested in a complete characterization which also includes the field in the focal plane. This was previously not accessible, since in the data of [13, 14] the FOV is cut out from the central part of the probe. This is not sufficient to obtain the complete information on the probe, i.e. it is for example not possible to reconstruct the size of the focal spot, which is obviously an essential information for the maximum achievable resolution. In this work we record the complete

decay of the probe at the holography end station **GINIX** (Göttingen Instrument for Nano-Imaging with X-rays)[2, 66] at the P10 beamline of Petra III (DESY, Hamburg), and use it for reconstruction based on an improved multiple magnitude projections (MMP)-scheme [53, 67, 68] as well as the near-field ptychography (NFP)-scheme [14]. We recorded two independent data sets: One for NFP with the afore-mentioned lateral and longitudinal shifts of an object with a fixed focus to detector distance. The other set for MMP consists of a detector scan along the longitudinal direction, i.e. the focus to detector distance is varied. The fundamental difference in these data sets (in view of probe reconstruction) is the way the data diversity is introduced. In NFP a mixing operation is performed of probe P and object O , while for MMP the changes in the distance of the detection plane introduce diversity. MMP can not only be exploited for probe reconstruction but also for object reconstruction, as demonstrated before in other wavelength regimes [67, 68].

The two independent approaches yield probe reconstructions which are in very good agreement. Beyond reconstruction of the probe, the presented scheme bears significant advantages also for imaging, i.e. reconstruction of objects. Note that most alternative phase retrieval algorithms in the near-field setting, which also exploit longitudinal scanning (diversity) such as the contrast transfer function (CTF) reconstruction [20] or the transport of intensity equation (TIE) [69, 70], rely in on assumptions (pure phase object, slowly varying phase, linearity of the propagation) of the wave field under reconstruction, which limit the range of their applicability. None of these restrictions apply to the MMP or NFP scheme.

Section 2.2 introduces the experimental setup and the measurement schemes. In Sec.2.3 an optimized version of the MMP-algorithm is introduced, suitable for diverging beams and noisy data. Section 2.4 compares the wave field reconstructions of NFP and MMP, both in and around the focal plane and the far-field. We close the paper in Sec. 2.5 with some practical considerations, how the presented methods can be used for nano-focus optimization and alignment.

2.2. Experimental setup

The experiment was carried out at the nano-focus end station (**GINIX**) of the P10 undulator beamline [2] with photon energy set to 8 keV by a Si(111) channel-cut monochromator. Figure 2.1 (a) shows a sketch of the setup. A set of slits allowed to control the illuminated area of the Kirkpatrick-Baez (KB)-mirrors, and hence also the divergence of the focused beam. The different measurement

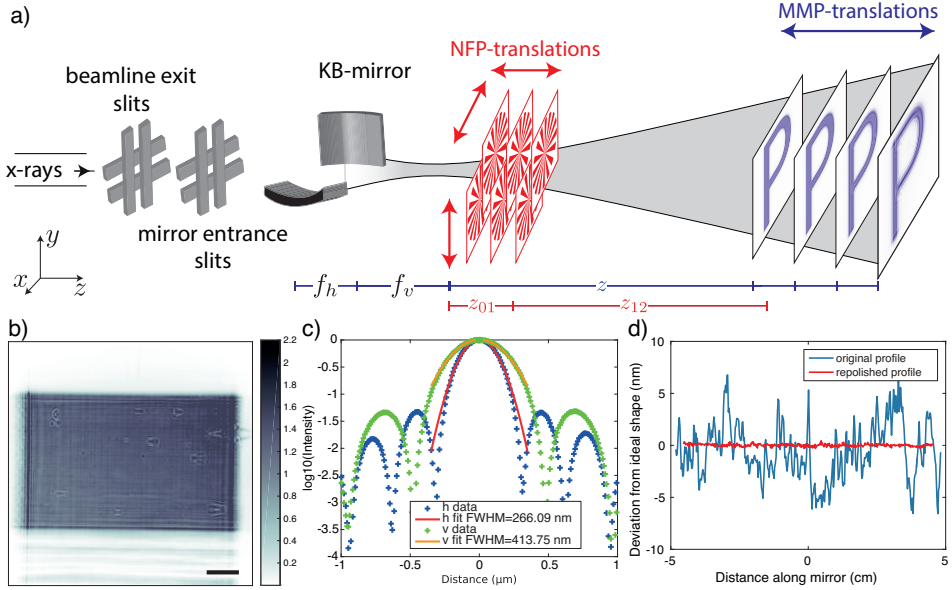


Figure 2.1.: Experimental setup. (a) Basic sketch of the nano-focus instrument (GINIX setup at P10 beamline PETRAIII) and data acquisition scheme. The monochromatic beam is focused by a KB-mirror system, placed 88 m upstream from the undulator source. The beam size in front of the KB is controlled by two pairs of slits. For the MMP scheme, the empty beam intensity distribution, represented by a P, is recorded at different defocus positions z (blue translations) along the optical axis with no additional object in the beam path. Contrarily, the NFP scheme (red translations) requires an additional test object placed (Siemen star) at varied defocus positions z_{01} and an overlapping scan in transversal direction, while the detector distance is fixed. (b) Example of the beam intensity distribution recorded for $z = 0.3346$ m for $400 \times 400 \mu\text{m}^2$ slit opening. Scale bar indicates 100 μm . (c) Intensity distribution along the principle axis (horizontal, vertical) in the focal plane, as simulated numerically by a Huygens principle approach [71] for a $100 \times 100 \mu\text{m}^2$ slit settings, and the measured height profile of the mirrors. (d) Deviations from ideal height profile for the vertical focusing mirror, shown for original and upgraded mirror.

schemes are color coded in red (NFP) and blue (MMP). The intensity patterns were recorded by a scintillator(LUAG) coupled CCD (PCO pco.2000) with $20\times$ magnification microscope lens, resulting in an effective pixel size of 370 nm. The detector was placed on a motorized stage following the beam's optical axis. For MMP, empty beam recordings were acquired at 4 detector defocus distances of $z = \{0.3643, 0.3542, 0.3443, 0.3346\}$ m with an exposure time of 0.1 s. This series of measurements was obtained for the following settings of the beamline slits: $50 \times 50, 100 \times 100, 250 \times 250, 250 \times 400, 400 \times 400$ (horizontal(μm) \times vertical(μm)).

Parameter	MMP	NFP	Unit
Beamline exit slits (h×v)	100×100	100×100	μm ²
Mirror slits (h×v)	400×500	220×270	μm ²
z_{01}	–	{80, 85, 90, 94}	mm
z	{33.5, 34.4, 35.4, 36.4}	37.2	cm
Pixel size	37	{80, 85, 90, 93}	nm

Table 2.1.: *Experimental parameters for the MMP and NFP recordings.*

A typical measurement is shown in (b). For NFP, an additional object is required. Here we used a Siemens star test pattern with 100 nm thickness of Tantalum (NTT-AT). The object was placed at different defocus distances z_{01} , see Tab. 2.1. At each distance, a lateral scan with step size of 5 μm of 4×4 points was performed with 40 ms exposure time. The detector was kept at a fixed position at $z = 0.3723$ m. The KB-mirrors have been recently upgraded by state of the art elastic emission machining (EEM) polishing [72], resulting in a height deviation (from the ideal ellipse, peak to valley) of $\sigma_{\text{figure}} = 0.89$ nm, 0.88 nm and a root-mean-square-roughness $\sigma_{\text{rough.}} = 0.09$ nm, 0.1 nm, for the horizontal(h) and the vertical(v) mirror, respectively, see height profile function in (d). This corresponds to a 5.4(h), 15.8(v) fold improvement for the figure errors and a 4.4(h), 1.5(v) fold improvement for the roughness over the initial values [2, 66]. Note that for these near atomically flat reflecting surfaces, the focal intensity distribution becomes almost identical to the ideal case, over four orders of magnitude in the intensity, as shown in Fig. 2.1 (c). Contrarily, the flat-field pattern still shows the characteristic stripes originating from the height deviations.

2.3. MMP - algorithm

Reconstruction of a nano-focus probe P amounts to the reconstruction of a complex valued wave field Ψ from intensity measurements, i.e. it is a perfect example of solving the phase problem. In comparison to [53], we use here an optimized algorithmic approach for MMP based on [73], which we will call sequential relaxed averaged alternating reflections (sRAAR), since the projection on the measurements is carried out in a sequential manner. An iteration of sRAAR is given by

$$\Psi_{n+1} = \prod_{i=1}^J \frac{\beta_n}{2} (R_S(R_{M_i}(\Psi_n)) + \Psi_n) + (1 - \beta_n)P_{M_i}(\Psi_n), \quad (2.1)$$

where $R_{S/M_i}(\Psi) = 2P_{S/M_i}(\Psi) - \Psi$ denotes a (mirror) reflection by a given constraint set, and $i \in \{1 \dots J\}$ enumerates the intensity measurements M_i . J influences the accuracy of the reconstruction, already for $J = 2$, given that the change in Fr is sufficient, we can obtain reconstructions for Ψ . Increasing J further increases accuracy, but for the expense of more costly numerical operations. The parameter β_n controls the relaxation, and is varied as a function of the iteration number n according to

$$\beta_n = \exp\left(- (n/\beta_s)^3\right) \beta_0 + \left[1 - \exp\left(- (n/\beta_s)^3\right)\right] \beta_{\max}, \quad (2.2)$$

where β_0 denotes the starting value, β_{\max} the final value of β_n and β_s the iteration number when the relaxation is switched. This relaxation strategy follows [73] (Eq. 37). A value of β_0 close to 1 helps in the beginning to efficiently sample the possible solutions, during the later iterations the smaller β_n helps to draw the weight on the measurements. The projection on the measurements P_{M_i} is given by

$$P_{M_i}(\Psi) \equiv \mathcal{D}_{-\text{Fr}_i} (A_{M_i} [\mathcal{D}_{\text{Fr}_i} (\Psi)]) , \quad (2.3)$$

where A_{M_i} is the actual adaptation of amplitudes, given by

$$A_{M_i}(\Psi) = \left(1 - \left[\frac{|\Psi|^2}{(|\Psi|^2 + \epsilon)^{1/2}} - \sqrt{M_i} \right] \frac{|\Psi|^2 + 2\epsilon}{(|\Psi|^2 + \epsilon)^{3/2}} \right) \Psi, \quad (2.4)$$

which follows [74], ϵ is a constant to prevent a division by 0 in the order of magnitude of machine precision. Note that this implementation of the projection on the measurement constraint introduces a smooth perturbation, which improves numerical stability [73]. The propagation to the individual measurement planes is performed by the Fresnel propagator \mathcal{D}_{Fr} , for a given Fresnel number $\text{Fr} = \Delta x^2/(\lambda z)$ with respect to the pixel size Δx ,

$$\mathcal{D}_{\text{Fr}}(\Psi) = \mathcal{F}^{-1} [\mathcal{F} [\Psi] \exp((-i\pi)/(2\text{Fr})(k_x^2 + k_y^2))], \quad (2.5)$$

where k_x and k_y are frequencies in Fourier space. The operator P_S applies a support constraint in the focal plane, it is given by

$$P_S(\Psi_n) = |\Psi'_n| \cdot \exp [i(\arg(\Psi'_n) + \arg(\Psi_n))] , \quad (2.6)$$

where Ψ'_n is given by

$$\Psi'_n = \mathcal{F}^{-1} (S \cdot \mathcal{F} (|\Psi_n|)) . \quad (2.7)$$

This is basically a back propagation to the focal plane neglecting the curvature followed by application of a support constraint.

The support constraint S is defined as

$$S = \begin{cases} 1 & \text{for } \sqrt{q_x^2 + q_y^2} < q_c \\ 0 & \text{else} \end{cases} \quad (2.8)$$

where q_x and q_y denote coordinates in the focal plane and q_c the cut off value. The hard cut-off can be relaxed by using a Gaussian window. Applying S directly on $\mathcal{F}(\Psi_n)$ leads to a propagation by a unknown distance, since the curvature is not exactly known in the beginning of the reconstruction process. This problem is circumvented by taking the modulus. The algorithm and the projectors in use have been tested in a numerical experiment, for details confer to the supplement material.

2.4. Results

The MMP algorithm described in Sec. 2.3 was applied to the data, after performing the following raw data processing steps: After subtraction of a dark image the intensities were scaled to mean amplitude 1 and then aligned to the center of mass of the contour of the beam. Other alignment schemes like Fourier space registration [75] do not work for this kind of data, due to the divergence.

The pixel size of all distances has been reduced by interpolation to 37 nm. This high sampling is necessary for artifact free Fresnel propagation, in particular to account for the rapidly varying chirp functions of the spherical contribution of the phase, otherwise the propagation in between the measurement planes is inconsistent. Note that in contrast to many previous treatments and the NFP implementation below, the MMP data is not transformed to an equivalent parallel beam geometry

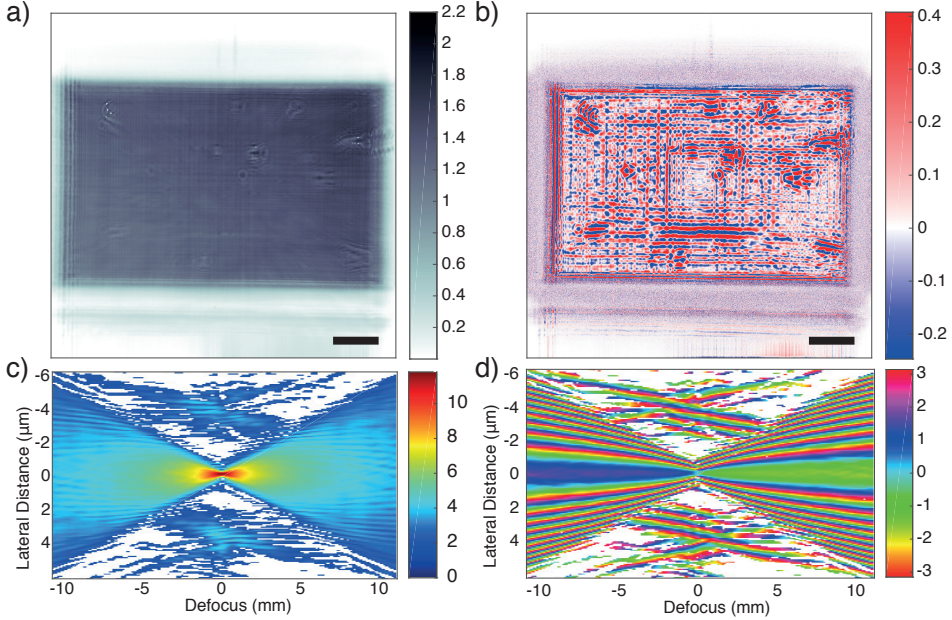


Figure 2.2.: Probe reconstructed from MMP for the $400 \times 400 \mu\text{m}$ slit setting, showing (a) amplitude and (b) phase, in the detection plane at 0.3643 m . Scale bar indicates $100 \mu\text{m}$. The corresponding propagation profile is also shown in (c) intensity (logarithmic) and (d) phase along the optical axis $\pm 10 \text{ mm}$ around the focal plane in the vertical direction. Pixels with intensity values smaller than 10^{-5} of the maximum value were masked out with white.

(by Fresnel scaling theorem), but treated in the direct coordinate system. After preprocessing the data were used as input for sRAAR presented in Sec. 2.3. The parameters for sRAAR were $\beta_0 = 0.99$, $\beta_{\text{max}} = 0.75$, $\beta_s = 150$. sRAAR was iterated 2000 times starting from the measured amplitudes in the plane at $z = 0.3643 \text{ m}$ multiplied with the phases of a Gaussian beam, giving a first guess for the curved wavefront. For the reconstructions we assumed $w_0 = 250 \text{ nm}$, where w_0 is the waist of a Gaussian beam. We chose for the support constraint $q_c = 200 w_0$. Figure 2.2 shows the result for the typical imaging configuration of the exit slits with $400 \times 400 \mu\text{m}^2$. In this configuration, the mirrors are fully illuminated, i.e. the maximal length of the mirrors is illuminated. This correspondingly highest numerical aperture results in the smallest focal width of $192(2) \times 170(1) \text{ nm}^2 (\text{h} \times \text{v})$, as determined from the reconstructed focus via fitting a Gaussian function with linear background. The reconstructed probe wave field is shown in Fig. 2.2 (a) amplitude and (b) phase at the detection plane at $z = 0.3643 \text{ m}$. Assuming that the

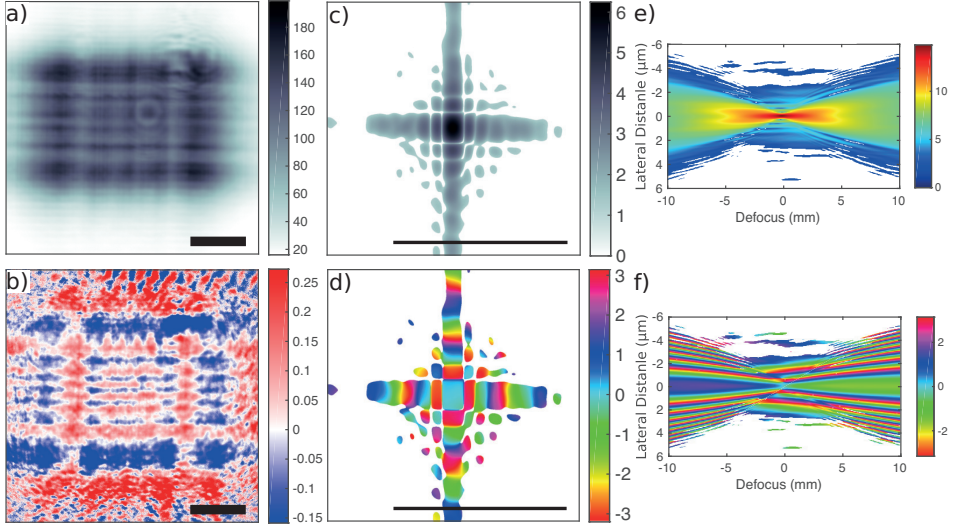


Figure 2.3.: Probe reconstructed from NFP for the $100 \times 100 \mu\text{m}^2$ slit setting, showing (a) amplitude and (b) phase in the detection plane at 0.3732 m . Scale bar is $50 \mu\text{m}$. The focus intensity (c) and phase (d) are obtained by Fourier transformation. Scale bar is $5 \mu\text{m}$. The corresponding propagation profile is also shown in (e) intensity (logarithmic) and (f) phase along the optical axis $\pm 10 \text{ mm}$ around the focal plane in the vertical direction. Pixels with intensity values smaller than 10^{-5} of the maximum value were masked out with white.

far field approximation holds, which is well justified in view of the small Fresnel number ($\text{Fr} = 2.5 \cdot 10^{-5}$), we apply the Fourier transform to recover the probe in the focal plane. By application of the Fresnel propagator, we can then simulate the propagation around the focus, see (c) and (d).

Next we present the NFP results and a corresponding comparison. A detailed description of NFP can be found in earlier publications [14, 76]. The preprocessing steps for the NFP are as follows: The holograms were dark field corrected. In a next step the holograms have been aligned in transversal direction via a Fourier space registration [75] using the encoder positions of the scanning motors as starting guess. For the longitudinal alignment i.e. the correction of propagation distances, an auto-focus algorithm [77] has been used. The reconstructions were obtained after 25 NFP iterations. The object O was initialized with uniform amplitude 1 and phase shift of -0.2 rad . In the first 10 iterations the constraint for negative phases has been applied to the object's guess. P was initialized by a back-propagated flat field. The feedback parameter for P was chosen as $\beta = 0.1$ and $\alpha = 0.2$ for the object. Note that the necessary Fresnel scaling is applied on the current guess of

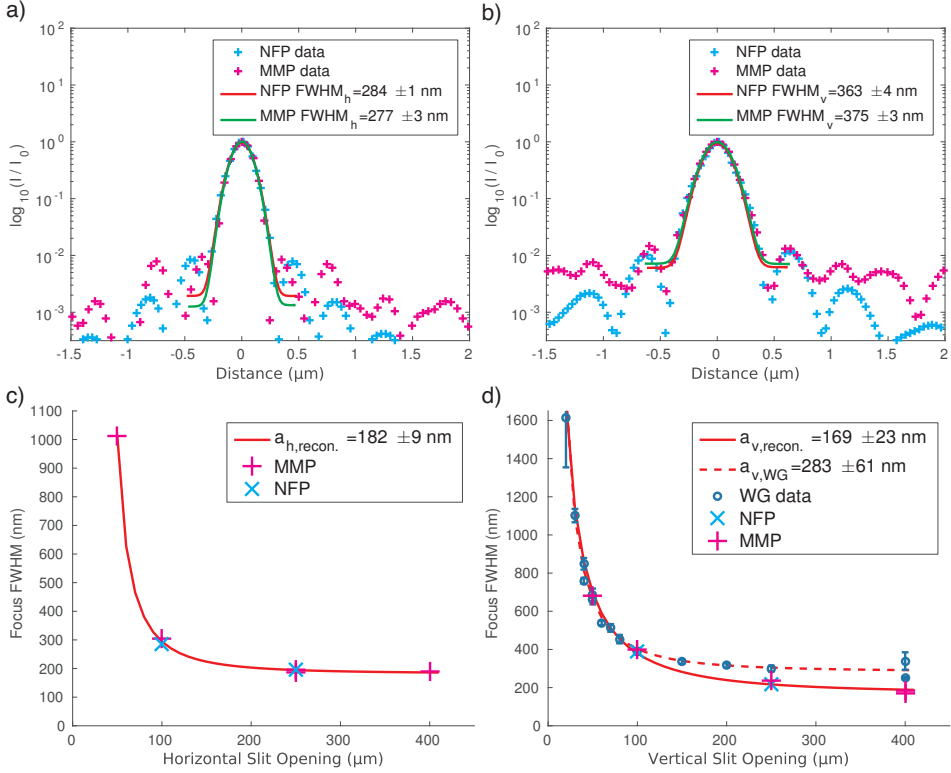


Figure 2.4.: Comparison of reconstructed (normalized) intensity profiles of NFP and MMP in the horizontal (a) and vertical (b) direction of the focal plane, for the $100 \times 100 \mu\text{m}^2$ slit setting. Using the series of slit settings we illustrate the dependence of focus size on slit opening for horizontal (c) and vertical (d) direction. Using the model function Eq. (2.9) for the focus width, the size of the source's image is $a_{\text{recon.}} = 182(9) \times 169(23) \text{ nm}^2$. (d) Same as (c) with additional and completely independent results for the focus size, as determined by scanning a waveguide (with entrance size 50 nm).

O before projecting on the measurements by resizing the reconstruction matrices. Figure 2.3 presents the results of the NFP reconstruction, for a $100 \times 100 \mu\text{m}^2$ slit opening, and Fig. 2.4 the results of NFP and MMP in direct comparison, evaluating the reconstructions along the principal axis and the corresponding focal spot sizes for horizontal (a) and vertical (b) direction. Good agreement between both completely independent methods is observed, concerning in particular the central peak and the first side oscillation. As measure for the focus size we use the full width at half maximum (FWHM) of a Gaussian with linear background fitted to the central peak. Again, we find good agreement between NFP and MMP

with 284(1) nm to 277(3) nm horizontally and 363(4) nm to 375(3) nm vertically, respectively. The data acquired for an entire series of slit settings is shown in graphs (c) and (d), illustrating the dependence of the focus size on the slit opening d (numerical aperture), following the expected behavior. The $\text{FWHM}(d)$ curves are then fitted to [78]

$$\text{FWHM}_{h/v} = \left(\underbrace{a_{h/v}^2}_{\text{image of source}} + \underbrace{\left[\frac{c}{d_{h/v} - \Delta} \right]^2}_{\text{diffraction on slits}} \right)^{\frac{1}{2}}, \quad (2.9)$$

modeling both geometric demagnification of the (incoherent) source size $a_{h/v}$ and diffraction broadening as a function of the slit size $d_{h/v}$ (in front of the KB). Physically, the fitting constant c can be related to focal length and photon energy. Note also that an offset Δ with respect to the nominal slit values was introduced to take into account errors in the calibration of the slit size. Fitting Eq. 2.9 to the reconstructed focus sizes yields $a_{\text{recon.}} = 182(9) \times 169(23) \text{ nm}^2(\text{h} \times \text{v})$. The values for the vertical direction (d) are further confirmed by scanning the focal intensity with a waveguide (WG) [79, 80]. From these data we obtain $a_{v, \text{WG}} = 283(61) \text{ nm}$, this value is larger due to vibrations of the WG during the scan, also the finite channel width of the WG broadens the intensity distribution.

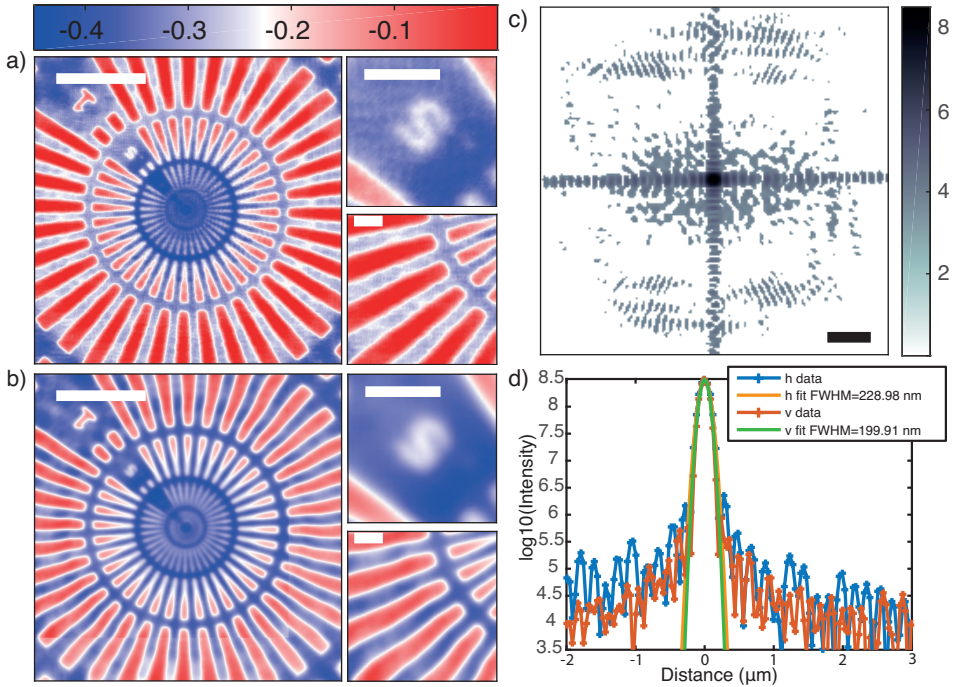


Figure 2.5.: NFP reconstruction of the object, recorded at slit settings of $400 \times 400 \mu\text{m}^2$ ($h \times v$) (beamline exit) and $220 \times 270 \mu\text{m}^2$ (mirror). (a) Phases of the NFP reconstruction for the Siemens star pattern. Scale bar is $10 \mu\text{m}$. The insets show a detail of the $0.5 \mu\text{m}$ marker (top) and a region of the rays (bottom). Scale bar is $2 \mu\text{m}$. (b) Reconstruction using the contrast transfer function algorithm [20] with the same input as (a). Same scale and color bars as in (a). The probe reconstructions corresponding to (a) is shown in (c), along with (d) the corresponding line profiles through focus. The scale bar for (c) indicates $1 \mu\text{m}$. Note that the focal width is smaller than in Fig. 2.4, owing to the larger slit opening.

Figure 2.5 presents the results for object reconstruction under optimized illumination (a), and also illustrates the benefit in image quality, when compared to a standard object reconstruction (b) (without simultaneous probe reconstruction). For this comparison, the contrast transfer function (CTF) algorithm [20] was used, and applied in such a way, that the same amount of datasets were used. Both schemes hence have the same set of measurements as input. We clearly observe the benefit of using an iterative algorithm with probe retrieval. Notably, the insets show an improvement in resolution (detail on .5 marker) and the removal of some low-frequency image distortions (detail on rays). We attribute this improvement to the separation of probe and object.

2.5. Summary and outlook

We have presented a novel approach to reconstruct the extended quasi-spherical wavefront of a hard x-ray nano-probe, in the typical setting of state-of-the-art nanoscale holographic x-ray imaging and tomography using high gain KB focusing. Importantly, the complex-valued illumination wavefront can be retrieved for the unperturbed case of the actual KB beam, without recourse to additional wavefront modification, as in the scheme by [13]. This goal was accomplished by two completely independent approaches, which differ in the data acquisition scheme and the reconstruction algorithm, namely NFP [14] and MMP, which we have further adapted and optimized here, with respect to earlier implementations [53, 67, 81]. Notably, the current implementation can handle the diverging beam in the laboratory coordinate frame without transformation to equivalent geometries, e.g. by application of the Fresnel scaling theorem. While this is clearly more demanding on the computational level, it offers a more direct access to the relevant aspects of focusing and propagation without the assumption of a perfect point beam focus. The resulting reconstructions of the NFP and MMP scheme are in very good agreement, and the benefit of (simultaneous) probe retrieval for actual imaging applications was also demonstrated, comparing the superior object reconstructions of NFP (see Fig. 2.5) with the standard CTF approach.

Finally, we point out that this scheme can be extremely useful for the alignment and improvement of the focusing optics. Near-field reconstructions are less sensitive to partial coherence, and even for large slit sizes can give proper information on the probe. However, since the presented method is numerically involved, one may worry about practical procedures which could give fast and robust feedback, for example during beamline alignment. To this end, we show in the supplemental material that a simple procedure based on the directly computable autocorrelation function, as computed by FFT from the KB far-field, can already help in the optimization of focusing, and when needed can be extended to the full scheme presented here.

Acknowledgments

We thank Michael Sprung for support during the beam time and Aike Ruhlandt for numerous discussions. Funding by SFB 755 *Nanoscale Photonic Imaging* is gratefully acknowledged.

3. The Fluence-Resolution Relationship in Holographic and Coherent Diffractive Imaging

Johannes Hagemann and Tim Salditt

Reproduced from *Journal of Applied Crystallography* (2017), **50**, 531 – 538.

This work presents a numerical study of the fluence-resolution behavior for two coherent lens-less x-ray imaging techniques. To this end we compare in numerical experiments the fluence-resolution relationship of inline near-field holography and far-field coherent diffractive imaging (CDI). To achieve this, we carry out the phase reconstruction using iterative phase retrieval algorithms on simulated noisy data. Using the incident photon fluence on the specimen as control parameter we study the achievable resolution for two exemplary phantoms (cell and bitmap). Our results indicate a superior performance of holography compared to CDI, for the same fluence and phase reconstruction procedure.

3.1. Introduction

The simple question "Which resolution do I get for the invested photon fluence?" is extremely important for x-ray imaging of radiation sensitive specimen, such as biological cells and tissues. Structure analysis by diffraction is in general based on elastic scattering of photons and hence the Thompson scattering cross section, which is much smaller than the cross section for photo absorption, which results in significant energy uptake within the sample and hence causes radiation damage. However, for coherent imaging the dose issue is accentuated, since the information is collected from a single copy of the structure imaged, rather than from a large ensemble of identical constituents, over which the dose is distributed. Pioneering studies have addressed this topic in the framework of kinematic scattering theory for far-field coherent diffractive imaging (CDI) [82, 83], and have found a steep

power-law $D \propto d^{-4}$ relating dose D and resolution d , for the case of imaging three-dimensional (3d) structures at isotropic resolution. Note that this corresponds to equivalent imaging of 2d slices of a width which is scaled down with d , and hence loses contrast. Contrarily, for constant width, increasing only the 2d resolution yields $D \propto d^{-2}$, for diffraction as in absorption, see for example [84]. Further work has studied the effects of having a certain feature of interest embedded in other structures (matrix) [85], showing that the reconstruction quality in CDI is nearly independent of the surrounding (for given dose). Before addressing the case of (coherent) diffraction, which became important after the advent of CDI [17], earlier work had already compared x-rays, neutron, and electrons as microscopy probes, but had exclusively considered image formation by absorption [86]. This is understandable for the simple reason that x-ray microscopy started in absorption contrast, and was only later extended to (phase contrast) diffractive imaging. A comparison between x-ray microscopy in absorption contrast (water window spectral range) and by numerical simulation was provided in [87], showing that isolated low-Z materials such as biological cells can be imaged with fewer photons by CDI. The literature cited above already illustrates the large range of perspectives which one can take to address the dose and resolution issues, at least in a broad sense. One can compare different probes (x-rays versus other probes), different types of contrast (absorption versus phase contrast), different experimental parameters (notably wavelength) or different types of imaging (e.g. lens based x-ray microscopy versus lens-less diffractive imaging). To this list, we here add the optical regime of a coherent diffractive imaging experiment.

Notably, we want to compare direct reconstruction of lens-less coherent imaging data in the near-field and far-field regime. While the previous studies addressing CDI mentioned above were concerned with far field diffraction, the numerical simulations used in this work are carried out in the optical near-field regime. Figure 3.1 shows a principal sketch for a NFH (a) and CDI (b) experiment. (c) shows both cases transferred to parallel beam setting, as it used in the numerical experiments of this study. Our goal is to provide a quantitative comparison between near-field inline holographic imaging (NFH) [5, 18, 88, 89] and CDI [17, 90]. The main difference between this work and the previous mentioned studies is thus the imaging regime in use.

Further, a recent numerical study [91] also assessed NFH and CDI and have formulated a signal-to-noise criterion. Rather than resolution as in the present study, VILLANUEVA-PEREZ ET AL. focused on the sensitivity w.r.t. to the phase shift of a given feature and its size at a constant fluence.

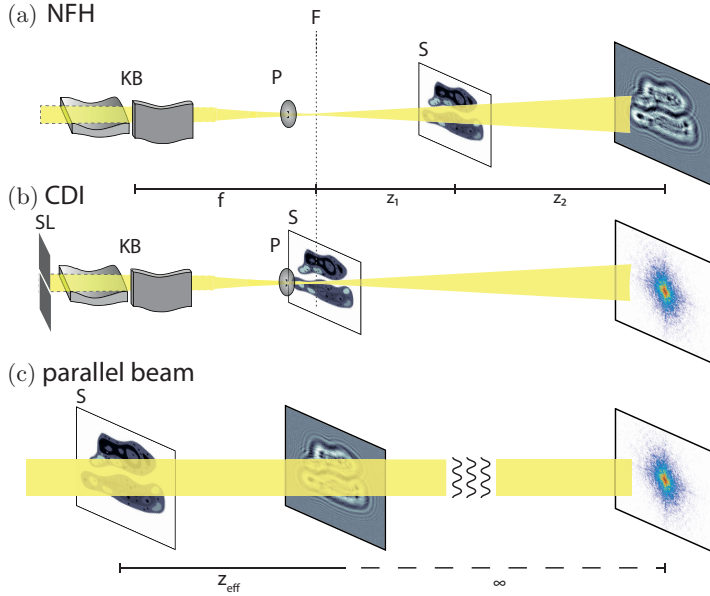


Figure 3.1.: Experimental implementation for NFH (a) and CDI (b) shown in a diverging beam geometry (in particular for a synchrotron setup cf. [2]). The beam is focused by Kirkpatrick-Baez mirrors (KB), then a pinhole (P) is commonly used as a low-pass filter for removing high spatial frequencies in the probing beam. For CDI the specimen (S) is placed in the focal plane (F), while for NFH it is placed at a defocus position z_1 . The detector is then placed in a distance z_2 behind S. This yields for NFH a (de-)magnification of $M = (z_1 + z_2)/z_1$. Note that in order to satisfy the coherence requirements for CDI the effective source size has to be reduced by slits (SL). (c) shows the imaging configurations transferred to the setting of a collimated (parallel) beam. This is achieved via a simple coordinate transform (i.e. Fresnel scaling [44]), where the effective propagation distance is given by $z_{\text{eff}} = z_2/M$.

The motivation of this study are the experimental indications for the high dose effectiveness of near-field holographic (NFH) imaging [79, 92, 93]. In [79] for example, NFH of bacteria were recorded in the multi-keV regime, where a single bacteria is essentially a pure phase contrast object. Reconstructions were obtained at a dose which was orders of magnitude smaller than reconstructions of similar resolution obtained for the same bacteria by (far-field) ptychography before [15]. Since experimental work can always be influenced by a number of additional parameters which can for example easily render the data inconsistent, a higher or lower dose required for a particular experiment is not conclusive *per se*. In the light of the limited evidence, we therefore turn to numerical analysis, comparing the CDI to NFH for simulated noisy data on the same phantoms. To this end, we

have first used the Maximum-Likelihood (ML) approach introduced by ELSER and EISEBITT [94]. Accordingly, a critical fluence μ_c can be defined above which the correct phantom (random bitmap) out of a selection of random bitmaps could be identified with a chosen tolerance (error) level ϵ and for given photon shot noise [95]. In this way, one can test the information content in the noisy 2d diffraction patterns and investigate the dependence of μ_c on object contrast levels, the accepted error level, and the bitmap size. For the experimentally relevant case of weak phase contrast, applicable to most biological samples, NFH required lower dose than CDI for the optimum propagation distance (Fresnel number) [95]. However, apart from small oscillations of μ_c as function of the distance, as expected based on the contrast transfer function (CTF), the results in the near field were almost identical to the far-field results [95]. Hence, as far as the encoding of information is concerned, which can be tested by the ML approach, far-field CDI and near-field NFH seem, in principle to be roughly equal in dose efficiency. What the ML approach cannot address, however, is whether an unknown object can actually be reconstructed from the noisy data, rather than just comparing likelihoods between the true object and some alternatives (bitmaps with randomly switched bits).

In this work, we fill this gap and actually test the actual process of reconstruction from noisy diffraction patterns and not just a ML reconstructability criterion. The main control parameter in this numerical work is again the fluence μ , i.e. the average number of photons per pixel in the plane of the object. Using μ we are able to tune our numerical experiment from the case "barely reconstructing" to "best object reconstruction". According to this parameter we generate test data of two phantoms (i) a cell, and (ii) a bitmap object (as in [95]), see Fig. 3.2. Following the generation of the noisy diffraction patterns, we run phase retrieval algorithms on the data and determine the resolution by Fourier ring correlation (FRC) [96, 97]. Section 2 details on the data generation and reconstruction scheme. Section 3 presents the results for the NFH to CDI comparison. The paper closes in Sec. 4 with summary and conclusion. Of course, implementing both NFH and CDI on the same sample can be experimentally challenging due to limitations of the setup (coherence, beam size, sampling constraints). These considerations are beyond the scope of this work. Further, we consider only coherent scattering (elastic Thomson scattering) and no further interactions of the radiation with matter. Our main focus is the optical regime and the decoding of (phase-)information. Thus all simulations are carried out in a *dimensionless setting* (pixel units and Fresnel number), as detailed below.

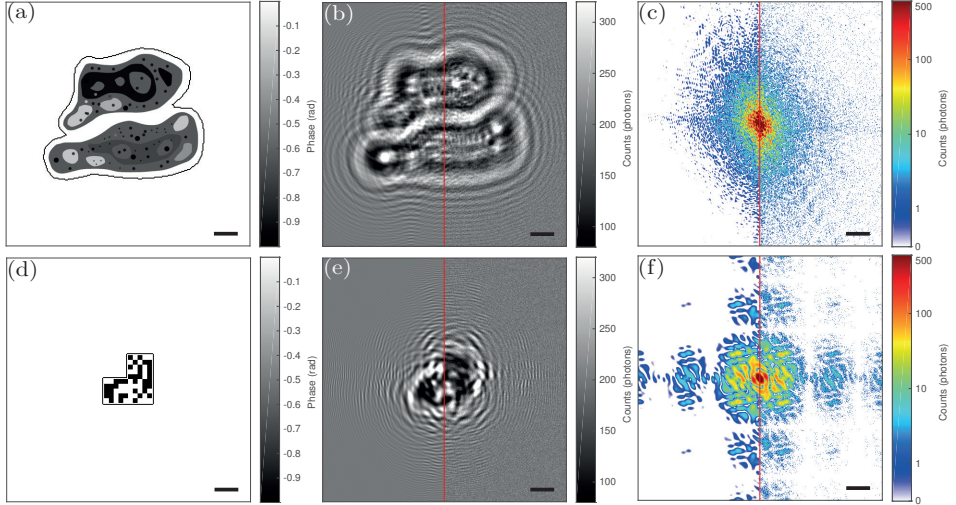


Figure 3.2.: Setup of the numerical experiment. (a) Shows the phase-only phantom of two cells with individual compartments and maximum (exaggerated) phase shift of -1 rad. The size of the phantom is 512×512 pixel² embedded in 1024×1024 pixel². (b) Simulated near-field intensity measurement at Fresnel number of 10^{-3} (linear scaling). The left half shows the noiseless measurement, while the right side shows the measurement with noise for 200 photons per pixel in the detection plane. (c) Simulated far field intensity measurement, analog to (b), a count of 0 photons corresponds to white (logarithmic scale). (d) Bitmap pattern analog to [95]. The maximum phase shift is -1 rad and the size of one bitmap pixel is represented by 10×10 pixels in the sample plane. (e) and (f) analog to (b) and (c), respectively. The solid line surrounding the objects in (a) and (d) marks the border of the support used in the reconstruction. Scalebar indicates 50 px.

3.2. Numerical setup

Figure 3.2 introduces the concept of the numerical study. In essence the two optical setups – far-field CDI and near-field holography (NFH) – are simulated for two different phantoms, namely a phantom of two adhering biological cells (as used in [98]), and a random binary bitmap, see (a) and (d), respectively. Both phantoms are pure phase contrast objects, with phases $\phi_{x,y}$ in the range $[-1, 0]$ rad (cell), and $\phi_{x,y} \in \{0, -1\}$ rad (bitmap). Note, that binary bitmaps with no correlations between pixels are to some extent amenable to analytical treatments and have been used before for in [94] (1d bitmap) and [95] (2d bitmap). Both images have the size of 512×512 pixel² embedded in $1024 \times 1024 (N_x \times N_y)$ pixel². This embedding ensures that the simulated numerical aperture (NA) is sufficiently large to recover

details down to the pixel level. The NA in vacuum is given by

$$NA = \sin \alpha \approx \tan \alpha \approx N_x \Delta x / (2 z_{\text{eff}}), \quad (3.1)$$

where paraxiality is assumed and Δx is the pixel size. The resolution limit d_{min} due to the NA is

$$d_{\text{min}} = \lambda / (2 \sin \alpha), \quad (3.2)$$

with wavelength λ . Inserting Eq. (3.1) and using the definition of the Fresnel number $\text{Fr} = (\Delta x)^2 / (\lambda z_{\text{eff}})$ yields

$$d_{\text{min}} = \frac{\lambda z_{\text{eff}}}{N_x \Delta x} = \frac{1}{\text{Fr}(N_x / \Delta x)}. \quad (3.3)$$

Setting $d_{\text{min}} = \Delta x$ yields then $F \geq 1/N$ as a requirement for the NA.

In both cases, CDI and NFH we assume perfect illumination as by point source or in equivalent geometry by a plane wave (cf. Fig. 3.1(c)) such that the exit wave Ψ is given by the phantom $\Psi = \exp(i\phi_{x,y})$. The measurements for NFH have been generated by applying the Fresnel propagator \mathcal{D}_{Fr} given by

$$\mathcal{D}_{\text{Fr}}(\Psi) = \mathcal{F}^{-1} [\mathcal{F} [\Psi] \exp((-i\pi)/(2 \text{Fr})(k_x^2 + k_y^2))], \quad (3.4)$$

where $k_x = 2 n_x / N_x$ and $k_y = 2 n_y / N_y$ are spatial frequencies in Fourier space with $n_{x,y} \in [-N_{x,y}/2 \dots N_{x,y}/2]$ and a Fresnel number of $\text{Fr} = 10^{-3}$. The measurements for CDI have been generated by discrete Fourier transformation \mathcal{F} of the corresponding exit wave. Next, the generated intensity patterns (far-field and near-field, respectively) in the detection plane are subjected to Poissonian noise using the routine `imnoise` (Matlab. Inc.), with the average photon fluence μ (in photons per pixel) in the object plane as only parameter. Fig. 3.2 (b,c) and (e,f) show in each case the ideal noiseless simulated data or ‘measurements’ (left side), as well as a random realization of the noisy measurement for a fluence of 200 photons per pixel (in the exit plane). The exemplary NFH and CDI measurements simulated for the phantom nicely illustrate the completely different nature of the signal: In the case of NFH the signal varies around one (normalized primary beam) by self-interference of primary beam with the diffracted beam behind the object, and is best represented in linear scale with a narrow range of intensities. Contrarily, the CDI data covers many orders of magnitude from the central pixel to the edge of the detector, where most pixels have zero photon counts. Note that in this idealized simulation, we take the full diffraction pattern into account i.e.

the numerical aperture is sufficiently large and assume that the detector does not need any kind of beamstop, which would result in a loss of information.

Thus, in summary, the noisy measurements have been generated using the following recipe:

1. Propagate the field Ψ from the sample plane to the measurement plane (detection plane) using the respective propagator \mathcal{X} (\mathcal{F} or \mathcal{D}_{Fr}).
2. Calculate the intensities of the field, yielding the measurement $M = \|\mathcal{X}(\Psi)\|_2$; normalize M so that $M' = \sum_{\text{pixels} \in M} M(x, y) \equiv 1$.
3. Multiply M' with $\mu \cdot N_x \cdot N_y$, use the result as input for a Poisson random number generator. This yields the noisy measurement used in for the phase reconstruction.

The reconstructions from the noisy data have been obtained by using the Relaxed Averaged Alternating Reflections(RAAR)-algorithm [73]. The iterates are given by

$$\Psi_{n+1} = \frac{\beta_n}{2} (R_S(R_M(\Psi_n)) + \Psi_n) + (1 - \beta_n)P_M(\Psi_n), \quad (3.5)$$

where $R_{S/M}(\Psi) = 2P_{S/M}(\Psi) - \Psi$ denotes a (mirror) reflection by a given constraint set and n the iteration index. The parameter β_n controls the relaxation. It follows the function

$$\beta_n = \exp\left(- (n/\beta_s)^3\right) \beta_0 + \left[1 - \exp\left(- (n/\beta_s)^3\right)\right] \beta_{\text{max}}, \quad (3.6)$$

where β_0 denotes the starting value, β_{max} the final value of β_n and β_s the iteration number when the relaxation is switched. This relaxation strategy follows [73] (Eq. 37). The parameters have been set for to $\beta_0 = 0.99, \beta_m = 0.75, \beta_s = 150$ iterations all reconstructions. The projection on the measurements P_M is the standard magnitude projector

$$P_M(\Psi) \equiv \mathcal{X}^{-1} \left\{ M^{1/2} \cdot \exp(i \cdot \arg[\mathcal{X}(\Psi_m)]) \right\}, \quad (3.7)$$

where \mathcal{X} is either \mathcal{F} or \mathcal{D}_{Fr} for far-field or near-field propagation, respectively. In Eq. (74) [74] an alternate version for P_M is given which should handle numerical inconsistencies such as noise. In our case, the experiments using this version did not show any improvement for the resolution.

The operator P_S is used to enforce the support S which is assumed to be perfectly

known and the pure phase constraint in the object plane i.e.

$$P_S(\Psi_n) = \begin{cases} \exp(i \cdot \arg(\Psi_n)) & \text{for pixel} \in S \\ \exp(i \cdot 0) & \text{for pixel} \notin S \end{cases} \quad (3.8)$$

The code to reproduce the results can be found on GitHub: <https://github.com/JHoahg/Resolution-and-Fluence> .

3.3. Results

Before addressing the fluence-resolution relationship, we present an exemplary reconstruction to illustrate the steps which are necessary to obtain the reconstruction data, which are then analyzed by massively parallel batch processing. Figure 3.3 shows an exemplary reconstruction for $\mu = 200$ photons per pixel for both phantoms (a) and (c), using the noisy measurements shown in Fig. 3.2 (c,d,e) and (f).

The left and right side of Figure 3.3 (a, c) show the phases of the NFH and CDI reconstruction, respectively, again for both the (a) cell and (c) the bitmap phantom. The reconstructions are based on the same set of parameters and constraints as far as possible. There are two differences: (i) the propagation operator (\mathcal{F} or \mathcal{D}_{FR}) and (ii) the starting guess. For the holographic reconstruction, an array uniformly initialized with amplitude 1 and phase 0 was used, whereas the CDI reconstruction used an initialization consisting of uniform amplitude 1 but randomly chosen phases from the range $[-\pi, \pi]$, both in the object plane. Changing the initial guess typically had only little effect on the results. Inspection of the holographic reconstructions in (a) and (c) shows some high frequency noise in the background of the reconstructions, but still the fine structures of the cells (small black dots) are clearly visible and the edges of the bitmap are sharp. The CDI reconstruction of the cell shows clearly a loss of detail, but the background is less noisy. For the bitmap we see washed out edges and some structured background which matches the length scale of the bits. Note that the reconstruction show the object after the measurement projection (before the support is enforced).

For quantitative comparison of the resolution, we have used FRC. To this end, the phases of the reconstructions are correlated with the corresponding phantom phases (Fig. 3.2), and the decrease of the correlation is plotted as a function of spatial frequency. The resolution is determined by the first intersection, f_r , the resolved spatial frequency, with the so-called 1/2-bit threshold, indicating the

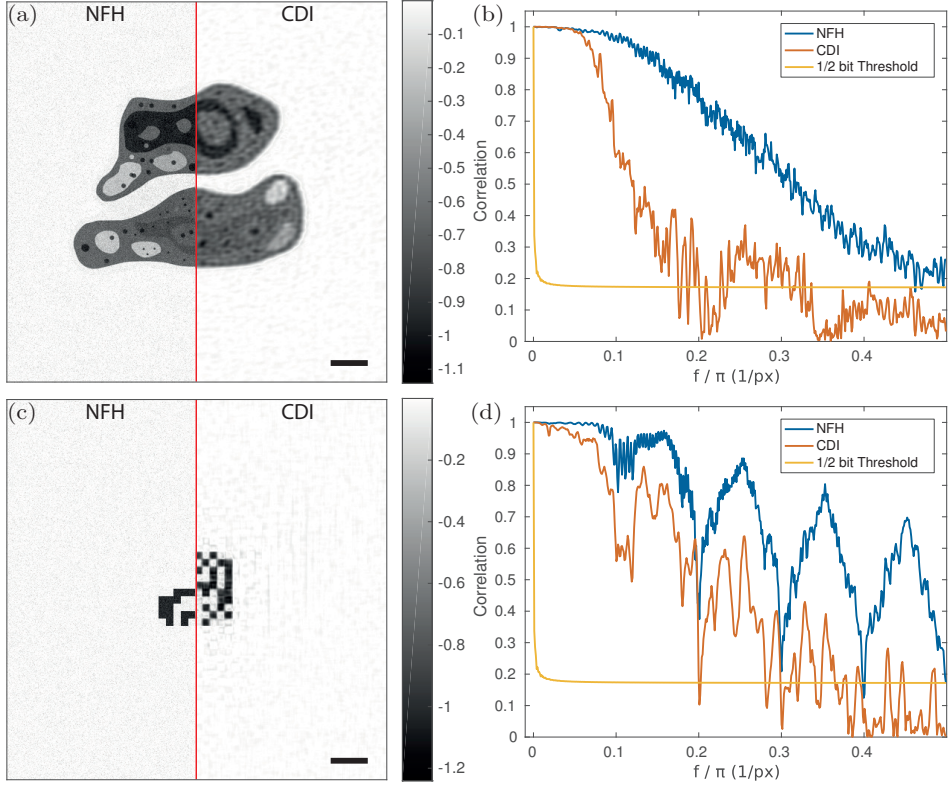


Figure 3.3.: Example reconstructions for 200 photons per pixel. (a) Shows the phases (rad.) of the reconstruction of the cells after 200 iterations of RAAR ($\beta_0 = 0.99$, $\beta_m = 0.75$, $\beta_s = 150$ it.) using a support and pure phase object constraint. The left half shows the reconstruction obtained by the near-field data, the right side the results for the far field data. (b) Fourier ring correlation of the reconstructions with the phantom in Fig. 3.2 (a). (c) and (d) analog to (a) and (b) for the bitmap object shown in Fig. 3.2 (c). Scalebar indicates 50 px.

degree of correlation at which sufficient signal has been acquired [97]. The results are shown in Fig. 3.3 for (b) the cell and (c) the bitmap. The FRC curve in (b) for the CDI reconstruction decays much faster ($f_r = 0.17$) than for the NFH reconstruction ($f_r = 0.48$), in agreement with visual inspection. Interestingly, the FRC curves for the bitmap phantom show an oscillatory behavior, but again the CDI curve decays faster ($f_r = 0.2$) compared to the NFH curve ($f_r = 0.4$), i.e. shows less resolution.

Next, we turn to the fluence-resolution relationships which are computed by performing the automatized reconstruction and FRC analysis for measurements of

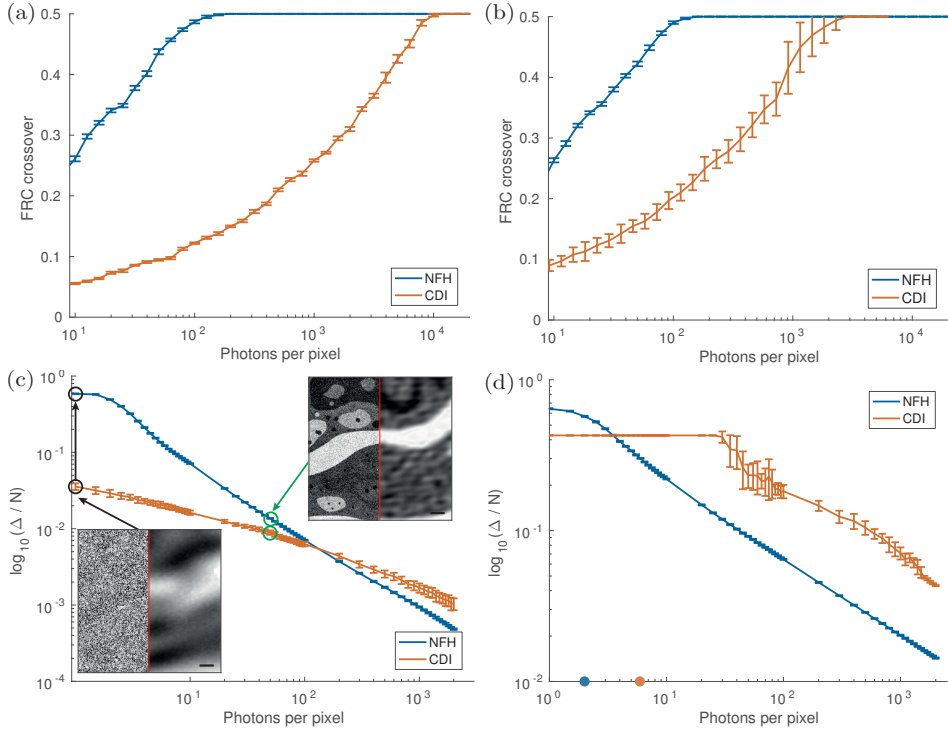


Figure 3.4.: Resolution as function of the dose for holographic and coherent diffractive imaging. (a) Result for the cell phantom. (b) Result for the bitmap phantom. The photon number ranges from 1 to 20000 photons per pixel. Each photon number had 30 realizations for the near and far field measurement. The reconstruction was carried out with RAAR and the same settings as before. (c) Δ (normalized by the number of pixels in the support N) for the cell phantom as function of the fluence. The inserts (200×200 central pixels of the cell phantom) show different phase reconstruction snapshots (NFH left, CDI right) for fluencies of 1 (black) and 50 (green) photons per per pixel, with respectively colored arrows. The insets scalebar is 20 px. (d) Δ/N for the bitmap. The colored dots mark the critical fluence obtained by ML simulations.

systematically varied fluence μ . For each μ covering the range from 1 to 20000 photons per pixel (phantom plane), 30 realizations have been generated and reconstructed, each with the same parameters. Figure 3.4 shows the results. Comparing the results for (a) the cell and (b) the bitmap, we notice that in both cases the NFH reconstruction reaches the maximum achievable resolution at significantly smaller fluence. Note that the spatial frequency of 0.5 periods per pixel corresponds to the maximum (half period) resolution of a pixel. However, reaching the full resolution is not necessarily equal to having a perfect reconstruction. For example, the ℓ^2 -

norm of the difference image (reconstruction-phantom) can be non zero, while the FRC has already saturated. Comparing (a) and (b) we notice that NFH reaches the maximum resolution for both objects at the same fluence of around 300 photons per pixel. At the same time, the error bars of the bitmap results are larger than for the cell. Contrarily, CDI needs 11000 photons to reach full resolution for the cell, and 3000 photons for the bitmap. Furthermore, we have analyzed the error of the reconstruction by the ℓ^2 -norm, see Fig. 3.4 for (c) the cell, and (d) the bitmap. To this end, the ℓ^2 -norm Δ of the phase difference

$$\Delta = \sum_{\forall \text{pixels} \in S} \|\arg(\text{phantom}) - \arg(\text{reconstruction})\|^2, \quad (3.9)$$

has been computed for all pixels within the support. The Δ curves in (c) and (d) are normalized by the number of pixels in S and show an unexpected behavior. At low fluencies the error of CDI is smaller than that of NFH followed by a cross-over at $\mu = 140$ (cell) and $\mu = 4$ (bitmap), where NFH becomes superior in terms of Δ . On closer inspection of the reconstruction result, however, it becomes clear that the smaller Δ at low fluence is misleading. CDI yields an unstructured reconstruction with no representation of structural details, see inserts in (c). The reconstructions are much worse than the NFH results for the same fluence, but exhibit a smaller Δ , by ways of averaging the signal deviations. We must conclude that Δ is not a well suited error metric at low fluence.

Thus, it becomes clear that in all cases tested, NFH yields superior results than CDI. Note that the absolute Δ values also depend on the number of iterations (200 in both cases). Running the algorithm for more iterations, e.g. 800 iterations, led to a further reduction of Δ of about 30% in the case of NFH, and 10% for CDI (cell phantom). Furthermore, the introduction of additional constraints of course can also change the error value. For example, using the prior knowledge that the binary bitmap must have discrete phase values 0, -1, suggest to use a thresholding constraint (binary value projector)

$$P_S(\Psi_n) = \begin{cases} \exp(-i) & \text{if } \phi_{x,y} < 0.5 \\ \exp(0i) & \text{if } \phi_{x,y} \geq 0.5 \end{cases}. \quad (3.10)$$

Figure 3.5 shows the results using this projection in addition to support and pure phase constraint for the bitmap phantom. For these results we have used a bitmap with 1:1 pixel correspondence of bitmap to object plane pixel. Thus the entire object has a size of only 10×10 pixel. Fig. 3.5 (a) shows the Δ/N error (as in

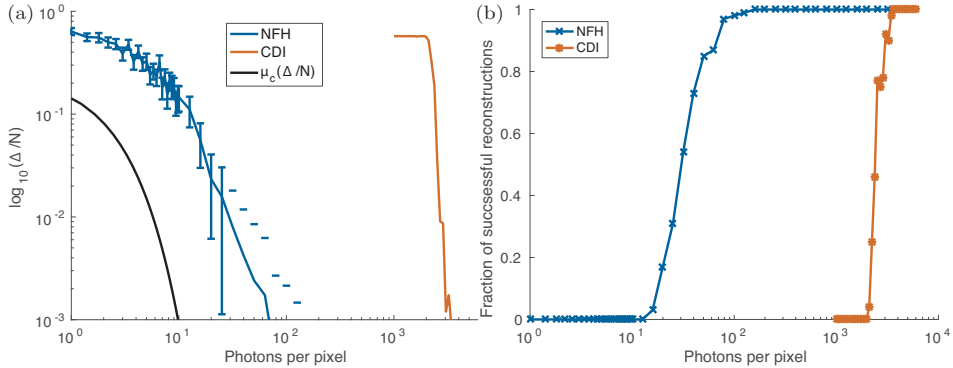


Figure 3.5.: Reconstructability results for the bitmap. (a) Δ/N evolution for the thresholded reconstruction on a bitmap object with 1:1 pixel correspondence of bitmap and object plane pixel. (b) Fraction of successful, i.e. $\Delta = 0$, reconstructions for 100 repetitions of a given fluence, cf. [95].

Fig. 3.4(d), but now after the threshold constraint), corresponding to the fraction of wrong pixels. Here we see the expected behavior, that NFH reconstructs better at low fluence than CDI. For comparison, we also plot the theoretical function $\mu_c(\Delta/N)$ (solid line) based on the ML analysis, describing the critical fluence to identify the correct bitmap from the noisy diffraction pattern (CDI), out of a set of neighboring bitmaps [95]. Figure 3.5 (b) shows the fraction of successful reconstructions, i.e. the fraction of successful reconstructions ($\Delta = 0$) from an ensemble of 100 runs, as a function of fluence. Comparing these results we see that CDI reconstructions require substantially more flux at any error level. Furthermore, the functional form of the curve is smoother for NFH, while the transition from non-reconstructible to reconstructible is extremely sharp for CDI similar to a phase transition.

3.4. Summary and outlook

In this work, we have investigated the fluence efficiency of variants of lens-less x-ray imaging techniques, notably coherent diffractive imaging (CDI) operating in the optical far-field, and inline holography (NFH) operating in the optical near field. Despite the entirely different nature of the signals and the image formation, which can be classified as heterodyne and homodyne, i.e. with and without adding a reference wave, it is commonly assumed that the information content in the diffraction pattern for given photon fluence should be equal. The analytical

work and the simulations of [95] have already pointed out that this can never be exactly true, since the oscillatory nature of the contrast transfer functions in NFH result in a dependence on the Fresnel number. Therefore, absorption and phase contrast has to be distinguished, and furthermore also the regime of weak or strong contrast. However, the Maximum-Likelihood approach of [95] addresses the information content of the noisy pattern and not the reconstruction quality which can actually be obtained by standard methods of iterative algorithms. As we have shown here, the latter case is characterized by substantial differences between NFH and CDI. In other words, while the information content may be similar, the ability of the algorithms to decode the diffraction pattern deviate significantly. These conclusions have been substantiated both by the error metric of the ℓ^2 -norm Δ and Fourier ring correlation. For example, Fig. 3.5 (b) showed that both NFH and CDI reach full reconstructability within one decade of photon fluence, but for CDI fluence curve was shifted up by two decades. Furthermore, both NFH and CDI reconstructions required substantially higher fluence as predicted by the ML approach. In conclusion, our findings point to an important advantage of NFH, in addition to the large tolerance for partial coherence, the compatibility with extended specimen and the flexibility in reconstruction constraints e.g. the pure phase constraint is often sufficient to reconstruct at least a coarse image of the object). Some of these advantages may also apply to ptychography, for example, when mixed states are taken into account [99]. It goes without saying, that these conclusions await further validation by other reconstruction codes as well as by careful experimental test. If the evidence is substantiated, more imaging experiments of radiation sensitive specimen such as biological objects should be carried out in the holographic regime for which dedicated synchrotron beamline are now available.

3.5. Appendix A: Direct back propagation

Following the suggestion of a reviewer, we have investigated to which extent the results obtained in this work depend on the reconstruction (which always requires a specific choice of constraints and reconstruction algorithm), we have also performed simulations in the simplest possible setting, based on direct back propagation. To this end, the exit wave in the sample plane was first propagated to the detector plane to generate diffraction data as before. The, Poisson noise was added to the intensity (amplitude), again as before. Finally, the wave with the noisy amplitude and ideal phase was propagated back to the sample plane. The

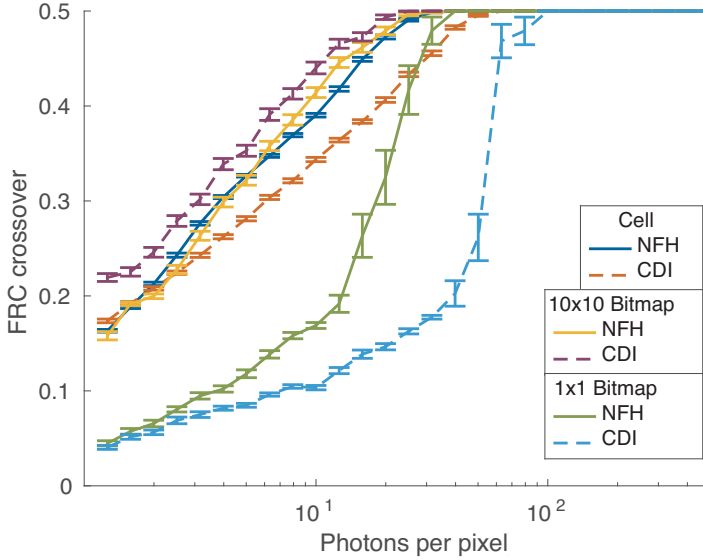


Figure 3.6.: Results for direct back propagation. Three objects are compared: the cell, a bitmap with each bitmap pixel represented by 10×10 image pixels and a bitmap with direct 1:1 pixel correspondence. Solid lines correspond to NFH results for a Fresnel number of 10^{-3} , dashed lines correspond to CDI results. The results for each fluence μ have been averaged over 30 noise realizations.

idea of this procedure was to eliminate the role of the reconstruction algorithm used. The ideal complex valued data M is given as

$$M = \mathcal{X}(\Psi), \quad (3.11)$$

where \mathcal{X} is either \mathcal{D}_{Fr} or \mathcal{F} for NFH or CDI, respectively and Ψ the exit wave in the sample plane. Using the noising procedure from the main text gives the noisy intensities $\|M\|_{\epsilon}$ which are then combined with the phases to yield \hat{M}

$$\hat{M} = \sqrt{\|M\|_{\epsilon}} \cdot \exp(i \cdot \arg(M)), \quad (3.12)$$

i.e. the noisy complex amplitudes. The \hat{M} are generated for different fluences μ ranging from 1 to 1000 photons per pixel and are then used as input for the inverse propagator \mathcal{X}^{-1} for NFH and CDI. Figure 3.6 shows the results of this numerical experiment. We compare three different phantoms: (i) the cell phantom, (ii) the bitmap phantom with one bitmap pixel represented by 10×10 image pixels (oversampled information), and (iii) one bitmap pixel represented by 1 image pixel.

NFH shows again superior performance for the cell phantom and the 1×1 bitmap, but not to the same degree as before. Furthermore, CDI reaches higher resolution at lower dose for the 10×10 bitmap. This can be understood based on the fact that in this numerical experiment the phases are given, and the main advantage of NFH in encoding phase information by interference does not play a role.

In addition, we have varied the contrast of the object. The results illustrate the same trend for both CDI and NFH: As the phase shift of the phantom increases, less photons are needed to reach maximum resolution, as expected. This is in agreement with the findings of [91].

Acknowledgments

We thank Jan-David Nicolas, Malte Vassholz and Simon Maretzke for fruitful discussions and Chris Jacobsen for inspiring comments.

Funding by BMBF project *05K16MGB - WeKokUbS: Wellenfront- und Kohärenzkontrolle an Undulatorbasierten Strahlquellen zur Optimierung bildgebender Verfahren* and CRC 755 Nanoscale Photonic Imaging is gratefully acknowledged.

4. Reconstructing Mode Mixtures in the Optical Near Field

Johannes Hagemann and Tim Salditt

Reproduced from Optics Express (2017) **25**, 13973 – 13969

We propose a reconstruction scheme for hard x-ray inline holography, a variant of propagation imaging, which is compatible with imaging conditions of partial (spatial) coherence. This is a relevant extension of current full-field phase contrast imaging, which requires full coherence. By the ability to reconstruct the coherent modes of the illumination (probe), as demonstrated here, the requirements of coherence filtering could be relaxed in many experimentally relevant settings. The proposed scheme is built on the mixed-state approach introduced in [Nature, **494** (2013)], combined with multi-plane detection of extended wavefields [Opt. Commun., **199** (2011); Opt. Express, **22** (2014)]. Notably, the diversity necessary for the reconstruction is generated by acquiring measurements at different defocus positions of the detector. We show that we can recover the coherent mode structure and occupancy numbers of the partial coherent probe. Practically relevant quantities as the transversal coherence length can be computed from the reconstruction in a straightforward way.

4.1. Introduction

The coherence properties of the illumination (probe) are a fundamental prerequisite for lensless coherent imaging techniques [44, 100], both in the optical near field and far field. When reconstructing from measured data, the assumption in particular of a spatially fully coherent illumination is ubiquitous, even though it is clear that this condition is never (and can never be exactly) fulfilled [101]. The effects of image degradation by partial coherence have been described in many different settings [102, 103]. Measured or estimated spatial [104] or temporal [105] coherence properties have also been incorporated in the phase reconstruction process.

Wavefront sensing and coherence measurements have therefore attracted significant attention in the past, especially in the x-ray regime where coherent imaging has stirred much interest as a way to circumvent the lack of suitable lenses [61, 62, 106–113]. The rationale for measuring coherence properties in these studies is that by experimental control of the probe, spatial coherence can be increased sufficiently high to warrant that the coherence length ξ exceeds the field of view. In this way the requirements of conventional phase retrieval algorithms can be met. Recently, however, the methodology for phase retrieval has been extended by Thibault and Menzel to include the reconstruction of multiple coherent modes in the phase retrieval process [99]. Their approach follows the concept of coherent mode representation [101, 114] which has been widely used in many optical disciplines. The coherent modes are a particular example of the concept of state mixtures. Mixed states can also account for aberrations in the object (vibrations) and detection (point spread function) plane. They have demonstrated, that the inclusion of the mode reconstruction in the phase retrieval process can yield not only an enhanced reconstruction quality for objects under partial coherent imaging conditions but also a description of the partial coherent probe in terms of modes. The additional information required for the reconstruction can be generated from ptychography [12, 59], where diversity in the data is increased by scanning the object through the probe. The state mixture concept was extended and applied to different experimentally relevant configurations, for example for non-monochromatic radiation [115] or a (deliberate) smearing of the probe during on-fly-scans [116]. Further it has been shown, that the reconstruction of states can reveal more information about a specimen [117]. The symmetry of the operations in the ptychographic reconstruction algorithm can also lead to ambiguities in the reconstructed states and additional constraints are required in some cases to break these ambiguities [118].

However, the extension to the coherent imaging in the optical near field has so far been lacking. At the same time, multi-mode reconstructions of extended wavefields are of considerable interest. Firstly, extended multi-mode reconstructions can help to understand on a fundamental level why the near-field imaging is found to be more tolerant to partial coherence than its far-field counterparts. Secondly, full-field x-ray imaging is of tremendous practical importance, in particular for larger specimen and for tomography, where scanning techniques are prohibitive. Importantly, near-field or propagation imaging is almost always known to be implemented in a partial-coherence setting, including robust exploitation of phase contrast at laboratory sources [56, 119–121].

In this work we show by numerical simulations, that the extraction of coherent modes can be also applied to reconstruct the extended probe as it is used in x-ray propagation imaging or inline x-ray holography. To this extent we present an algorithm based on multiple magnitude projections (MMP) [67] generalized to mixed states, i.e. partial coherence. We have previously used MMP for probe characterization [53, 122] under the assumption of full coherence. We denote its multi-modal generalisation by mmMMP. In both the MMP and mmMMP schemes, the detector is moved to different longitudinal distances (propagation distances). This movement changes the Fresnel number of the probe with respect to some reference plane (e.g. the first measurement or the focal plane) and introduces diversity in the measurements, which is required for a reliable reconstruction. Note that in general, mmMMP will require more detection planes than MMP to compensate for the information loss inflicted by partial coherence. We show that mmMMP algorithm is capable of recovering the coherent modes with their accompanying occupation and the degree of coherence of the ensemble of modes.

Sec. 4.2 describes the setup for data generation after a short recapitulation of coherence properties primarily for the sake of notational clarity. Section 4.3 details the algorithm and numerical implementation. The results of the numerical experiment are shown in Sec. 4.4 before the paper closes in Sec. 4.5 with a summary and outlook.

4.2. Simulation model

The basis for the physical model of partially coherent image formation is the representation of the probe's wavefield as a superposition of uncorrelated but coherent modes $\Psi_m \in \mathbb{C}$ [101, 114, 123] i.e the coherent mode expansion with $m \in \{1 \dots M\}$ denoting the mode index and Ψ_m satisfying orthogonality

$$\langle \Psi_m^*, \Psi_n \rangle = \delta_{nm} , \quad (4.1)$$

where $\langle \cdot, \cdot \rangle$ denotes the scalar product. The Ψ_m are propagated individually through free space by use of the Fresnel propagator \mathcal{D}_{Fr} and interact separately with optics or objects. Non-linear extensions of the model are beyond the scope of this paper and typically not relevant to x-ray imaging. In the detection plane, the intensities are computed for each mode

$$I_m = |\mathcal{D}_{\text{Fr}}(\Psi_m)|^2 , \quad (4.2)$$

and their incoherent superposition is taken to be the measurement \mathcal{I}

$$\mathcal{I} = \sum_m \lambda_m I_m, \quad (4.3)$$

where λ_m denotes the occupation number of Ψ_m , i.e the intensity for the mode. Equation (4.1) to Eq. (4.3) are sufficient to setup a straightforward numerical implementation for the propagation of a partially coherent probe. In order to determine the spatial coherence properties from the coherent mode expansion, we have to introduce auxiliary variables. We assume stationary and monochromatized undulator radiation, so that the equal-time coherence function or mutual intensity can be used

$$J_m(\vec{r}_1, \vec{r}_2) = \Psi_m^*(\vec{r}_1) \Psi_m(\vec{r}_2). \quad (4.4)$$

J_m has to be calculated for each mode Ψ_m with $\vec{r}_{1/2}$ points in the plane of Ψ_m . The collective $J(\vec{r}_1, \vec{r}_2)$ of the ensemble of modes is obtained by summing $J(\vec{r}_1, \vec{r}_2) = \sum_m J_m(\vec{r}_1, \vec{r}_2)$. Normalization yields the complex degree of coherence

$$j(\vec{r}_1, \vec{r}_2) = \frac{J(\vec{r}_1, \vec{r}_2)}{\sqrt{J(\vec{r}_1, \vec{r}_1)} \sqrt{J(\vec{r}_2, \vec{r}_2)}}. \quad (4.5)$$

Note, that this quantity is 4-dimensional. By assuming translational invariance and isotropy of the coherence properties we reduce the (\vec{r}_1, \vec{r}_2) dependence to a distance $d = \sqrt{\|\vec{r}_1 - \vec{r}_2\|^2}$ dependence. Using this simplification $j(d)$ is depictable in a $\|j(d)\|$ vs d plot, cf. Fig. 4.4. The spatial coherence length ξ is defined as the crossing point of $\|j(d)\|$ with a given threshold value, in this work 0.5.

Figure 4.1 shows a sketch of the setting for the case of 3 modes, represented by the iconic images of a 1,2 and 3. Following the MMP scheme, we need to generate \mathcal{I} for different propagation distances, or corresponding Fresnel numbers Fr_k , where the index $k \in \{1 \dots K\}$ is used to enumerate the K measurements \mathcal{I}_k . Figure 4.2(a) shows the input images which are processed to yield the orthogonal modes (b) for the numerical experiment. For each complex-valued input two images represented by $N_x \times N_y$ matrices are chosen. One is interpreted as phase $\phi \in [-0.4, 0.4]$ rad the other as amplitude $A \in [0.8, 1.2]$ arb.u. and then combined according to $A \cdot \exp(i\phi)$. Next, the inputs are reinterpreted as column vectors of a matrix $\underline{A} \in \mathbb{C}^{(N_x \cdot N_y) \times (M+1)}$, which is then fed into a QR -factorization. The QR -factorization is a method from linear algebra to compute the factorization $\underline{A} = Q \cdot R$, where $Q \in \mathbb{C}^{(N_x \cdot N_y) \times (M+1)}$ is a unitary matrix and $R \in \mathbb{C}^{(M+1) \times (M+1)}$ is a upper triangular matrix. The column vectors of the resulting Q are reshaped

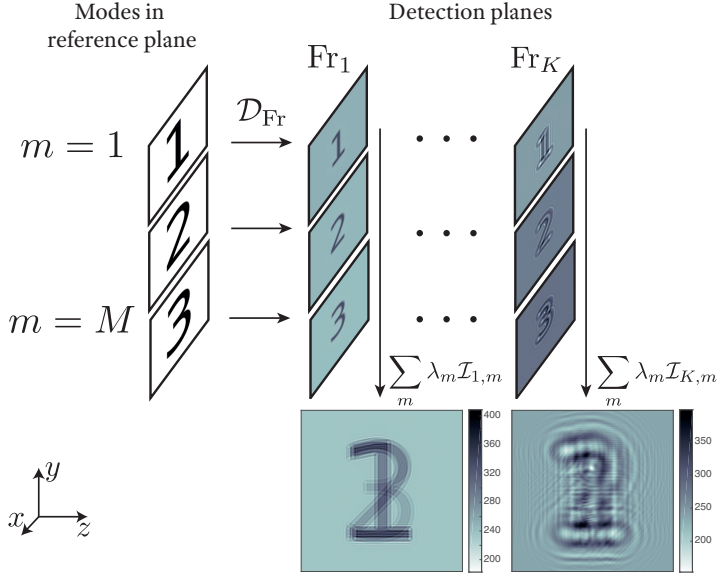
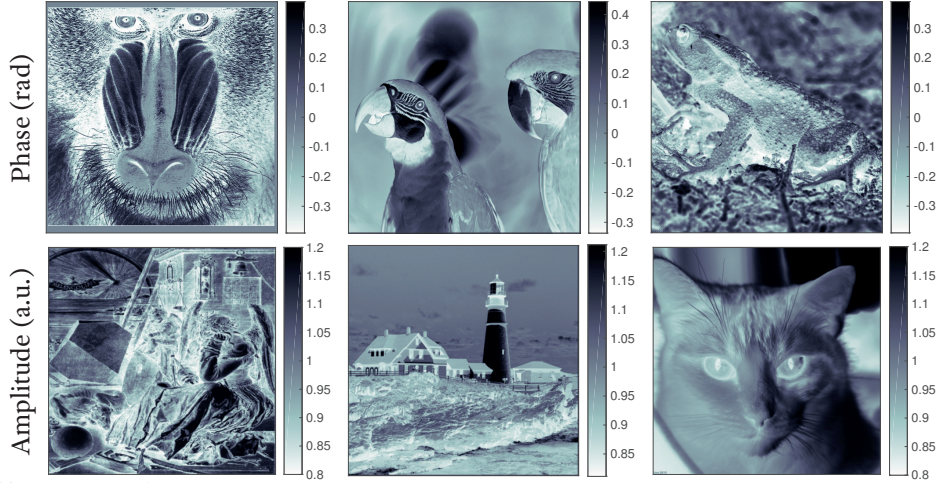


Figure 4.1.: Sketch of the data generation for the numerical experiment. (left) 3 exemplary modes, which are individually propagated to the detection planes at Fresnel numbers Fr_k (right). (bottom) The corresponding \mathcal{I}_k is formed by incoherently adding the individual intensities $I_{k,m}$.

to obtain $M + 1$ matrices of size $N_x \times N_y$ representing the orthogonal modes used for subsequent simulation of the measurements. The QR -factorization can be computed by different algorithms e.g. Gram-Schmidt process, Householder reflections or Givens rotations [124]. Since the QR -factorization makes the Ψ_m orthogonal with respect to the preceding mode, an additional mode has to be generated for initialization of the process, which does not contribute of the ensemble of modes used in the numerical experiment in Sec. 4.4. Thus, all subsequent QR -factorizations during the reconstruction operate only on the M propagation modes, which still form a orthogonal basis. The next step is to choose occupation numbers λ_m for the respective Ψ_m . For the example shown here, we choose $\lambda_m^0 = 4 \cdot 10^6 [0.5, 0.3, 0.2]$. Next, the modes are propagated Eq. (4.2) and summed up Eq. (4.3) to yield \mathcal{I}_k . As a final step of data generation noise can be applied. The set of \mathcal{I}_k is then be used as input for the reconstruction algorithm presented in the next section.

a) Input Images for Orthogonalization



b) Unitary modes

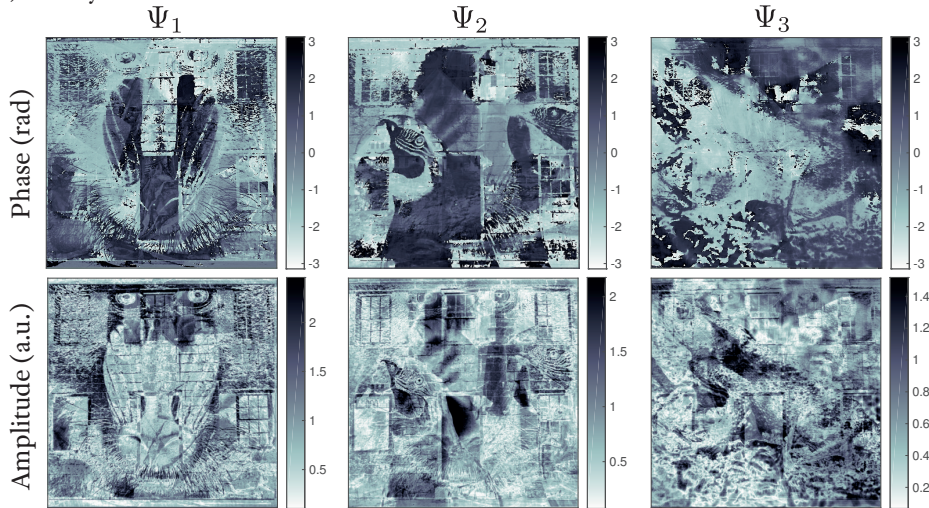


Figure 4.2.: Generation of coherent modes. Test images (a) were taken and interpreted as amplitudes and phases of the coherent modes. Using these modes as input for a QR-factorization, suitable, i.e. orthogonal, modes (b) are obtained for propagation and data generation, following the scheme introduced in Fig. 4.1. The modes are scaled according to their occupation number.

4.3. Algorithm

Given the measurements \mathcal{I}_k (intensity only), we aim to reconstruct the ensemble of modes $\vec{\Psi}$ with M modes Ψ_m with the respective occupation λ_m . This is an example of the classical phase problem, however, now in the setting of partial coherence. We solve this problem via the use of iterative projection algorithms [74, 125]. These algorithms are quite versatile, since the problem specific part is coded only in the projectors and the applicability is not limited to any specific assumptions as for single-step solutions cf. [20]. We here use the Relaxed Averaged Alternating Reflections (RAAR)-algorithm [73] with adapted projections. A new iterate is given by the RAAR-algorithm:

$$\vec{\Psi}_{n+1} = \frac{\beta_n}{2} \left(R_S(R_{\mathcal{I}}(\vec{\Psi}_n)) + \vec{\Psi}_n \right) + (1 - \beta_n) P_{\mathcal{I}}(\vec{\Psi}_n), \quad (4.6)$$

where $R_{S/\mathcal{I}}(\vec{\Psi}) = 2P_{S/\mathcal{I}}(\vec{\Psi}) - \vec{\Psi}$ denotes a (mirror) reflection by a given constraint set and n the iteration index. Operations acting on $\vec{\Psi}$ have to be read in a per-mode manner. The parameter β_n controls the relaxation. For the present problem we found that a fixed $\beta_n = 0.99$ is best suited to assure stability of the reconstruction process. The projection on the measurements $P_{\mathcal{I}}$ is a nested operation. The operation is carried out independently for each mode and measurement. The information from the overall K measurements for one mode is merged by taking the average over the projected wave fields. This has the advantage, that all \mathcal{I}_k constraints are 'equally well' satisfied whereas in a sequential projection the last constraint projected on is always preferred, in terms of a error metric. As a drawback we note that this parallel projection can diminish the speed of convergence. The single projection of Ψ_m on measurement K is given by

$$P_{\mathcal{I}_k}(\Psi_m) \equiv \mathcal{D}_{-\mathcal{F}\{r_k\}}(A_{\mathcal{I}_k}[\mathcal{D}_{\text{Fr}_k}(\Psi_m)]), \quad (4.7)$$

where $A_{\mathcal{I}_k}$ is the adaptation of amplitudes, given by

$$A_{\mathcal{I}_k}(\bullet) = \sqrt{\frac{I_{k,m}}{\sum_{m=1}^M I_{k,m}}} \cdot \sqrt{\mathcal{I}_k} \cdot \exp(i \arg(\bullet)), \quad (4.8)$$

where $I_{k,m} = |\mathcal{D}_{\text{Fr}_k}(\Psi_m)|^2$ denotes the intensity for a given Ψ_m in the measurement plane k , cf. Eq. (4.2). The whole adaptation has to be read as a per pixel operation. The propagation to the measurement plane is performed by the Fresnel

propagator \mathcal{D}_{Fr} for a given Fresnel number Fr with respect to one pixel,

$$\mathcal{D}_{\text{Fr}_k}(\bullet) = \mathcal{F}^{-1} [\mathcal{F}[\bullet] \exp((-i\pi)/(2\text{Fr}_k)(k_x^2 + k_y^2))], \quad (4.9)$$

where k_x and k_y are spatial frequencies in Fourier space. Thus $P_{\mathcal{I}}(\vec{\Psi}_n)$ is finally given as:

$$P_{\mathcal{I}}(\vec{\Psi}_n) \equiv \begin{cases} \frac{1}{K} \sum_{k=1}^K P_{\mathcal{I}_k}(\Psi_1) \\ \dots \\ \frac{1}{K} \sum_{k=1}^K P_{\mathcal{I}_k}(\Psi_M) \end{cases}. \quad (4.10)$$

The operator P_S is used to enforce the orthogonality constraint on $\vec{\Psi}$ in the reference plane. For this purpose, a QR factorization is applied (MATLAB's implementation) with the modes given as column vectors in Q and the occupation numbers λ_m given as the diagonal elements of R

$$P_S(\vec{\Psi}_n) = QR(\vec{\Psi}_n). \quad (4.11)$$

Finally, the updated $\vec{\Psi}$ are extracted from Q by reshaping the respective column m of Q back to the $N_x \times N_y$ array and subsequent multiplication with the corresponding m -th entry of R .

The algorithm was implemented in MATLAB, making use of the parallel computing toolbox and complemented with specialized CUDA (Compute Unified Device Architecture) kernels [126] running on the graphics processing unit for the calculation of the Fresnel propagator and $j(\vec{r}_1, \vec{r}_2)$. The implementation of mmMMP and the simulation described in the next section are available online [127].

4.4. Numerical experiment

The setup for the numerical experiment has been guided by the experimental results [109] obtained for the instrument [2] operated by our group at P10/PETRA III (DESY). In these previous results, a number of 3 coherent modes was found for the nano-focused undulator radiation of this instrument. This in line with earlier work on a dedicated high-coherence beamline[107]. For the numerical experiment, $M = 3$ modes are prepared and reconstruction is performed based on a set of $K = 10$ measurements with Fresnel numbers tabulated in Tab. 4.1. The orthogonal modes are shown in Fig. 4.2(b). The occupation numbers λ_m^0 and all other experimental parameters are also tabulated in Tab. 4.1. As initialization for $\vec{\Psi}$ we

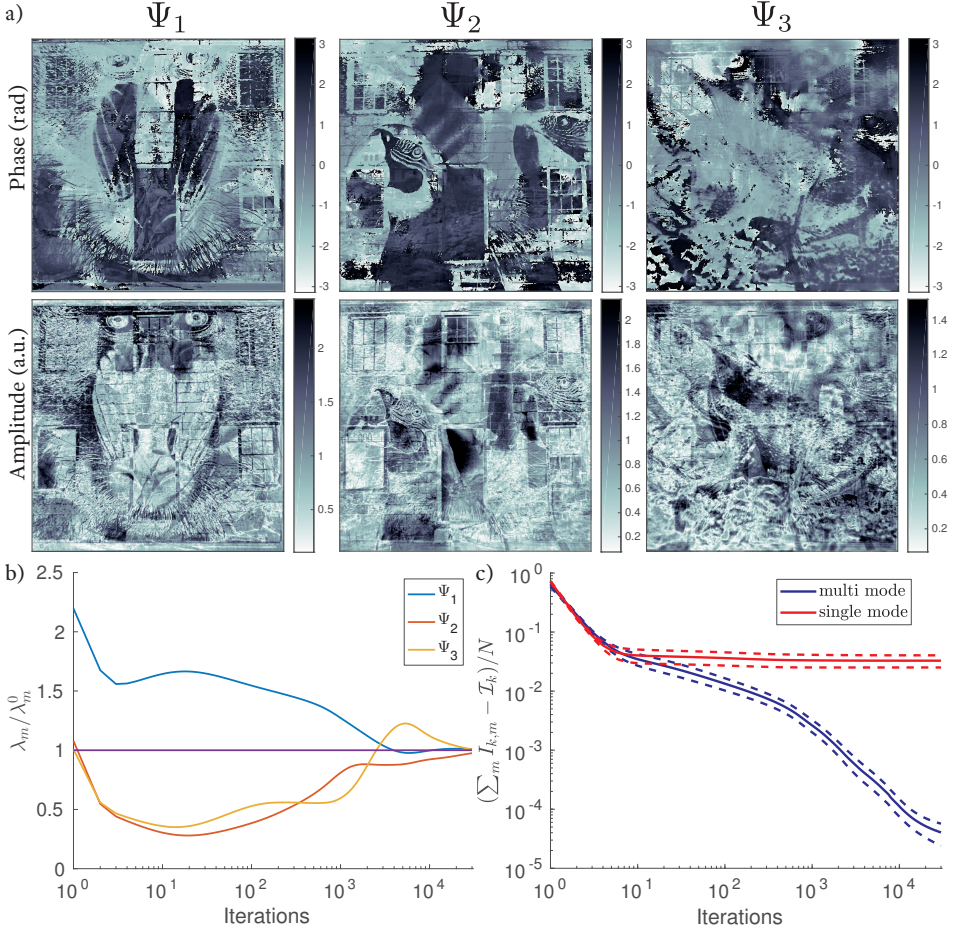


Figure 4.3.: Results of the mmMMP reconstruction. (a) The set of reconstructed modes in phase and amplitude. (b) The convergence graph for the occupation numbers λ_m . The convergence is shown relative to the current occupation in an iteration with respect to the prescribed occupation λ_m^0 . (c) Comparison of the error evolution Δ_k of the mean over all measurement planes Eq. (4.12) for a single mode reconstruction (red) and multi mode reconstruction (blue). Dashed lines indicate the bounds of the standard deviation over all measurement planes.

have generated 3 random modes orthogonalized by QR -factorization and scaled by an initial guess for the mode occupation λ_m . Figure 4.3 presents the results of the reconstruction after 30000 iterations with (a) showing the 3 recovered modes. Visual inspection by comparing the reconstructions to Fig. 4.2 demonstrates the successful reconstruction. Out of the three modes, Ψ_1 is recovered best, due to the fact that it has the largest occupation number. Ψ_2 and Ψ_3 also show a convinc-

ing recovery. However, some larger regions still exhibit a phase offset with respect to original. In Fig. 4.3(b) the evolution of the reconstructed occupation number λ_m/λ_m^0 , normalized to the true value, is plotted as a function of iteration number. The plot shows only a slow convergence for λ_m . Interestingly, the modes $\vec{\Psi}$ are faster recovered than their occupation numbers. The plot shows some characteristics which we found to be typical when testing different parameters (different M , K or λ_m^0): At the beginning Ψ_1 absorbs much of overall intensity and only following further iterations the intensity is distributed among the Ψ_m in a non-monotonous reconstruction trajectory, see also App. D. Figure 4.3(c) shows the per pixel error of the reconstruction with respect to the (simulated) measurements, calculated from

$$\Delta_k = \sum_{\text{all pixels}} \left| \sum_m I_{k,m} - \mathcal{I}_k \right|^2 / N. \quad (4.12)$$

The solid lines show the mean of Δ_k for the 10 measurement planes of the multi modal reconstruction (blue) presented here and a single mode reconstruction (red) assuming full coherence using the unmodified MMP scheme. The dashed lines show the bounds of Δ_k over all measurement planes. After 30000 iterations, the multi-mode reconstruction correctly taking into account partial coherence shows a residuum which is more than two orders of magnitude smaller than the reconstruction based on the (wrongful) assumption of full coherence, which is ubiquitous in x-ray propagation imaging.

With the reconstructed $\vec{\Psi}$ at hand, we can then calculate the equal-time complex degree of coherence j as shown in Fig. 4.4 using Eq. (4.5). Figure 4.4 compares $\|j(d)\|$ for input modes (blue) and the reconstructed modes (red). An important quantity for coherent imaging experiments is the (transversal) coherence length ξ . It can be defined via the intersection of $\|j(d)\|$ with a given value, here 0.5 (yellow).

The appendix provides additional parameter variations, i.e. addressing the influence of noise as well as a reduced input data set, to test the stability of the mmMMP algorithm. For the noisy simulations in App. A we chose a mean photon fluence per pixel μ with $\mu = \{1000, 100, 10\}$ but otherwise unchanged parameters (Tab. 4.1). The \mathcal{I}_k have been scaled accordingly, then the pixel values have been used as input for a Poissonian noise generator. Even for low fluences down to $\mu = 10$, we observe a satisfactory recovery of Ψ_1 and Ψ_2 , see Fig. 4.6. This surprising noise tolerance can be explained based on the fact that 10 measurements are used and that the images are highly sampled. Appendix B presents reconstruction results for a reduced input data set. Not surprisingly, more diverse

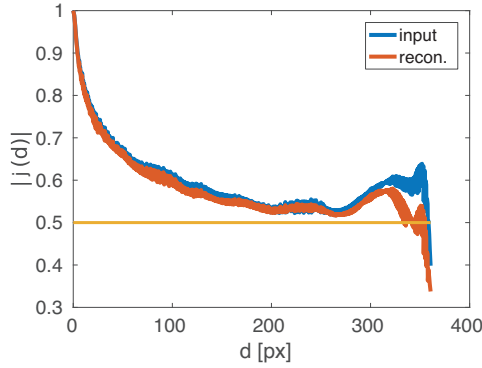


Figure 4.4.: Comparison of the degree of coherence $\|j(d)\|$ for the reconstructed modes (red) and input modes (blue).

input data leads to a better reconstruction quality and faster convergence of the algorithm, see Fig. 4.7 for an exemplary reconstruction. The simulations show that for a reliable reconstruction of 3 modes $K > 6$ is necessary. In both scenarios we note that a considerable higher number of iterations is needed to recover the ensemble of modes. The reconstruction scheme seems to be more stable against noisy data than for reducing the input data set. Appendix C surveys the influence of M on the reconstruction quality. We note an improvement of the reconstruction until the correct M is reached. Increasing M further does not improve or worsen the reconstruction. Appendix D shows the influence of the starting guess λ_m on the reconstruction. The different reconstruction trajectories show differences in convergence speed. A desired error level can be reached in this (ideal) setup by investing more iterations.

Table 4.1.: Summary of the parameters for the numerical experiment.

Parameter	Value
Number of modes M	3
Number of measurements K	10
Fresnel numbers Fr	0.0032 0.0020 0.0015
	0.0011 0.0009 0.0008
Occupation λ_m^0	0.0006 0.0005 0.0004 0.0003
Initial guess for occupation	$4 \cdot 10^6$ [0.5 0.3 0.2]
Image/Matrix size	$4 \cdot 10^6$ [0.6 0.25 0.15]
Iterations	1200^2 embedded 2048^2 px
	30000

4.5. Summary and outlook

We have presented an extended multi plane reconstruction scheme for near-field x-ray holography under conditions of partial coherence. We carried out numerical experiments primarily on noiseless and noisy data.

Our results show that reconstruction of the coherent near-field modes is possible and that quantities as the coherence length and occupation numbers can be faithfully reconstructed, given sufficient longitudinal diversity of the measurements, i.e. a sufficient number of detection planes. Furthermore, our results clearly demonstrate the increased reconstruction quality which can be obtained when data recorded under condition of partial coherence is also reconstructed in a multi-modal approach, instead of the assumption of a single mode. While near-field imaging is known to be more tolerant towards partial coherence than its far-field counterpart, the present work shows that it is still important to go beyond the idealized assumption of full coherence. In the present work, we have also tested how the reconstruction quality decreases when the number of measurements K is decreased. Of course, the number of measurements planes scales with the number of modes. In fact, it can be expected that $K > 2 \times M$. In our numerical experiments for $M = 3$, we found indeed that $K = 8$ still resulted in good reconstructions, however, requiring a larger number of iterations (cf. App. B).

Following this work, two next steps suggest themselves: First, the new algorithms and approach should be tested experimentally. Second, probe reconstruction as presented here should be extended to full reconstruction of object and probe, as it has already been shown for the far field.

4.6. Appendix A: Mode reconstructions from noisy measurements

Reconstruction was tested under the influence of noise for photon fluences of $\mu = \{10, 100, 1000\}$ photons per pixel, again using modes shown in Fig. 4.2. The measurements \mathcal{I}_k were generated for the set of Fresnel numbers Fr_k (cf. Tab. 1) as detailed in the manuscript (cf. Sec. 2). The \mathcal{I}_k were then rescaled according to μ and used as input for MATLAB's `imnoise`-function. Figure 4.5 shows an example for these measurements. The set of resulting noisy \mathcal{I}_k was then used as input for mmMMP. Figure 4.6 shows the obtained mode reconstructions from these input data. The reconstructed modes presented in (a) show good recovery for Ψ_1 but

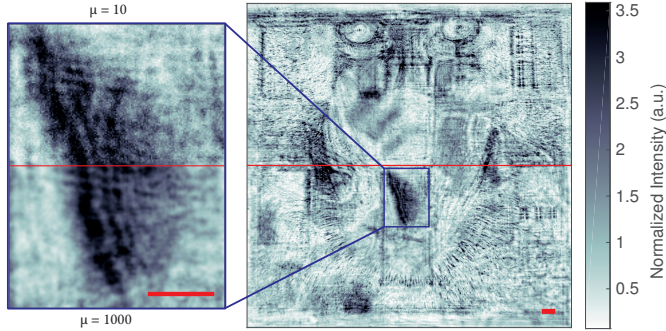


Figure 4.5.: Example for a noisy measurement at $Fr = 3.2 \cdot 10^{-3}$. (top) The realization for $\mu = 10$ photons per pixel and (bottom) $\mu = 1000$ photons per pixel. The insert (left) shows the loss of feature visibility in the hologram by noise. Note, that for representation purposes, the intensities have been rescaled by their mean value. Scale bar indicates 50 px.

significant deviations for Ψ_2 and Ψ_3 . For high fluence $\mu = 1000$, the reconstruction error Δ shown in (b) exhibits a similar functional form as for the noiseless case in the main text, but it does not quite reach the same error level (after 30000 iterations). The reconstruction for $\mu = 10$ seems to stagnate, even if we let it run over a considerable amount of more iterations (95000 iterations). Nevertheless, the reconstruction result shown in (c) after 95000 iterations for Ψ_3 (left) compares surprisingly well with the original Ψ_3 (right).

4.7. Appendix B: Mode reconstructions from a reduced data set

Next, the influence of a reduced data set was studied, to this end the number of measurements K was reduced. The mode reconstruction was carried out on noiseless measurements simulated from the modes shown in Fig. 2. Starting from the initial set of Fr_k (Tab. 1), tailing Fr have been removed until the new K is reached. The simulated cases $K = 6$ and $K = 8$ are presented in Fig. 4.7. The reconstructed modes after 50000 iterations are shown in (a), the left half for $K = 6$ and the right half for $K = 8$, respectively. While the reconstructed amplitude and phase for Ψ_1 is acceptable for $K = 6$, the other modes are not reconstructed. In the corners of Ψ_2 and Ψ_3 some details of a window appear, but the majority of the mode is noise. Increasing the iteration number, in this case to $n = 550000$, did not improve the mode reconstruction significantly. Contrarily, for $K = 8$ we still

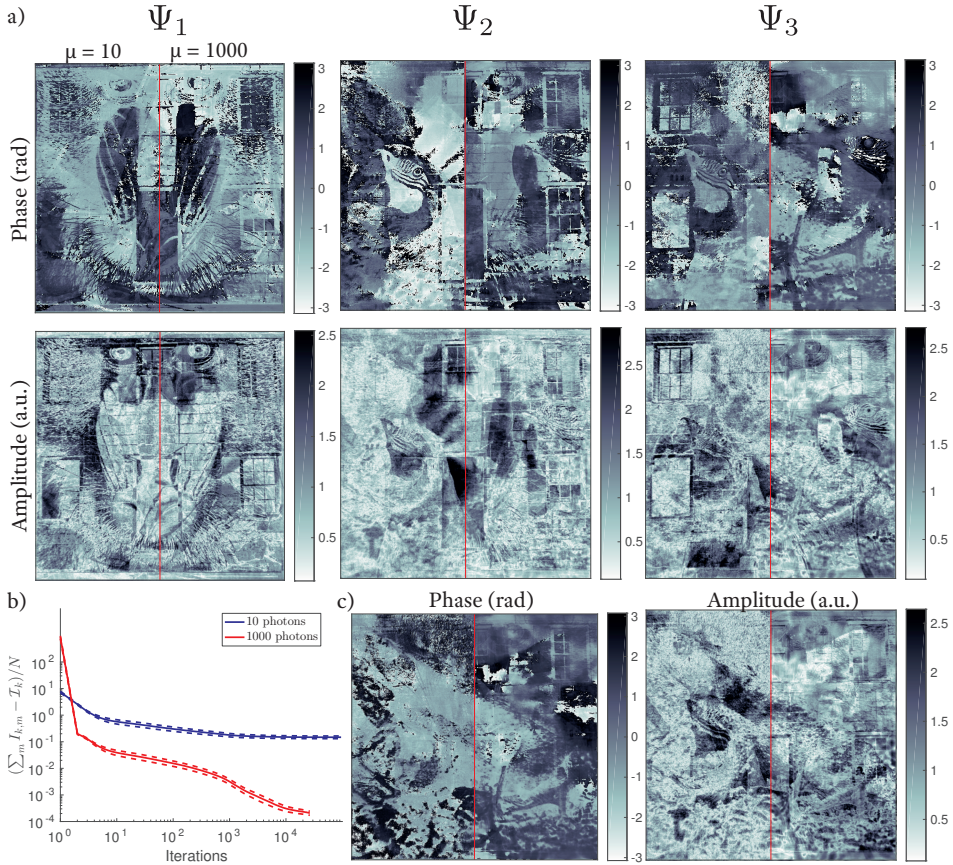


Figure 4.6.: Results obtained from noisy data. (a) Reconstructed modes in phase and amplitude. The left half shows the reconstruction for $\mu = 10$ and the right for $\mu = 1000$. The amplitudes have been normalized by the mean value for the side-by-side plot. (b) Error Δ as a function of iteration n , for both photon numbers. Dashed lines indicate the bounds of the standard deviation over all measurement planes. (c) Reconstruction of Ψ_3 for $\mu = 10$ after 95000 iterations (left) compared to the input mode (right), cf. Fig. 2 of the main manuscript.

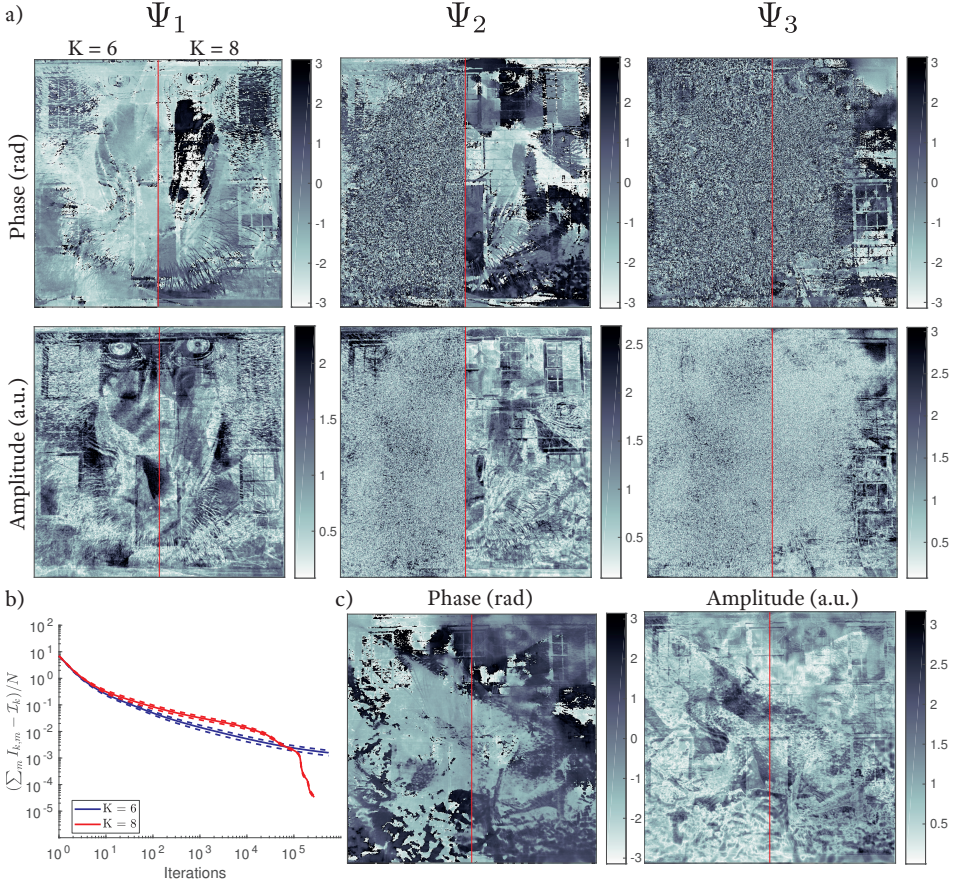


Figure 4.7.: Results obtained from the reduced input data set. (a) Reconstructed modes in phase and amplitude after 50000 iterations. The left half shows the reconstruction for $K = 6$ and the right for $K = 8$. (b) Error evolution for both K as function of iteration number. Dashed lines indicate the bounds of the standard deviation over all measurement planes. (c) Reconstruction of Ψ_3 for $K = 8$ after 270000 iterations (left) compared to the input mode (right), cf. Fig. 4.2.

observe good recovery for Ψ_2 , but Ψ_3 also shows noise artifacts in the middle of the image. Letting the algorithm run for more iterations in this setting (270000 iterations) yielded a reconstruction of similar quality as the one in main text.

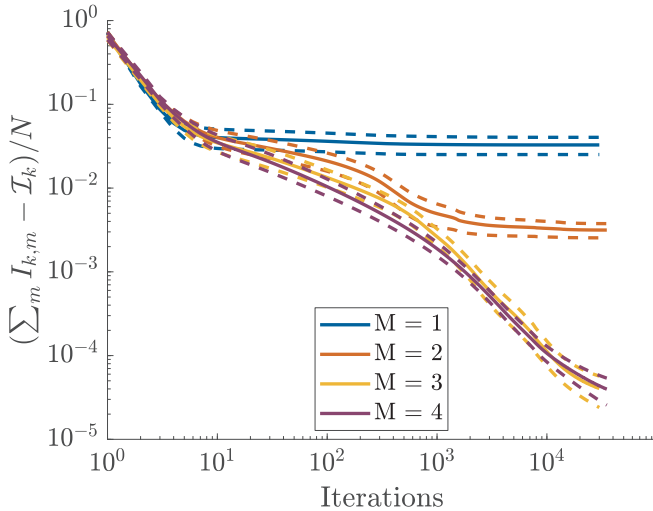


Figure 4.8.: Influence of the choice of M on Δ_k . The results for $M = 1$ and $M = 3$ are already shown in Fig. 4.3(c). The results for $M = 2$ and $M = 4$ have been added. Solid lines indicate the mean error $\bar{\Delta}_k$ over all \mathcal{I}_k . Dashed lines indicate the bounds of the standard deviation over all measurement planes.

4.8. Appendix C: Influence of the choice of M for reconstruction

The number of reconstructed modes M is an important parameter for physical interpretation of data. Here we have complemented the results of Fig. 4.3(c) with a variation of the number of modes M for multiple runs on the same (simulated) data set. Again the parameters listed in Tab. 4.1 have been used, no noise has been added to \mathcal{I}_k . The results are shown in Fig. 4.8, again we use Δ_k according to Eq. (4.12) to monitor the error. The presentation of results follows Fig. 4.3(c), see the main text. The results show the better description of the \mathcal{I}_k by increasing M . For $M = \{1, 2\}$ we note stagnation of the error, the $M = 2$ curves shows already that the stagnation is reached later and that the data is better described. For $M = \{3, 4\}$ we see no stagnation of the error. The $M = 4$ curves shows no better description of the data. From these results it is possible to deduce $M = 3$, also for experimental data where M is not known beforehand.

4.9. Appendix D: Influence of the initial guess of λ_m for reconstruction

Besides M and the initialization of Ψ_m , i.e. orthogonal and random, a starting guess for λ_m has to be chosen. Here we have tested the stability of the algorithm with regard to different choices of the starting initialization of λ_m . In the first case all Ψ_m have the same occupation λ_m i.e. $\lambda_m = \frac{1}{M} \cdot \text{number of photons}$. The results for this equal occupation reconstruction are shown in Fig. 4.9, the structure follows Fig. 4.3. The reconstruction with equal occupation as starting guess reproduces the reconstruction shown in Fig. 4.3. Further we have tested randomly chosen initializations. Here we have chosen random initializations for λ_m for the setting of $M = 3$ as described in the main text. The λ_m have been chosen as follows:

- Generate M random numbers A_m .
- Sort A_m in descending order.
- generate the normalized occupation $\widehat{\lambda}_m = \frac{A_m}{\sum_{m=1}^M A_m}$.
- Calculate $\lambda_m = \widehat{\lambda}_m \cdot \text{number of photons}$.

Figure 4.10(a) shows the trajectories of the relative occupation λ_m/λ_m^0 for randomly chosen starting guess of λ_m . The numbers in the legend for each panel denote the $\widehat{\lambda}_m$. The normalized occupation of the searched ensemble of modes is $\widehat{\lambda}^0 = \{0.5, 0.3, 0.2\}$. The ensemble of realizations shows that the algorithm is stable against variations in the starting guess of λ_m . (b) shows a longer run for the realization $\widehat{\lambda}_m = \{0.487, 0.291, 0.222\}$. After 30000 iterations this reconstruction has not yet shown satisfactory recovery of the occupation numbers. Running more iterations, overall 100000, has finally yielded a good recovery of the occupation. The true occupation can be recovered, in unfavorable cases at the expense of more iterations.

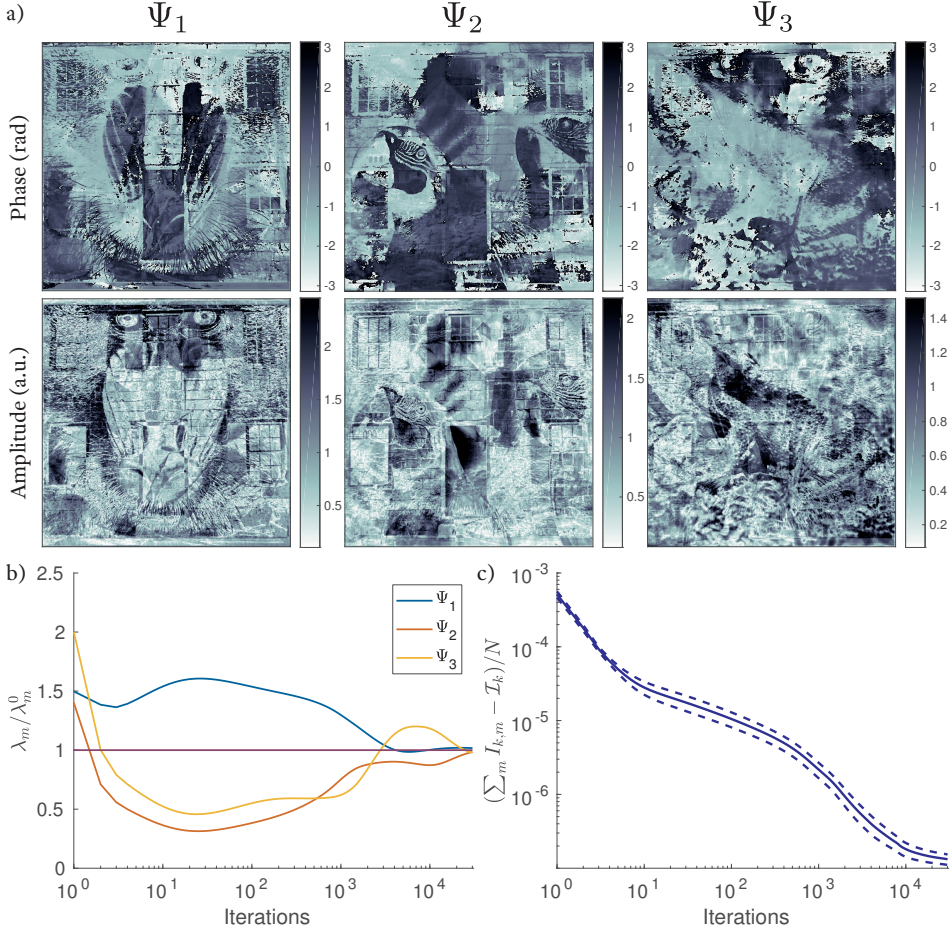


Figure 4.9.: Results of the equal occupation reconstruction. (a) The set of reconstructed modes in phase and amplitude. (b) The convergence graph for the occupation numbers λ_m . The convergence is shown relatively to the current occupation in an iteration with respect to the prescribed occupation λ_m^0 . (c) Comparison of the error evolution Δ_k of the mean over all measurement planes Eq. (4.12) for a single mode reconstruction (red) and multi mode reconstruction (blue). Dashed lines indicate the bounds of the standard deviation over all measurement planes.

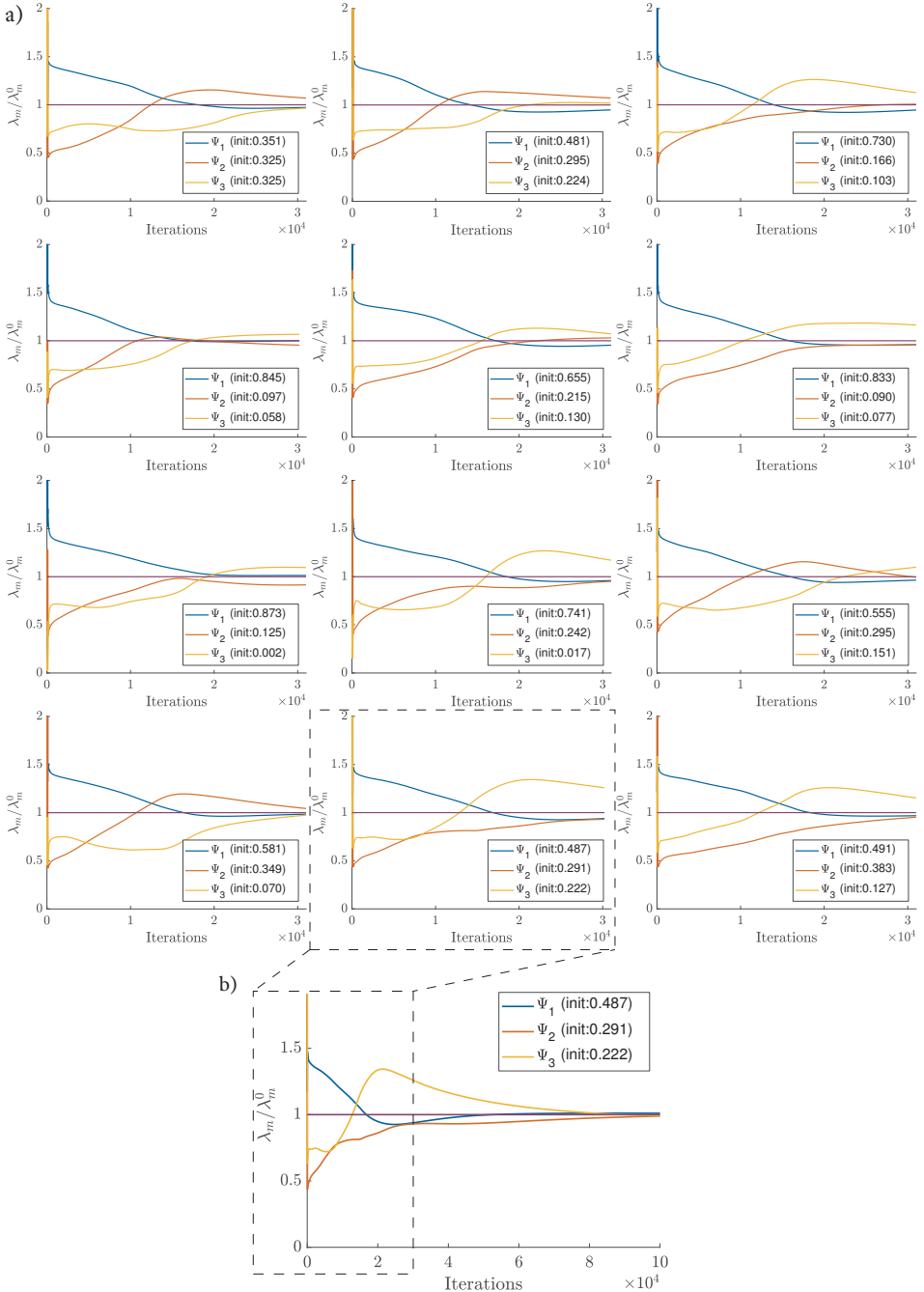


Figure 4.10.: Trajectories for the realizations of λ_m . The individual trajectories (a) of the relative occupation λ_m/λ_m^0 for overall 12 realizations are shown, using the parameters listed in Tab. 1. The realization with $\widehat{\lambda}_m = \{0.487, 0.291, 0.222\}$ showing not satisfactory convergence after 30000 iterations, has been iterated 70000 iterations more (b).

Funding Information

Deutsche Forschungsgemeinschaft (DFG) (SFB 755); Bundesministerium für Bildung und Forschung (BMBF) (05K16MGB).

Acknowledgments

We thank Markus Osterhoff and Aike Ruhlandt for fruitful discussions. We thank Jan Goeman for keeping the number crunching machines up and running.

5. Divide and Update: Towards Single-Shot Object and Probe Retrieval for Near-Field Holography

Johannes Hagemann and Tim Salditt

Reproduced from *Optics Express* (2017) **25**, 20953 – 20968

We present a phase reconstruction scheme for X-ray near-field holographic imaging based on a separability constraint for probe and object. In order to achieve this, we have devised an algorithm which requires only two measurements – with and without an object in the beam. This scheme is advantageous if the standard flat-field correction fails and a full ptychographic dataset can not be acquired, since either object or probe are dynamic. The scheme is validated by numerical simulations and by a proof-of-concept experiment using highly focused undulator radiation of the beamline ID16a of the European Synchrotron Radiation Facility (ESRF).

5.1. Introduction

X-ray near-field holographic imaging (NFH) enables single shot, full-field imaging of specimen with nanoscale spatial resolution [5, 89]. Sharing the characteristic advantages of high penetration and quantitative contrast with other x-ray imaging modalities, it can in addition exploit the advantage of high temporal resolution down to single pulse imaging with synchrotron (SR) and free electron laser (FEL) radiation [128, 129]. This is for the simple reason, that a full wavefield can be probed in a single shot without scanning. Figure 5.1 depicts the setup of NFH using highly focused SR or FEL radiation. By choice of the source to object distance z_1 and the object to detector distance z_2 , the geometric magnification $M = (z_2 + z_1)/z_1$ and the field of view (FOV) can be tailored to the experimental need.

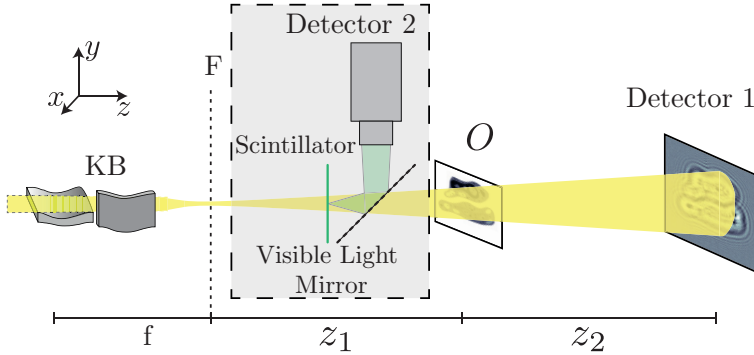


Figure 5.1.: Schematic of an experimental setup for near-field holography. Near-field holographic images are recorded with detector 1 at distance z_2 behind the object O , mounted on a motorized stage in defocus position z_1 behind the focal plane F of a Kirkpatrick-Baez mirror (KB) system with focal distance f . The dashed box shows the extension to a parallel acquisition setup. The two measurements $|\mathcal{D}_{\text{Fr}}(\Psi)|^2$ and $|\mathcal{D}_{\text{Fr}}(P)|^2$ can be acquired in single-shot by the use of a semi-transparent second detector. This Detector 2 is positioned front of O to record the illuminating probe. This experimental geometry is proposed for single-pulse FEL full field imaging scheme. For further discussions refer to the main text.

A major challenge in NFH is the fact that the validity of phase retrieval and hence image quality depends crucially on the quality of the illumination. Due to the finite source-size, a number of unwanted effects can arise, such as distortions in the wavefront or a partial coherent illumination, but also geometrical optical effects such as astigmatism. For example, focusing by elliptically shaped multilayer mirrors in Kirkpatrick-Baez geometry [21] is accompanied by unwanted phase distortions in the incoming X-ray probe induced by deviations from the ideal height profile of the mirrors [122]. After free space propagation to the imaging or detection plane, the phase errors result in a measurable intensity pattern, which often appears as pronounced horizontal and vertical stripes due to the two orthogonal mirrors, see Fig. 5.2 for an example of an empty beam pattern. In other types of focusing similar distortions arise. Focusing is required to generate the diverging illumination for high magnification and resolution. Note that also for parallel beam propagation imaging it is extremely common to implicitly assume perfect plane wave illumination by performing the conventional flat-field correction [128, 130–134]. In previous studies, we have shown that under these conditions the commonly used standard flat-field correction, i.e. the division of measured intensities with the specimen in the beam by measured intensities without specimen in the beam, induces artifacts

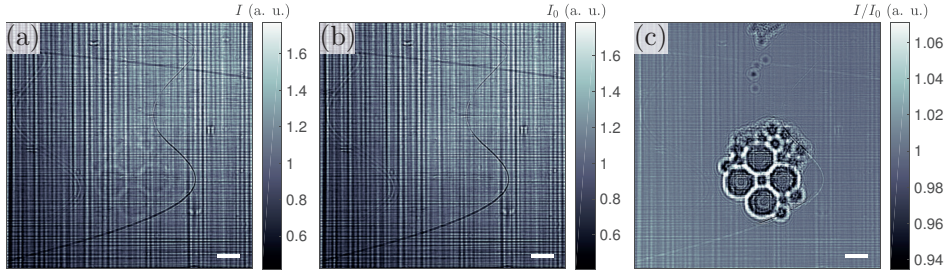


Figure 5.2.: Experimental data used for phase retrieval by d&u. (a) Recorded near-field intensity pattern with the object in the beam, i.e. $|\mathcal{D}_{\text{Fr}}(\Psi)|^2$. (b) Same without object, i.e. $|\mathcal{D}_{\text{Fr}}(P)|^2$. For comparison we also show (c) the flat-field correction of the object's hologram as obtained by dividing $|\mathcal{D}_{\text{Fr}}(\Psi)|^2$ by $|\mathcal{D}_{\text{Fr}}(P)|^2$. The scale bar indicates $5\ \mu\text{m}$.

[53, 54], as illustrated in Fig. 5.2(c). To overcome these problems, the experimentalist can choose between two principal strategies: (i) corrections by a refined optical system (hardware), or (ii) corrections by enhanced algorithms (software). The hardware solution can consist in the simplest case by additional apertures to cut off typical intensity tails in the focal plane. A more sophisticated solution is the use of x-ray waveguides (WG) [135], which act as coherence and wavefront filters [136], providing improved illumination schemes for NFH [56, 79, 137]. This advantage comes at the cost of a reduced photon flux, and increased acquisition time. The algorithmic approach by ptychography, on the other hand, solves the flat-field problem by a precise reconstruction of the complex-valued illumination. In the language of ptychography the illumination is called the probe P . To this end multiple exposures of the specimen, or in ptychographic terms of the object O , are acquired at different transversal positions in the beam. This position scanning is extensive, since an overlap between 60% to 85% is necessary for proper convergence of the ptychographic algorithm [138], depending on experimental modalities. This applies for the far-field [12, 139] case of ptychography and its extensions to NFH [65, 76]. Ptychography can also account for other non ideal states (e.g. lack of coherence) of the probe or object [99, 140]. Associated with longer scanning time is also a larger data set, which has to be acquired by transversal and/or longitudinal (for the near-field) scans of O in order to generate sufficiently diverse input data for the simultaneous reconstruction of P and O . The scanning also imposes a higher dose on O , compared to NFH [141], which can induce radiation damage and lead to an inconsistent ptychographic dataset. Most importantly, the scanning scheme is incompatible with time-resolved studies and with ultra-fast (single shot)

imaging. Note that some objects are deliberately destroyed by the first pulse, using the 'diffract-before-destroy' strategy used in some schemes of FEL imaging [33, 142, 143]. A further problem for ptychography at FEL is the intrinsic shot-to-shot variation of P , resulting from pulse generation by the SASE process [144].

In this work we seek to make single shot NFH compatible with non-stationary probes and in particular FEL imaging. To this end, we propose a new algorithmic approach. The reconstruction of object and probe is based on two intensity recordings: (i, exit wave) of the object in the beam and (ii, probe) of the empty beam without object. The exit wave $\Psi = P \cdot O$ is written as separable product of P and O . This implies that the product approximation holds, this is in general true for thin and especially biological specimen [145]. The proposed algorithm uses the separability constraint known from ptychography, and an intertwined update scheme operating on both images, which we denote by divide&update (d&u).

We show by simulation and experimentally that d&u yields an improved reconstruction quality of O compared to a reconstruction obtained from the same data using the standard flat-field correction as data preprocessor. The two images can be recorded either sequentially or simultaneously (parallel recording). As the probe stability was sufficiently high in the SR experiment serving as proof-of-concept in this work, we have used the sequential recording which is easier since no special detection scheme is necessary. In the case of parallel recording as required for single pulse FEL imaging, a semi-transparent detector screen in front of the object (denoted by detector 2 in Fig. 5.1) could be used, or a beam splitter in front of O to split the XFEL pulse before it interacts with O [146, 147].

For this purpose, a semi-transparent detection screen or beam splitter has to be placed in front of the object. There are two challenges to consider: Firstly, the sensor resolution has to sample the probe sufficiently well. Secondly, the heat load for the semi-transparent screen must be kept at a reasonable level. Both are difficult, if the detection screen is too close to the focal plane of a nano-focus optic. However, the 'probe detector' can equally well be placed in the convergent beam, e.g. directly behind the focusing device where the beam is extended, and where a field of view of several hundred micrometer could be probed with sufficient spatial sampling. In this case, the reconstruction requires additional propagation of the wavefields by Fresnel propagators, as also demonstrated in this work for simulated data in App. A.

The paper is structured as follows: Section 5.2 details the d&u scheme. Section 5.3 tests the algorithm on simulated data, before application to experimental data. The paper closes with summary and outlook in Sec. 5.4.

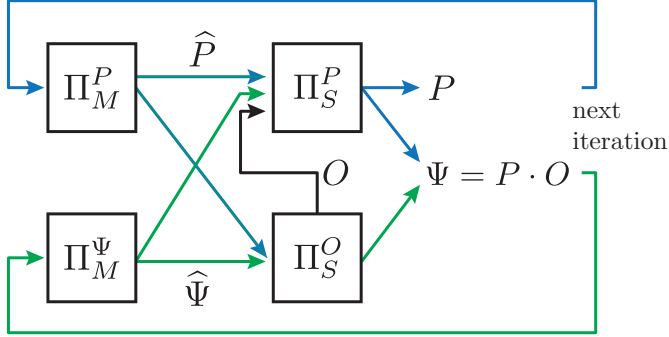


Figure 5.3.: Sketch of the algorithmic scheme of divide&update (d&u). The algorithm uses the two measurements $|\mathcal{D}_{\text{Fr}}(\Psi)|^2$ and $|\mathcal{D}_{\text{Fr}}(P)|^2$ as inputs. An iteration starts with the projection of the guesses for P and Ψ on the measured intensities using the projectors Π_M^P and Π_M^Ψ (left). After projection, the output fields \hat{P} and $\hat{\Psi}$ are used in a cross-over manner to update P and O in Π_S^O and Π_S^P (middle), which are then multiplied to form the Ψ for the next iteration (right).

5.2. Algorithm

As in other ptychographic approaches, the d&u algorithm uses the separability constraint in the plane of O . Figure 5.3 shows a principle sketch of d&u and Alg. 1 details the algorithmic approach.

In conventional NFH, when dealing with distorted probes the approximative hologram of O [54] is recovered by flat-field correction and then used as input for a phase reconstruction algorithm. In contrast to this standard approach we make use of the two available measurements in an iterative reconstruction scheme, cf. Fig. 5.3. Following the separability idea of ptychography we use amplitude adapted version $\hat{P}_n = \Pi_M^P(P_{n-1})$, $\hat{\Psi}$ analogously, to yield updates for P_n and O_n in a cross-over manner (middle) by use of constraints for O in the plane of the object. With the new P_n and O_n we generate the updated exit wave Ψ and start a new iteration.

The projection on the measurements $\Pi_M^\mathcal{X}(\bullet)$, with \mathcal{X} being either $|\mathcal{D}_{\text{Fr}}(\Psi)|^2$ or $|\mathcal{D}_{\text{Fr}}(P)|^2$, i.e. the respectively measured near field pattern, is given by the standard magnitude projector

$$\Pi_M^\mathcal{X}(\bullet) \equiv \mathcal{D}_{\text{Fr}}^{-1} \left(\mathcal{X}^{1/2} \cdot \exp(i \cdot \arg[\mathcal{D}_{\text{Fr}}(\bullet)]) \right), \quad (5.1)$$

applied to the respective iterate of P or Ψ . The propagation to the detection plane

is performed by the Fresnel free space propagator

$$\mathcal{D}_{\text{Fr}}(\bullet) = \mathcal{F}^{-1} [\mathcal{F}[\bullet] \exp((-i\pi)/(2 \text{Fr})(k_x^2 + k_y^2))], \quad (5.2)$$

where $k_x = 2 n_x/N_x$ and $k_y = 2 n_y/N_y$ are spatial frequencies in Fourier space with $n_{x,y} \in [-N_{x,y}/2 \dots N_{x,y}/2]$, $N_{x,y}$ are the dimensions of the image, \mathcal{F} the Fourier transformation and Fr is the Fresnel number with respect to one pixel (px).

Algorithm 1 Divide and Update algorithm

- 1: $O_0 \leftarrow \mathbb{1}_{N_x \times N_y}$ ▷ Initialization
 - 2: $P_0 \leftarrow \mathbb{1}_{N_x \times N_y}$
 - 3: **for** $n = 1 \dots n_{max}$ **do**
 - 4: $\widehat{P}_n \leftarrow \Pi_M^P(P_{n-1})$ ▷ Carry out amplitude adaption
 - 5: $(\widehat{\Psi})_n \leftarrow \Pi_M^\Psi((\Psi)_{n-1})$
 - 6:
 - 7: Compute Π_S^O :
 - 8: $O'_n \leftarrow (\widehat{\Psi})_n / \widehat{P}_n$ ▷ Divide for O , i.e. enforce separability
 - 9: $O_n \leftarrow \Pi_O(O'_n)$ ▷ and apply constraints
 - 10:
 - 11: Compute Π_S^P :
 - 12: $P'_n \leftarrow \left(\frac{(\widehat{\Psi})_n}{O_n} + \widehat{P}_n \right) / 2$ ▷ Divide for P
 - 13: $P_n \leftarrow \Pi_P(P'_n)$ ▷ and apply constraints
 - 14:
 - 15: $(\Psi)_n \leftarrow P_n \cdot O_n$ ▷ New exit wave
 - 16: **end for**
-

The details of the cross-over update are given in pseudo code in Alg. 1 in line 7-13, the corresponding projectors Π_S^O and Π_S^P are detailed below. The operator Π_S^O is used to update the iterate for O . First the fields are separated by division (line 8), enforcing separability. Next, the projector Π_O is used to enforce the constraints on O , i.e. pure, negative phase and support constraint.

$$\Pi_O(\bullet) = \begin{cases} \exp(i \cdot \arg(\bullet)) & \text{for pixel} \in S \\ \exp(i \cdot 0) & \text{for pixel} \notin S \vee \arg(\bullet) > 0 \end{cases} \quad (5.3)$$

Here the support S is assumed to be known, but additional refinements as shrink-wrap can be easily implemented to refine S . In practice, the support is easily generated from the conventional approach of empty beam correction, followed by holographic reconstruction. Note, that any other known constraint on O can be incorporated as well.

Next, P is updated using Π_S^P . The new O_n is used to separate P_n taking also \widehat{P}_n into account (line 12). In a general setting, we can only use the information from \widehat{P} and the division of $\widehat{(\Psi)}_n/O_n$. However, in contrast to the general setting, one often has quite powerful constraints at hand on P , depending on the experimental situation, for example smoothness or small distance with respect to a temporal averaged probe, which would of course further improve convergence. The smoothness of P is generated by the blurring of free-space propagation. It can be estimated from the power spectral density to choose a suitable full width at half maximum (FWHM) value of a Gaussian filter. The filter is respectively applied on the phases and amplitudes of P . Afterwards the filtered amplitudes and phases are recombined. In the presence of strong fluctuations in P multiple recordings $|\mathcal{D}_{\text{Fr}}(P)|^2$ can be combined to an averaged P . By comparing the current iterate of P with the average P it is possible to discriminate variations larger than a given threshold and set these to the average value. These constraints can be additionally enforced as part of Π_P on P'_n (line 13). The updated exit wave $(\Psi)_n$ is calculated by multiplying P_n and O_n (line 15). The Matlab implementation of the algorithm is provided in Code 1 (Ref. [148]).

5.3. Results

5.3.1. Simulated data

Figure 5.4 shows the phantoms used for testing the algorithm. A sketch of two cells (a) [98] serves as pure phase phantom of the object. For the probe phantom, a mandrill test image (b), and Dürer's Melancholia I (c), serve to define phases and amplitudes, respectively. Both images are Gaussian low-pass filtered with a filter of FWHM of 5 px diameter to simulate the smoothing of a probe by propagation. To simulate the finite size of the illumination the amplitudes have been multiplied by a Gaussian window of a FWHM with 354 px. The images have size of 512×512 px² embedded in $N_x \times N_y = 2048 \times 2048$ px² for propagation. Only the central parts (512×512 px²) of the images are shown in this and the following figures.

The simulated measurements are depicted in Fig. 5.5 i.e. (a) $|\mathcal{D}_{\text{Fr}}(\Psi)|^2$ and (b) $|\mathcal{D}_{\text{Fr}}(P)|^2$ for a Fresnel number of $\text{Fr} = 10^{-3}$. Afterwards, Poissonian noise for a fluence $\mu = 200$ photons/pixel (ph/px) has been added to the measurements. $|\mathcal{D}_{\text{Fr}}(\Psi)|^2$ does not show a visible imprint of the propagated object, due to the comparative small, but for biological specimen reasonable [98] phase shift.

The approximated hologram is obtained by the standard flat-field correction i.e.

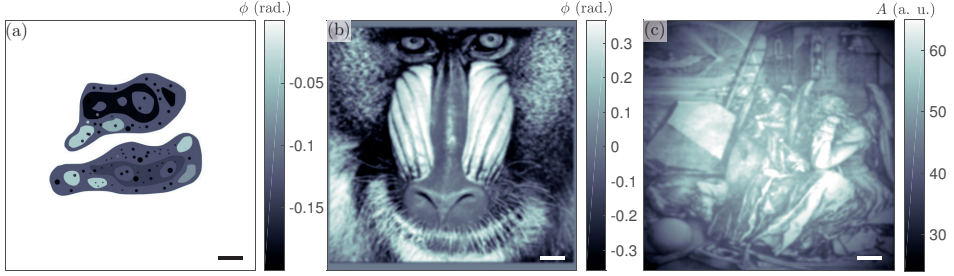


Figure 5.4.: Phantoms used for the simulation. (a) Phases of the object (pure phase contrast) with $\phi \in [-0.2 \ 0]$ rad. (b) Phases of the probe. (c) Amplitudes of the probe. The gray values of the input images are scaled to match phases $\phi \in [-0.4 \ 0.4]$ rad and amplitudes $A \in [0.8 \ 1.2]$. Amplitude and phase phantom images have been frequency filtered by a Gaussian with FWHM of 5 px. In addition, the amplitudes are multiplied with a Gaussian of 354 px FWHM to simulate an intensity decay. The scale bar indicates 50 px.

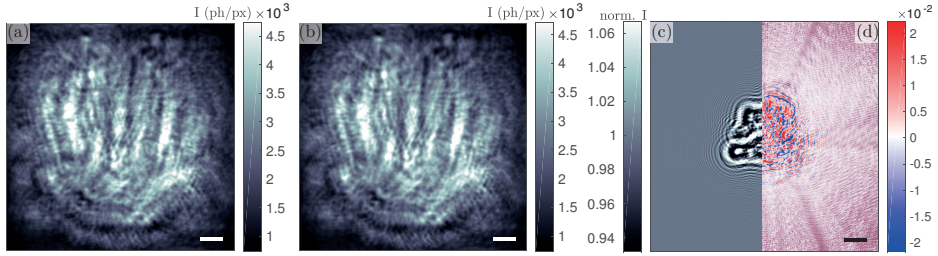


Figure 5.5.: Simulated input data for the simulations at $Fr = 10^{-3}$ with $\mu = 200$ ph/px, using the phantoms from Fig. 5.4. The measurements of (a) $|\mathcal{D}_{Fr}(\Psi)|^2$ and (b) $|\mathcal{D}_{Fr}(P)|^2$. The scale bar indicates 50 px. (c) The approximated hologram $|\mathcal{D}_{Fr}(\Psi)|^2/|\mathcal{D}_{Fr}(P)|^2$. (d) Relative error of (c) to the real hologram $|\mathcal{D}_{Fr}(O)|^2$. The scale bar indicates 100 px.

$|\mathcal{D}_{Fr}(\Psi)|^2/|\mathcal{D}_{Fr}(P)|^2$ and is shown in (c). This reveals the small contrast range of the imprint. The relative per pixel error of the approximated to the ideal hologram

$$\delta = \frac{(|\mathcal{D}_{Fr}(\Psi)|^2/|\mathcal{D}_{Fr}(P)|^2 - |\mathcal{D}_{Fr}(O)|^2)}{|\mathcal{D}_{Fr}(O)|^2} \quad (5.4)$$

is shown in (d). The absolute error is

$$\left(\sum_{\forall \text{pixels}} \left| |\mathcal{D}_{Fr}(\Psi)|^2/|\mathcal{D}_{Fr}(P)|^2 - |\mathcal{D}_{Fr}(O)|^2 \right|^2 \right)^{1/2} = 13.9.$$

The measurements have been then used for two simulations: First we have used the approximated hologram as input for an alternating projection algorithm [98], here we have implemented Relaxed Averaged Alternating Reflections (RAAR) [73]. The iterates of RAAR for the wavefield Ψ under reconstruction are given by

$$\Psi_{n+1} = \frac{\beta_n}{2} (R_O(R_M(\Psi_n)) + \Psi_n) + (1 - \beta_n)P_M(\Psi_n), \quad (5.5)$$

where $R_{O/M}(\bullet) = 2\Pi_{O/M}(\bullet) - \bullet$ denotes a (mirror) reflection by a given constraint set and n the iteration index. Π_M and Π_O are defined as above in Eq. (??) and Eq. (??), respectively. The parameter β_n controls the relaxation. It follows the function

$$\beta_n = \exp\left(- (n/\beta_s)^3\right) \beta_0 + \left[1 - \exp\left(- (n/\beta_s)^3\right)\right] \beta_{\max}, \quad (5.6)$$

where β_0 denotes the starting value, β_{\max} the final value of β_n and β_s the iteration number when the relaxation is switched. This relaxation strategy follows [73] Eq. (37). The parameters have been set to $\beta_0 = 0.99$, $\beta_m = 0.75$, $\beta_s = 500$ for the reconstructions using RAAR.

Second have we used the two simulated holograms as input for d&u. We used the same constraints on O as described in Sec. 5.2. P is constrained by the magnitude projection and the separability. Additionally a smoothness constraint has been applied in Π_P . Amplitude and phase of P'_n are filtered with a Gaussian with FWHM of 1 px. Both algorithms were executed for 4000 iterations, starting from a amplitude 1, phase 0 initialization over the whole reconstruction area. Figure 5.6 summarizes the results.

By comparison of (a) and (b), the improved reconstruction quality of d&u is clearly evidenced. The background of (b) shows less distortions and small phase differences are reconstructed with better contrast, see for example the center region of the lower cell. The ringing artifacts at the edges of the object, which are observed in the standard flat-field correction scheme, disappear.

In addition to the object and in contrast to the standard scheme, d&u can recover P , at least to some extent, as shown in Fig. 5.6(c) and (d). The phases (c) show a good recovery of the edges compared to Fig. 5.4(b), but the low frequencies seem not recovered as well which is evidenced by the reduced contrast as compared to the original. Further, the amplitudes (d) are not as well recovered as the phases, some larger structures are recognizable as the cube left and the sitting angel on the right. Further below, we will discuss remedies which improve probe reconstruction,

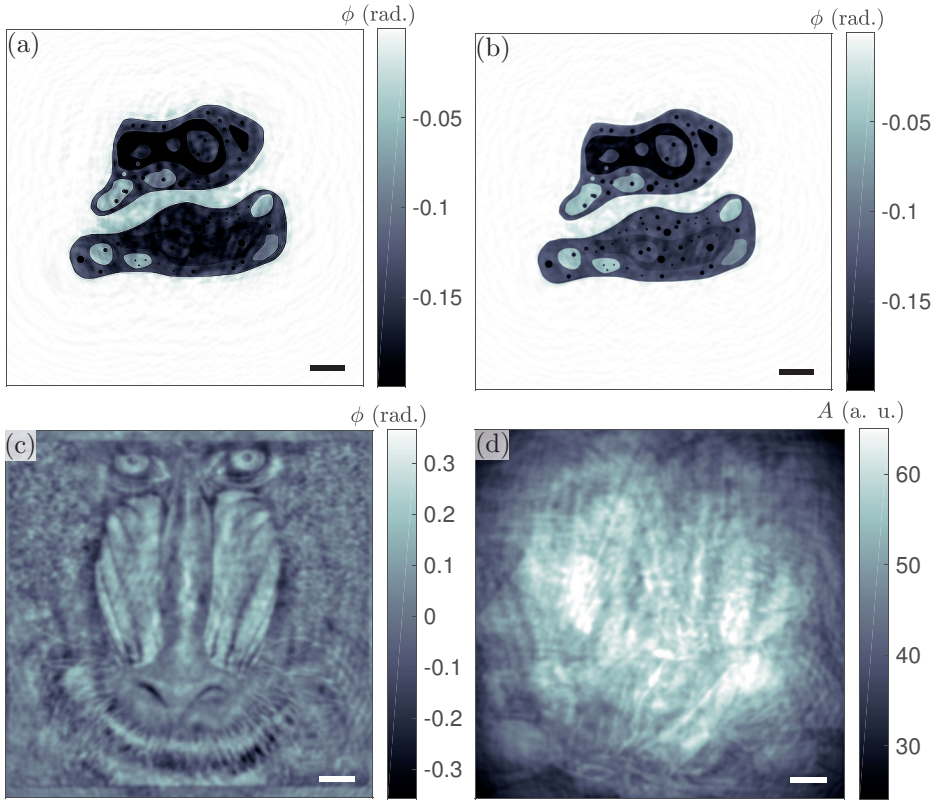


Figure 5.6.: Results obtained with divide&update for simulated noisy data with $\mu = 200$ ph/px after 4000 iterations. (a) The reconstructed object phases, obtained from conventional flat-field corrected data using RAAR. (b) The reconstructed object obtained from d&u. (c) Phases and (d) amplitudes of the reconstructed probe. The scale bar indicates 50 px.

by slightly changing the setting. Since only one measurement for P is used and no additional constraints on phase or amplitude, the reconstruction suffers from twin image artifacts and missing spatial frequency information. Figure 5.7 shows the results for the Fourier ring correlation (FRC)[97, 149] on the object reconstructions of Fig. 5.6(a) and (b) and the phantom Fig. 5.4(a). The flat field (blue) and d&u (red) reconstruction do not drop below the 1/2-bit threshold (yellow), this means both reconstructions have resolution down to the pixel level. The FRC yields more insight, it shows that the d&u reconstruction, while slightly lacking for frequencies in the range $[0.02, 0.15]$ 1/px, has a superior recovery of frequencies

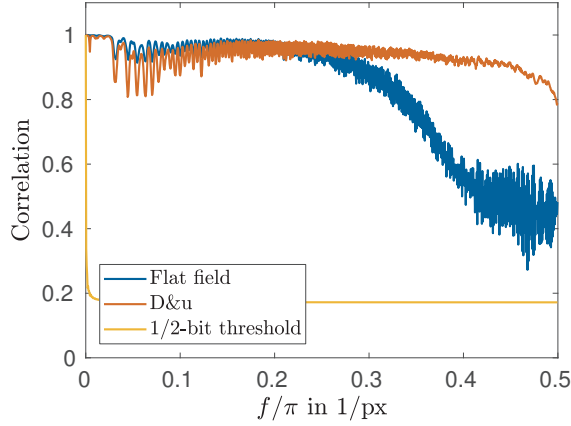


Figure 5.7.: Fourier ring correlation of the reconstructions of O shown in Fig. 5.6 with respect to the phantom Fig. 5.4(a).

beyond 0.25 1/px . The normalized Frobenius norm

$$\Delta = \frac{1}{N_x N_y} \left(\sum_{\forall \text{ pixels}} |\arg(\text{phantom}) - \arg(\text{reconstruction})|^2 \right)^{1/2} \quad (5.7)$$

is for the flat-field reconstruction $\Delta = 4.58 \cdot 10^{-5}$ and for d&u $\Delta = 2.45 \cdot 10^{-5}$.

5.3.2. Experimental data

In addition to the simulations, we present reconstructions obtained from experimental data, recorded at ESRF beamline ID16a using a photon energy of 17.05 keV, at instrumental settings described in [150]. The object consisted of spheres of different diameters 595 nm (SiO_2), 3 and 7 μm (polysterene). It was placed at a defocus distance of $z_1 = 13.79 \text{ mm}$. A FReLoN 2k ($N_x \times N_y = 2048 \times 2048 \text{ px}^2$) detector was used for recording the data with a pixel size of 845 nm, placed at a defocus distance of $z_2 = 435.56 \text{ mm}$. The exposure time was 1 s, 2 exposures have been acquired, one with and one without object in the beam. The exposures have been corrected for dark current, lens distortions and scintillator impurities. The images have been then normalized by their corresponding mean intensity value. The resulting normalized intensity distributions have been used as input for the reconstruction algorithms. Figure 5.2 shows the preprocessed input for (a) the measurement $|\mathcal{D}_{\text{Fr}}(\Psi)|^2$, (b) the measurement $|\mathcal{D}_{\text{Fr}}(P)|^2$ and (c) the flat-field correction

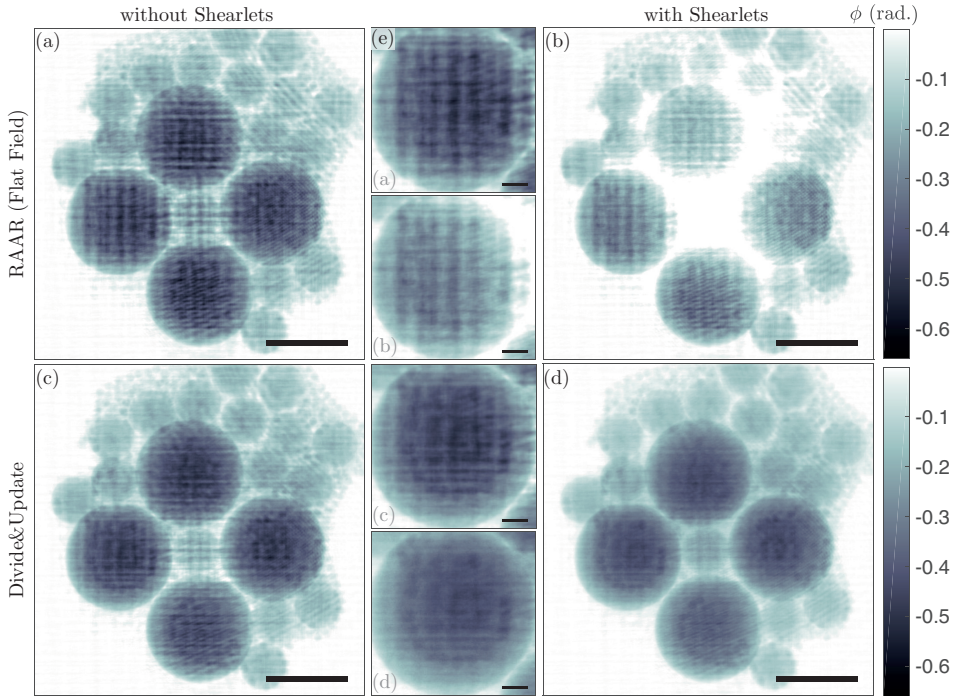


Figure 5.8.: Object phase reconstructions obtained by different reconstruction schemes applied to the same input data, shown in Fig. 5.2. (a) Reconstruction obtained by RAAR using the flat-field corrected input data after 20000 iterations. (b) same as (a) with shearlet suppression. (c) The d&u reconstruction shows significantly reduced artifacts. (d) same as (c) with shearlet suppression. All reconstructions shown are after 20000 iterations and the color bar applies to all panels. The scale bar indicates $5\ \mu\text{m}$ for (a) to (d). (e) Detail on the left large sphere for (a) to (d) from top to bottom, respectively. The scale bar indicates $1\ \mu\text{m}$.

obtained from (a) divided by (b). The effective object pixel size is $26.7\ \text{nm}$, given by the detector pixel size and the geometric magnification $M = z_2/z_1 \approx 31.5$. After transformation to a parallel beam (effective) geometry using the Fresnel scaling theorem, the (effective) Fresnel number is $\text{Fr} = 7.3 \cdot 10^{-4}$.

Figure 5.8 shows the reconstruction results after 20000 iterations for different reconstruction schemes applied on the same input data, as shown in Fig. 5.2. The reconstruction obtained by a standard iterative phase reconstruction algorithm scheme is shown in (a) and (b). As input the flat-field corrected single distance measurement was used, cf. Fig. 5.2(c). The reconstructions (c) and (d) obtained by d&u used the measurements shown in Fig. 5.2(a) and (b) as input. The phase

Table 5.1.: Summary of the parameters for the experiment.

Parameter	Value
Detector pixel size	845 nm
z_1	13.79 mm
z_2	435.56 mm
Magnification	31.5
Effective pixel size	26.7 nm
Fr	$7.3 \cdot 10^{-4}$
Iterations(simulation)	4000
Iterations(experiment)	20000

retrieval for Fig. 5.8(a) and (b) was carried out with RAAR, using the same set of constraints (pure phase shifting sample as well as the support constraints) as in the numerical experiment. This is to be compared with the reconstructions of O using d&u, shown in (c) and (d), which both exhibit improved reconstruction quality compared to (a) and (b), in particular an improved suppression of the P induced artifacts stemming from the KB aberrations. Also the resolution is improved, as judged from inspection of the smallest spheres, see also (e) for a zoom on the left of the large spheres. All reconstructions shown impose the same constraints on O , i.e. combined support and pure-phase constraint (cf. Eq. 5.3). In addition for (c) and (d) the physically correct formulation of the separation of complex valued wavefields instead of the flawed flat-field division [53, 54] is used. In the reconstruction of (b) and (d), an additional constraint in form of a shearlet suppression was applied in Π_S^O which for (d) further enhanced the reconstruction quality. For (b) the same set of shearlets has been suppressed as in (d) but with a negative effect on reconstruction quality. For this constraint, a shearlet decomposition [151–153] was used to identify components which appear both in P and the reconstructed O . These shared components are then removed from the object, as detailed in App. B. In (d) even the small spheres beneath the large sphere on the left become distinguishable. Still we note remaining structures which can be accounted to drift in P , i.e. inconsistency due to the fact that the object and empty beam recordings were not simultaneous, as proposed in the FEL illumination scheme sketched in Fig. 5.1. All reconstruction parameters are tabulated in Tab. 5.1.

The reconstructed phases and amplitudes of the probe are shown in Fig. 5.9 (a) and (b), respectively. The probe’s phase does not show a visible imprint of the object, contrary to the object where we observe remains of the probe. The amplitudes show no imprint, but we observe a decay of intensity towards the edge of the field of view, as we expect from a finitely extended illumination. Overall the separation

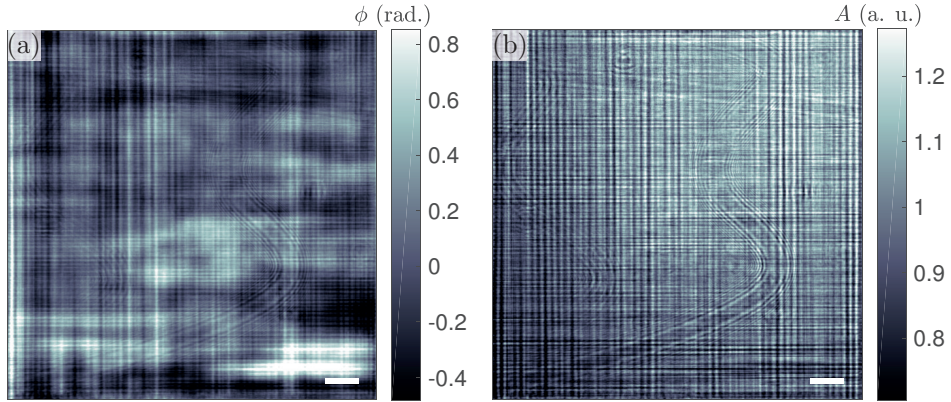


Figure 5.9.: Reconstructed probe P , obtained simultaneously with the object shown in Fig. 5.8(c). Phases and amplitudes are shown in (a) and (b), respectively. The scale bar indicates in all panels $5\ \mu\text{m}$.

of P and O works very well. The reconstruction was carried out as in the case for simulated data. However, a larger number of iterations is required, compared to simulated data. Inspection of the object reconstruction after 4000 iterations shows that the object has 'holes' which fill up with more iterations. Therefore a much higher number of iterations $n_{max} = 20000$ was used. The convergence rate can further be quantified by the error metric $\Delta_{\mathcal{X}}$ as a function of iteration n , as shown in Fig. 5.10. $\Delta_{\mathcal{X}}$ calculates the per pixel error of the reconstructed intensity $I_{\mathcal{X}}$ with respect to the measurements $M_{\mathcal{X}}$,

$$\Delta_{\mathcal{X}} = \sum_{\text{all pixels}} |I_{\mathcal{X}} - M_{\mathcal{X}}|^2 / N. \quad (5.8)$$

5.4. Discussion and outlook

Both simulation and experiment validate the proposed approach for simultaneous probe and object reconstruction in the optical near field, using a minimum of data, i.e. one recording with and one without the object (empty beam). In practice the two recordings can be acquired sequentially, as in the present experimental realisation, or simultaneously, if a second semi-transparent detector screen is used in front of the object, see Fig. 5.1. This is to be compared to established near-field ptychographic schemes, which are based on lateral [13, 154] and/or longi-

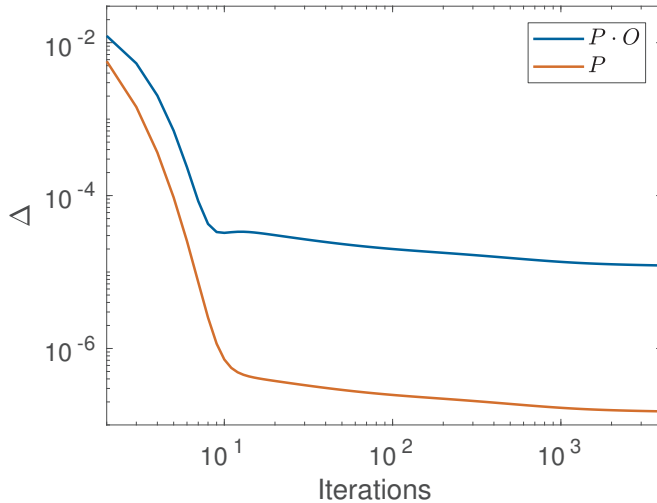


Figure 5.10.: Error measure Δ as function of the iteration number for the exit wave's Ψ (blue) and probes P (red) reconstructed intensity.

tudinal translations of the object [14, 76]. Hence, the standard approaches require sequential recordings and significantly more input data. In particular, they are neither compatible with time-dependent imaging nor with non-stationary illumination (probe). Unwanted probe fluctuations are particularly problematic in FEL imaging using stochastic SASE pulses, with considerable pulse-to-pulse fluctuations.

The price for relaxing the need of a stationary probe is a stronger set of constraints. Here we have used the constraints of a pure phase object and a support for the object and smoothness for the probe. Additionally we have employed a shearlet decomposition to identify and remove artifacts stemming from the probe. This is not a severe restriction for holography of biological (from cells to tissues) and soft matter samples at the nano scale, since total absorption is significantly reduced compared to macroscopic phase contrast imaging. For example the model protein $\text{H}_{50}\text{C}_{30}\text{N}_9\text{O}_{10}\text{S}$ [98, 155] has at an energy of 17.5 keV an attenuation coefficient of $1.38 \cdot 10^{-7} \text{ nm}^{-1}$.

Further, extended samples could possibly also be used in this scheme if the probe is fully captured by the detector, including the beam tails. Therefore, we anticipate that the presented scheme is ideally suited for single pulse full field FEL imaging even in the presence of strong pulse-to-pulse fluctuations. Using nano-focused illumination and high geometric magnification M as recently realized with SR [79],

sub-50 nm resolution and typical FOV in the range of several 10 micrometers are realistic.

Finally, we want to briefly address probe reconstruction. The results of the probe reconstruction shown in Fig. 5.6 (simulated data) is still quite flawed, in particular concerning the amplitudes. This can be avoided if the empty beam and the object recordings are carried out in two different planes, which is not the actual geometry realized in the present experiment at ID16a, but the geometry proposed in Fig. 5.1 for future FEL work. As shown by further simulation in App. A, recording P and Ψ in two different planes already stabilizes the reconstruction. We also stress that the Mandrill-Dürer probe is certainly an extreme case and could be replaced by an 'easier' setting with a smooth probe, for example a probe where more constraints can be applied from prior knowledge, e.g. from recording a data stream of typical probe fluctuations. A machine learning algorithm could then identify a lower dimensional space of 'allowable' probes. This issue is left for future investigation.

In summary, combination of common constraints with separability of P and O yields a minimalistic implementation of ptychography and a significant improvement in resolution, phase sensitivity and reduced probe artifacts as compared to reconstructions using flat-field corrected data. The divide and update scheme (d&u) presented here could also be extended to far-field imaging (coherent diffractive imaging) in a straightforward way. Finally, we want to point out the advantages of d&u also for the case of imaging with stationary probes. Conventional probe and object retrieval by multi-plane detection or multi-object translations requires substantial recording time. Contrarily, single distance recordings are preferred in particular for tomographic scans. The present scheme reconciles such single distance recordings with proper treatment of an aberrated (non-ideal) probe.

5.5. Appendix A: Simulation for parallel data acquisition scheme

The proposed setup for parallel data acquisition Fig. 5.1 has been validated by simulation. The reference plane for P has been set at $\text{Fr} = -1 \cdot 10^{-3}$ in front of the plane of O . This way we can simulate effects of a propagated probe at the object plane. Starting from the plane of O we have simulated measurements of Ψ for $\text{Fr}_\Psi = 1 \cdot 10^{-3}$ and P for $\text{Fr}_P = -5 \cdot 10^{-3}$ (in front of O). Poissonian noise corresponding to 2000 ph/px has been added to the measurements. Figure 5.11 shows the reconstructions of O (a) and P (b,c) after 4000 iterations of d&u without

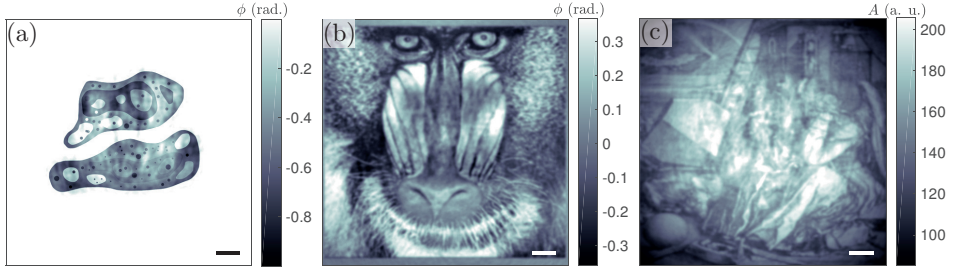


Figure 5.11.: Reconstructions for parallel acquisition setup. Structure as in Fig. 5.4. (a) Phases of the reconstructed object. (b, c) reconstructed probe in phase and amplitude, respectively, in the probe's reference plane located at $Fr = 1 \cdot 10^{-3}$ in front of the object. The scale bar indicates 50 px.

shearlet constraint. Inspecting the reconstructions shows, that the amplitudes of P (c) are recovered much better than in Fig. 5.6. The second measurement distance for P breaks the twin image symmetries (complex conjugates) and eliminates these artifacts. The remaining artifacts in P stem from the incomplete separation of O . Note, a smaller Fr_P yields a better reconstruction of P . The reconstruction of O is spoiled by some low frequency artifacts as compared to Fig. 5.6. Using shearlets to identify unseparated contributions in O can improve the reconstruction.

5.6. Appendix B: Details of the shearlet suppression

For enhancing the reconstruction a shearlet suppression has been applied in each iteration step. The shearlet transformation has been calculated using ShearLab 3D v1.1 [151, 156]. A shearlet system with 4 scales and $\{1, 1, 2, 2\}$ shears per respective scale. This results in a system redundancy of 49 shearlets. Starting with the reconstruction of O shown in Fig. 5.8(b) and P in Fig. 5.9, the phases of these wavefields have been decomposed in the shearlet basis. In order to find the shearlets with the largest contribution, the shearlets intensity, i.e. the sum of the shearlet's coefficients as function of the shearlet index is shown in Fig. 5.12(left). The blue and red curve show the shearlet's intensities for O and P (left), respectively. These curves have basically the same, but shifted functional form. The shift results from the fact, that we have assumed for $|O(x, y)| = 1$, while P is allowed to have spatially varying intensity values ≥ 1 . The sensitivity of the shearlets to structures in the reconstruction is exemplarily shown on the right. To exemplify

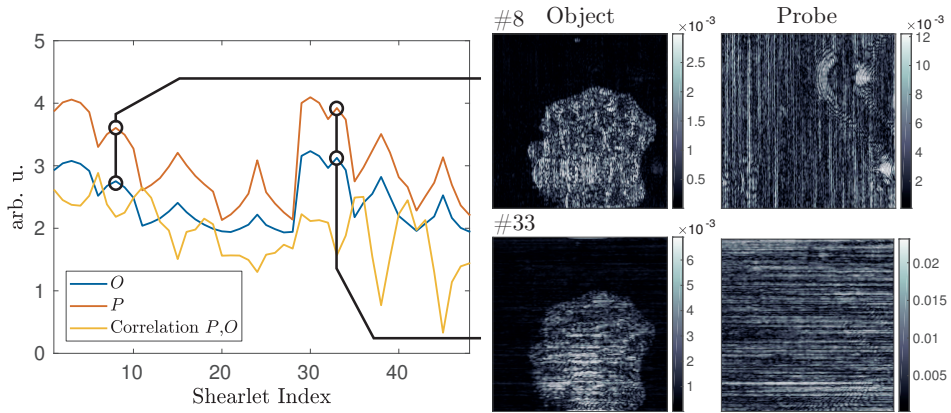


Figure 5.12.: Shearlet analysis of O and P . (left) The red and blue curve show the intensity of the shearlets as function of the shearlet's index. The yellow curve shows the correlation of the respective shearlet coefficients for P and O . (right) The coefficient matrices of O and P for the shearlets with index #8 and #33.

this, shearlets with large contribution for vertical and horizontal structures are shown, respectively #8 and #33. To gain further inside we have calculated the correlation of O and P for each shearlet coefficient. This has been achieved by using the MATLAB function `norm2xcorr`. The yellow curve shows the correlation of the P and O shearlets, for zero-shift. Certain shearlets show only a weak correlation and visual inspection shows indeed that these are the shearlets describing the horizontal and vertical stripes on different scales in the reconstruction. The first approach, to threshold all shearlets below a certain correlation value yields only poor image quality, since some of the removed shearlets carry important resolution information, e.g. # {29, 34, 39}. After visual inspection, the shearlets S_{VI} with indices # {3, 8, 15, 30, 31, 33, 38} have been suppressed, which has yielded the best reconstruction shown in Fig. 5.8(c). The suppression has been carried out by multiplying the whole coefficient matrix corresponding to a shearlet by a factor θ , in this case $\theta = 0.8$. The shearlet suppression was applied in each iteration of the reconstruction run for the result shown in Fig. 5.8(c), providing additional constraint as part of Π_G^O . Contrarily, Figure 5.13 illustrates the effect of (a) applying the shearlet suppression as mere post-processing image filter compared to (b) incorporating the suppression in the algorithm. This shows that the additional computational effort yields an improved reconstruction.

This scheme is a first approach to incorporate the shearlet decomposition in phase retrieval to enhance separability of P and O it can be further extended: The

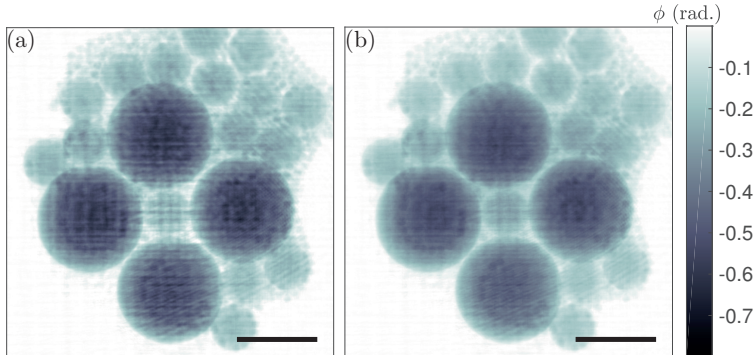


Figure 5.13.: Effect of shearlet suppression. (a) shows the effect of the shearlet suppression applied on the object's reconstruction shown in Fig. 5.8(b). (b) the same as Fig. 5.8(c), where the shearlet suppression has been applied as part of Π_S^O in each iteration. The scale bar indicates in all panels 5 μm .

shearlet components extracted from O can be 'transplanted' in the corresponding coefficients of P . The suppression parameter θ can be relaxed, in order to boost artifact removal at the beginning of the reconstruction and later to find a stable solution. Multiplying the complete coefficient matrix with θ is rather harsh, since the shearlets give highly localized information, one could look for areas in the image, where the variation is strong and apply there locally the suppression. Finally we want to note, that the separation of P and O shows similarities to image separation problems[151, 157].

Funding

Deutsche Forschungsgemeinschaft (DFG) (SFB 755); Bundesministerium für Bildung und Forschung (BMBF) (05K16MGB).

Acknowledgments

We thank Mareike Töpferwien and Peter Cloetens for invaluable help during the beam time. We thank Aike Ruhlandt and Jan-David Nicolas for fruitful discussions. We thank Jan Goeman for keeping the number crunching machines up and running.

6. Summary and Outlook

This thesis has presented new schemes to account for imperfections encountered in x-ray near-field holography experiments. Chapter 2 presented the reconstruction of the probe of a state of the art x-ray nano focus setup under the assumption of full coherence. The probe reconstruction has been carried out in the diverging geometry i.e. no Fresnel scaling was applied. This is a numerical demanding approach but it yields a more direct access to the relevant aspects of propagation and focusing of the probe. The next step towards a full model of the probe is the inclusion of the effects of partially coherent illumination as described in Chapter 4. The partial coherence has been modeled in terms of an ensemble of mutually incoherent modes. To this end, the scheme by Thibault [99] has been extended to near-field imaging. In numerical experiments the reconstruction of the coherent modes with their accompanying occupation numbers has been demonstrated. Further, the algorithm's robustness was tested against different parameter choices. Also, the extraction of the coherence length has been shown. Related to this topic, the requirements on coherence for near- and far-field imaging have been surveyed in Appendix A. The results support the claim that near-field imaging is less sensitive to partially coherent illumination than far-field imaging.

Chapter 3 has presented a contribution to the vast, but extremely important, fluence-resolution discussion for different imaging modalities with x-rays or other kind of probes. Despite the considerable number of available publications concerning the dose and resolution in x-ray imaging and electron microscopy, this issue has not been fully answered, yet. In the chapter near- and far-field propagation-based imaging are compared in a numerical study. The results show a superior performance of near-field imaging. These numerical results are substantiated by experimental results, but only in a snap shot manner. A systematic study has still to be carried out. While the near field reconstruction is quite tolerant against noise, the reconstructions can still benefit from denoising techniques applied to the measurements or during the reconstruction process. Previous work using classical denoising strategies [158] and work based on rather new developments in statistical multiresolution estimation [159] showed the possible improvements for holography. Chapter 5 has described a novel ptychographic algorithm termed divide&update

using a minimalistic set of measurement. The feasibility has been demonstrated in simulations and on experimental data obtained at ESRF beamline ID16a. The obtained high quality reconstructions have shown the capabilities of the smoothness and shearlet constraint for phase retrieval. The possibilities offered by shearlets for artifact removal and efficient description of a wave field (be it object or probe) in terms of a sparse base should be further investigated and exploited in future work. Divide&update offers opportunities to implement imaging with non stationary probe or objects as they occur at x-ray free electron lasers. In order to acquire in parallel the measurements a second semi-transparent detector is necessary. First experiments, implementing a dual detector system have been performed at the GINIX-setup at DESY beamline P10. Nevertheless, divide&update offers also advantages for imaging with stationary probes, since data recording times are reduced and the aberrated probe is correctly taken into account.

With the advent of 4th-generation synchrotron sources, the available flux for imaging will be drastically increased. The dream to scan cubic millimeter sized specimen at 10 nm resolution may become reality. Not speaking about the enormous amounts of data, the dose on the specimen is tremendous. Also the question of specimen stability arises at long scanning times. With the possibility to acquire full field images with near-field holography, the radiation exposure can be minimized and scanning time can be reduced. Thus, with the enhanced reconstruction techniques presented here, near-field holography is ideally suited for these new x-ray sources.

Appendix

A. How much Coherence is Needed for Near-Field Imaging?

The ability of a x-ray wave field to interfere with itself and an object is a prerequisite for many x-ray measurement techniques. This is for example the case, not only for propagation-based imaging techniques as discussed in Chapter 4 but as well as for coherent spectroscopic techniques such as x-ray photon correlation spectroscopy (XPCS).

While Chapter 4 was concerned with the recovery of an ensemble of coherent modes to describe the coherence properties of the probe P , the question under survey here is: "Which degree of coherence is required for different imaging techniques?"

Despite the possibility at hand to reconstruct the modal structure of a partially coherent probe with mmMMP in the near-field or Thibault's approach for the far-field, it might still not be possible to acquire the necessary data set for the reconstruction due to temporal instabilities in P or O . Thus, similar as in Chapter 3, it is insightful to survey the robustness of different imaging techniques against partial coherent illumination. The techniques studied are near-field holography (NFH) and coherent diffractive imaging (CDI) in the optical far-field. The robustness is quantified in terms of resolution and reconstruction error with respect to a phantom, as a function of transversal coherence length ξ .

A.1. Coherence model

To study of the effects of a reduced spatial degree of coherence, i.e. $0 < \|j(d)\| < 1$, in NFH and CDI we make use of the model of a completely incoherent but

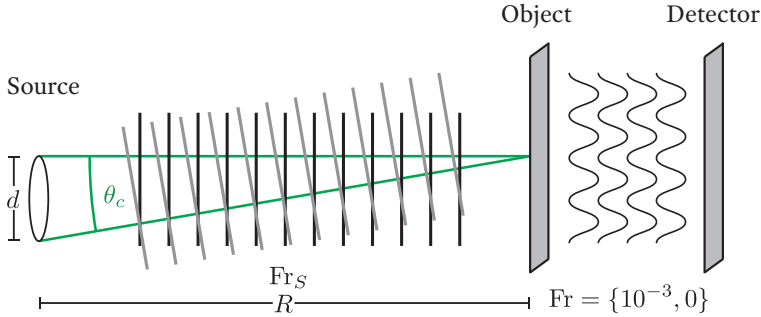


Figure A.1.: Sketch of the used coherence model. Plane waves are emitted by an incoherent source with extension d . An object is placed at distance R behind the source. The plane waves impinge on the object from a cone with opening angle θ_c . The object is given as a phantom image, cf. Fig. A.2. We assume that the projection approximation holds. The partial coherent measurements are simulated at a detector for the two cases of NFH and CDI.

monochromatic source. In a completely incoherent source all points in the source emit uncorrelated radiation.

Figure A.1 shows the principal sketch for the coherence model in use. The model considered is based on ergodic realizations and incoherent superpositions [123] of plane waves emitted by the source S with extent d . The object O is placed in a distance R behind the source. θ_c is the angle subtended by the source at O , we assume θ_c to be small so that the paraxial assumption holds. The plane waves emitted by S impinge on O at a maximum angle of θ_c . The coherence length ξ is then given by

$$\xi = \frac{\lambda R}{2d} = \frac{\lambda}{2\theta_c}, \quad (\text{A.1})$$

i.e. the length when two waves intersecting with θ_c have a phase shift of π . Thus θ_c can be expressed as

$$\theta_c = \frac{\lambda}{2\xi}. \quad (\text{A.2})$$

The momentum transfer of a wave impinging on O under angle $\alpha \in \{-\theta_c/2, \theta_c/2\}$ is

$$q(\alpha) = \frac{2\pi}{\lambda} \sin(\alpha), \quad (\text{A.3})$$

with the wavelength λ . Writing $\alpha = \zeta\theta_c/2$, $\zeta \in \{-1, 1\}$, inserting θ_c and assuming small angles $\alpha \approx 0$ yields

$$q = \frac{\pi\zeta}{2\xi}. \quad (\text{A.4})$$

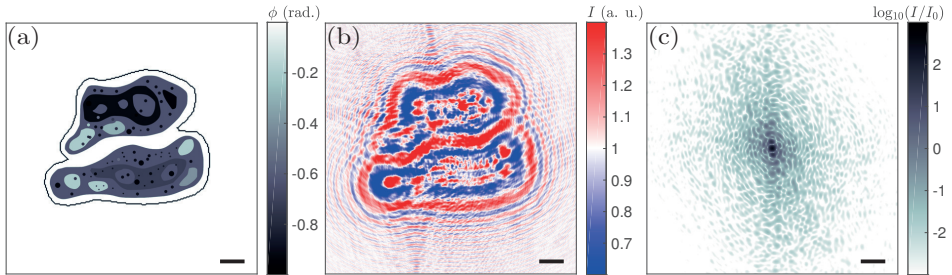


Figure A.2.: Setup for the simulation: limit of full coherence. The pure phase phantom (a) of a cell with maximum phase shift of -1 rad. The black line indicates the support used in the reconstruction. The ideal near-field hologram (b) at $Fr = 10^{-3}$ of (a). The ideal far-field measurement (c) of (a). The scalebar indicates 50 px. Examples of partially coherent measurements are presented in Fig. A.3.

The momentum transfer is independent of λ , this allows us to simulate the model in a dimensionless setting with ξ , given in units of pixels, as the only control parameter. Note, that the numerical implementation recurses to the use of α to choose the realizations of incident plane waves.

A.2. Numerical simulation

Figure A.2 introduces the concept of the numerical study. The setup presented here follows closely the setup of Chapter 3. As in Chapter 3 we use the phantom of two adhering cells (a). It is a pure phase-contrast object with phases $\phi_{x,y} \in \{0, -1\}$ rad. The phantom has a size of $L = 512 \times 512$ pixel² embedded in 1024×1024 ($N_x \times N_y$) pixel². From that we generate the ideal measurements for NFH (b) at a Fresnel number $Fr = 10^{-3}$ and CDI (c) at $Fr = 0$. To ensure artifact-free propagation a padded size of 2048×2048 pixel² has been used. Note, all lengths are measured in the size of pixels, thus the pixel size Δx is 1.

For the incoherent source model, especially for small ξ , a large number of realizations for the plane waves N_R is necessary. The measurements shown in the following have been obtained by the superposition of $N_R = 5000$ realizations of the source. Experimentation has shown, that small coherence lengths need this large number for N_R so that the partially coherent measurement properly converges. For simplicity this value has been used as well for the large coherence lengths.

Each realization of the exit wave Ψ_α is calculated by

$$\Psi_\alpha = P_\alpha \cdot O, \quad (\text{A.5})$$

where P_α is a canted plane wave emitted by S at angle α . α can also be read as the wave vector of the plane wave, interacting with the object O . Then by using the respective propagator \mathcal{X} , being either the Fresnel propagator \mathcal{D}_{Fr} Eq. (3.4) or the Fourier transformation \mathcal{F} , the partial coherent measurement M is simulated by

$$M = \sum_{n_R=1}^{N_R} \|\mathcal{X}(\Psi_\alpha)\|^2. \quad (\text{A.6})$$

Since a two dimensional extended source is considered, the plane waves are emitted in a cone (as seen from O), thus the incidence angles have to be uniformly distributed on a circle with “radius” $\theta_c/2$. The uniform distribution is generated in polar coordinates and then transformed in Cartesian coordinates:

1. Generate 2 uniform distributed random numbers $n_1, n_2 \in [0, 1]$.
2. Calculate the polar angle $\vartheta = 2\pi n_1$ and radius $\rho = \frac{\theta_c}{2} \sqrt{n_2}$. The root is for normalization on the circle surface.
3. Transform in Cartesian coordinates $\alpha_x = \rho \cos(\vartheta)$ and $\alpha_y = \rho \sin(\vartheta)$.

With that the canted plane wave P_α is

$$P_\alpha = \exp(i(\alpha_x \cdot r_x + \alpha_y \cdot r_y)), \quad (\text{A.7})$$

where $r_{x,y}$ denote coordinates in the plane of O .

While this is the intuitive way to simulate M , it has two drawbacks: (i) it is numerical extremely costly and (ii) for CDI the multiplication with P_α leads to numerous numerical artifacts in $\mathcal{F}(P_\alpha \cdot O)$. In order to remove these artifacts it is necessary to precisely choose padding and windowing functions.

A more practical approach can be obtained by analyzing the properties of the propagators. It shows that multiplication with P_α leads to a shift of the individual realization of the measurement. For the far field α translates to a shift of the ideal measurement by

$$\Delta s_{FF} = \alpha_{x,y} \cdot N_{x,y} \text{ (pixels)}. \quad (\text{A.8})$$

This is basically the interpretation of the incident wave vector in the discrete Fourier space sampling of the detector. The near field is affected in the same way but the finite propagation distance z has to be taken into account. Starting for

Algorithm 2 Generation of of partial coherent measurements using sub-pixel shifts

- 1: Calculate Δs_{\max} with $\alpha = \theta_c/2$
 - 2: $M_{id} \leftarrow \mathcal{X}(O)$ ▷ generate ideal M
 - 3: $M \leftarrow 0_{(N_x + \Delta s_{\max}) \times (N_y + \Delta s_{\max})}$ ▷ start with 0 for M
 - 4: ▷ Loop over realizations
 - 5: **for** $n = 1 \dots N_R$ **do**
 - 6: Generate $\alpha_{x,y}$, as described above
 - 7: Calculate $\Delta s(\alpha_{x,y})$
 - 8: $M_{\Delta s} \leftarrow \text{shift}(M_{id}, \Delta s)$
 - 9: $M \leftarrow M + 1/N_R \cdot M_{\Delta s}$ ▷ Add up and normalize
 - 10: **end for**
 - 11: Cut out M to fit $N_x \times N_y$
-

the near field shift Δs_{NF} with $\Delta s_{NF} = q \cdot z$ and using the definitions for q and Fr leads to

$$\Delta s_{NF} = \alpha_{x,y} \cdot \frac{1}{\text{Fr}} \text{ (pixels)}. \quad (\text{A.9})$$

Using these shifts, the simulation of M can be efficiently implemented using sub-pixel shifting operations, as detailed in Alg. 2. Some examples for the measurements with varied ξ can be found in Fig. A.3 (a,c).

Note, the simulation of M can also be carried out in form of a convolution with the Fourier transformation of the source profile (cf. Van Zittert-Zernike-theorem [123]), which can be interpreted as a coherence envelope. This is an approach often used in high resolution electron microscopy [160]. Still the variant presented here is more instructive and more of a bottom-up approach to describe the observed effects.

After simulation of M , the phase reconstruction process has to be carried out. As in Chapter 3 RAAR is used as reconstruction algorithm, cf. Eq. (3.5), with relaxation parameters $\beta_0 = 0.99, \beta_{\max} = 0.75, \beta_s = 75$ and 200 iterations. Also the same set of constraints is used, cf. Eq. (3.8). Note, the phase reconstruction is carried out under the assumption of full coherence, this introduces an inconsistency in the constraints. Recently, a method for CDI has been proposed [161] to recover the object and coherence properties of the illumination from a single measurement. The resolution of the obtained reconstruction is assessed via Fourier ring correlation [97, 149] (FRC) to the phantom.

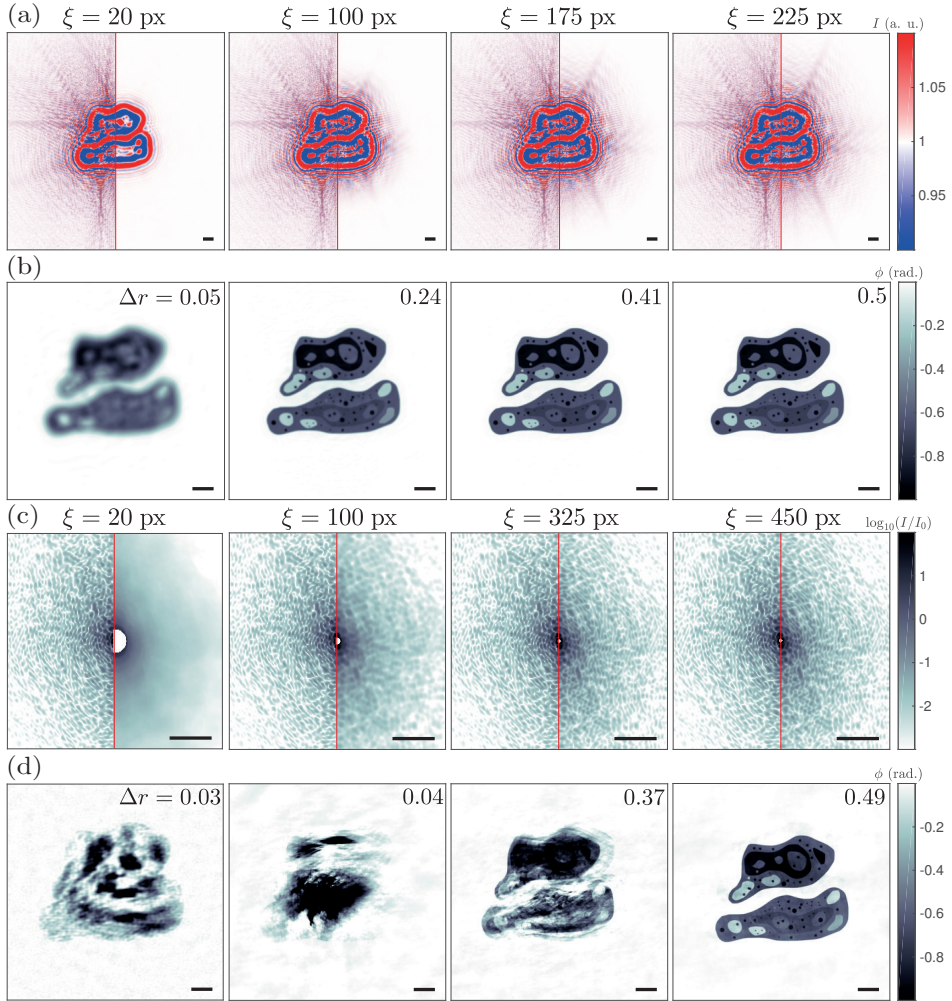


Figure A.3.: Example reconstructions for varied coherence length ξ . The measurements for NFH (a) and CDI (c) show for each panel in the left half the fully coherent measurement and in the right half the measurement obtained for the ξ given in the title. The partially coherent CDI measurements have a virtual beam stop covering the zeroth order. The NFH measurement is shown on linear scale and the CDI measurement on logarithmic scale. The reconstructed objects for NFH (b) and CDI (d). The number in the upper right corner of each panel denotes the resolution Δr in $1/\text{px}$. The scalebar indicates 50 px in all panels.

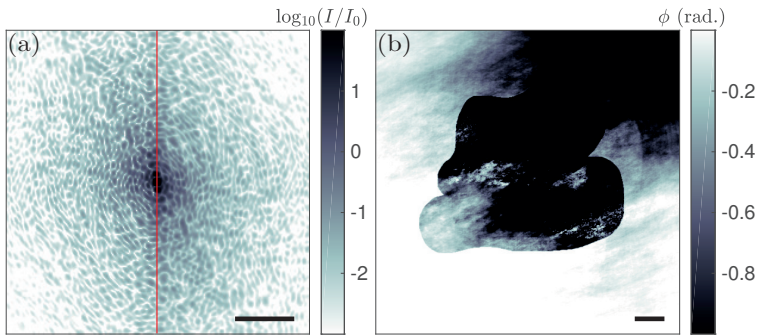


Figure A.4.: CDI reconstruction without the virtual beam stop. The simulated measurement for $\xi = 500$ px (a) and the corresponding reconstructed object's phases (b).

A.3. Results

First the influence of $\xi < \infty$ on the measurement M is surveyed in Fig. A.3. The M for varied ξ are shown in (a) for NFH and (c) for CDI, note the different choice of ξ for NFH and CDI. The left half of the measurement panels shows the ideal fully coherent M , while the right half shows M for the ξ given in the title with $N_R = 5000$. The NFH measurements are shown on linear scale in a diverging cool-warm colormap [162], which illustrates the oscillation of fringes. By increasing ξ , the fringes spread out wider and sub-structure in the fringes becomes visible. The recovered objects (b) used the respective measurement from (a). The increase in ξ is accompanied by an increase in resolution Δr , given in the upper right corner of the reconstruction panels. At $\xi = 225$ px, for comparison, the object has an horizontal extension of 306 px, NFH reaches full resolution and the recovered object exhibits no visible deviations from the phantom. Interestingly, the corresponding hologram shows more deviations to the ideal hologram.

The CDI measurements are depicted on a logarithmic scale. For small ξ they show a strong smearing. With increased ξ the speckles become sharper, but the fine lines between the speckles do not become zero as in the ideal measurement. The corresponding reconstructions (d), do not show the same blur as in NFH, but rather a total reconstruction failure for $\xi = 20$ px and 100 px. The reconstruction for $\xi = 325$ px still shows low frequency and stripe artifacts but the smallest features are quite clearly visible. For $\xi = 450$ px the reconstruction has nearly reached full resolution and is close to artifact free. The reader probably has noticed the

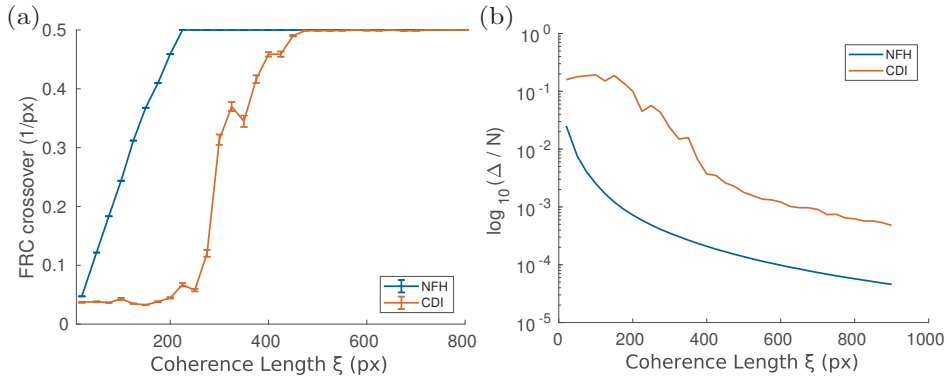


Figure A.5.: Results as a function of the coherence length ξ . The ξ -resolution result for NFH and CDI (a) for typical experimental parameters. ξ has been varied from 20 to 900 px, each ξ had 20 realizations with each 5000 realizations of the source to generate the measurement. The ℓ^2 error (Eq. (3.9)) of the reconstruction (b) with respect to the original phantom.

white circles in (c). These are virtual beam stops to block the zeroth order in the diffraction patterns and to exclude these values during the reconstruction process. The beam stops' radii have been chosen as $2 \cdot \Delta_{s_{\max}}$, with $\Delta_{s_{\max}}$ the maximum shift of the measurement for a given θ_c . This value seems prohibitively high but ensures stable reconstructions without introducing noticeable reconstruction artifacts. Figure A.4 shows a measurement (a) for $\xi = 500$ px without beam stop and the reconstructed phases (b) obtained from (a). The high coherence length results in a $\Delta_{s_{\max}} = 0.5$ px. Despite this low value, the reconstruction fails without beam stop. The artifacts encountered are not just low frequency deviations, also the inner structure is not recovered, only the support shows a strong imprint in the reconstruction.

Next, we turn to the coherence-resolution relationships which are computed by performing the automatized reconstruction and FRC analysis for measurements of systematically varied coherence length ξ . For each ξ covering the range from 20 to 900 px, 20 realizations have been generated and reconstructed, each with the same parameters. Figure A.5 shows the results. The ξ -resolution curve (a) shows two different behaviors, for NFH the resolution increases linearly until it reaches full resolution at $\xi = 225$ px. For CDI the resolution does not improve over the range of $\xi = 20$ px to 250 px, then we notice a steep increase in resolution which saturates at $\xi = 475$ px. The error plot (b) shows Δ , as defined by Eq. (3.9). For NFH we see up to $\xi = 225$ a steep decrease and afterwards a slower reduction in

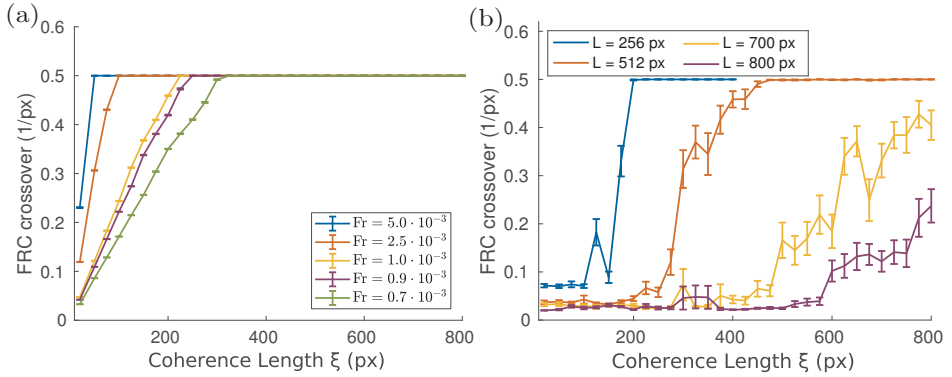


Figure A.6.: ξ -resolution results as function of the setup parameters Fr and L for (a) NFH and (b) CDI, respectively. The NFH result (a) for varied Fresnel number Fr . A smaller Fr needs a larger ξ for a high resolution reconstruction. The CDI result (b) for varied size L of the object under survey. The objects with larger size L need a higher degree of coherence in the illumination for a high resolution reconstruction. In both settings $N_R = 5000$ and 20 realizations per ξ have been used.

Δ . The CDI curve shows again at larger ξ a steep decrease, but overall the error is roughly an order of magnitude larger than it is the case for NFH.

The results shown so far have been obtained at fixed simulation parameters, notably Fr and object size L . The change of these parameters has different effects on NFH and CDI as the results in Fig. A.6 show. The algorithm and realization parameters are set as before. (a) shows the effect of changing Fr on the NFH result. The plot shows variation of Fr from $0.7 \cdot 10^{-3}$ to $5 \cdot 10^{-3}$. Smaller Fr need a larger ξ to be properly reconstructed. This can be explained by the fact, that at smaller Fr , the fringes of the hologram are propagated further out. Consider two features in the object that have a large separation distance. In the small Fr case the fringes emanated from these features come in contact. The fringes have to interfere coherently in order to form the correct hologram. This requires a larger ξ .

(b) shows the effect of changing the object size L on the CDI result. The plot shows the ξ -resolution curves for varied $L = \{256, 512, 700, 800\}$ px. This corresponds to object extensions of $\{153, 306, 418, 478\}$ px. The plot supports the standard recommendation for CDI to use „compact and isolated“ objects. Small objects need significantly less coherence to reconstruct than larger objects. Also the demands on the coherence seem to scale worse for larger objects.

The obvious next step is to study the influence of noise on the partially coherent

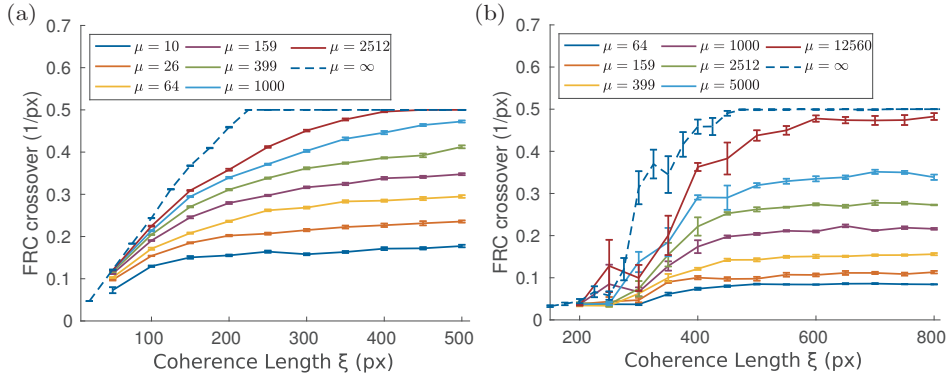


Figure A.7.: Resolution as function of ξ at varied fluence μ (photons per pixel). (a) results for NFH and (b) for CDI. Note, (a) and (b) show not exactly the same choice of μ also the sampling of ξ 's has been adapted to the respective method. The dashed lines indicate the noise free result from Fig. A.5(a).

measurements. The findings of this experiment are shown in Fig. A.7. The results have been obtained as for Fig. A.5(a), i.e. $Fr = 1 \cdot 10^{-3}$ and $L = 512$. Due to the larger numerical cost, added further by the variation of the fluence μ (photons per pixel), the realizations per measurement were reduced to $N_R = 3000$ and each ξ has been repeated just 10 times for averaging. The noise has been added after the simulation of the partial coherent measurement, following the recipe described in Chapter 3.2. Both NFH (a) and CDI (b) show stagnation of the resolution below 0.5 1/px if μ is too small, e.g. up to $\mu = 399 \text{ ph./px}$ for NFH and $\mu = 5000 \text{ ph./px}$ for CDI. For NFH we observe the interesting case $\mu = 2512 \text{ ph./px}$ where the increase in ξ increases the contrast in the measurement so that the fringes have sufficient contrast, yielding full resolution for the reconstructed object. As for the pure fluence resolution survey we note roughly 5 times higher requirements on the fluence for CDI then for NFH, before the reconstruction reaches full resolution.

A.4. Summary

The survey of the coherence requirements for near- and far-field propagation-based x-ray imaging, NFH and CDI respectively, shows a different behavior for these two optical regimes. NFH shows for a given Fr a linear behavior in the increase of resolution. With smaller Fr the increase in resolution is still linear but the full resolution is reached at larger ξ . For sufficiently small samples, CDI can reach the

full resolution earlier than NFH. Larger samples show an unfavorable scaling behavior for ξ and could be thus easier imaged under relaxed coherence requirements with NFH.

Taking also noisy measurements into account shows again the robustness of NFH compared to CDI. These results are also in line with the recent success of phase-contrast tomography [163–165] at laboratory setups.

B. Iterative Reconstruction Algorithms

In the following, different approaches to iterative phase retrieval are compared. The algorithm's performance are compared on noisy measurements of given fluence μ . Chapter 3 has surveyed the influence on the resolution on the reconstruction. The noise added to the measurements is clearly a form of inconsistency between the sought object, physical constraints and measurements. Phase retrieval is an example of a feasibility problem, where multiple constraints shall be satisfied at the same time. The set of solutions for this problem can be empty. The algorithm should find then the best approximation point in the configuration space to fit the constraints.

The algorithms under consideration are:

- algorithm of alternating projections (AP) [125]
- hybrid input output algorithm (HIO) [166]
- relaxed averaged alternating reflections (RAAR) [73]
- Wirtinger-flow (WF) [167]

AP/HIO and RAAR belong to the type of projection algorithms. These algorithms make use of consecutive projections P on the constraint sets S (specimen, sample, support) and M (measurement). AP is then written as

$$\Psi_{n+1} = P_S(P_M(\Psi_n)). \quad (\text{B.1})$$

HIO with support S and negativity constraint on the phases [98] is given by

$$\Psi_{n+1} = \begin{cases} \min(P_{\widehat{M}}(\Psi_n(x)), 0) & \text{if } x \in S \\ \Psi_n(x) - \beta(P_{\widehat{M}(\Psi_n(x))}) & \text{else} \end{cases}, \quad (\text{B.2})$$

with constant $\beta \in [0, 1]$. Additionally the implementation from [98] uses a „soft projection” on the measured intensities, this takes the distortion of noise into account. The intensities M are modified to yield \widehat{M}

$$\widehat{M} = \left(1 - \frac{D}{\Delta}\right) M + \frac{D}{\Delta} |\Psi_n|^2, \quad (\text{B.3})$$

where D is a discrepancy parameter and Δ the normalized ℓ^2 error of reconstructed to measured intensity

$$\Delta = \left(\frac{1}{N} \sum_{\forall \text{pixels}} \left[M - |\Psi_n|^2 \right] \right)^{1/2}. \quad (\text{B.4})$$

The algorithm is iterated as long $\Delta > D$ is true. The optimal choice of D is $D_{id} = (2/\mu)^{1/2}$ [98], but due to stagnation or too early abortion D should be chosen smaller than D_{id} [168]. This extension of HIO seems somehow artificial, but experimentation has shown that it is necessary. Figure B.4 (c) shows a reconstruction obtained with the standard magnitude projector which AP and RAAR use. This standard HIO (sHIO) shows artifacts in form of rings and low frequency distortions, the resolution is only $\Delta r = 0.267$ 1/px.

The RAAR iteration is repeated (cf. Eqs. 2.1, 3.5, 4.6, 5.5) here for completeness

$$\Psi_{n+1} = \frac{\beta_n}{2} (R_S(R_M(\Psi_n)) + \Psi_n) + (1 - \beta_n)P_M(\Psi_n), \quad (\text{B.5})$$

where $R_{S/M}(\bullet) = 2P_{S/M}(\bullet) - \bullet$ denotes a (mirror) reflection by a given constraint set. The parameter β_n controls the relaxation. It follows the function

$$\beta_n = \exp\left(- (n/\beta_s)^3\right) \beta_0 + \left[1 - \exp\left(- (n/\beta_s)^3\right)\right] \beta_{\max}, \quad (\text{B.6})$$

where $\beta_0 \leq 1$ denotes the starting value, β_{\max} the final value of β_n and β_s the iteration number when the relaxation is switched. The choice of β_s influences the convergence speed and β_{\max} changes the fix point to which RAAR converges, for example $\beta_{\max} = 0.5$ has the same fix points as AP. This is demonstrated in the following. Figure B.1 depicts the calculation of a new RAAR iterate with a geometrical interpretation of the intermediate steps. It also geometrically illustrates the construction of a reflector, in particular $R_M(\Psi_n)$. We see by the use of reflectors the space of possible configurations is better explored.

HIO is given in algorithmic notation and RAAR/AP in fix point notation, cf. [73, 169, 170]. Note, that the algorithmic form depends on the constraints in use.

WF is a gradient scheme, which employs coded measurements Y with $l = [1, L]$ random phase masks M_l or more general sampling vectors, which are known,

$$Y = \forall l : |\mathcal{D}_{\text{Fr}}(M_l^* \odot \Psi)|^2, \quad (\text{B.7})$$

where $*$ is the complex conjugate and \odot denotes the point-wise product. It does

A is the forward operator

$$A(\Psi) = \forall l : \mathcal{D}_{\text{Fr}}(M_l^* \odot \Psi) , \quad (\text{B.11})$$

the result is a 3d tensor of size $N_x \times N_y \times L$. A^t is the backward operator, operating on the tensor quantity

$$A^t(\bullet) = \sum_{l=1}^L M_l \odot \mathcal{D}_{-\text{Fr}}(\bullet) , \quad (\text{B.12})$$

yielding a 2d matrix of size $N_x \times N_y$. More details on WF can be found in the original publication [167]. The WF implementation is online available [171] and has been adapted for near-field measurements for the following simulations.

For the simulations we have used $\text{Fr} = 10^{-3}$ for data generation, image sizes and paddings have been chosen as in Chapter 3. The reconstruction of the cell phantom cf. Fig. 3.2(a) has been carried out for photon fluence $\mu = \{10, 100, 200, 1000, 2000\}$ and the four algorithms RAAR, AP, HIO and WF using the same constraints of pure and negative phase as well as a support constraint.

The input and constraints have been chosen as identical as possible, still each algorithm has some specialties. The starting guess was chosen as amplitude 1 and phase 0. The algorithms have been executed on the same input data, except WF, which needs $L = 21$ measurements. For RAAR we have chosen $\beta_0 = 0.99, \beta_s = 100$ and $\beta_{\text{max}} = 0.4$, HIO has used $\beta = 0.7$ and $D = \sqrt{2/\mu} \cdot 0.65$. AP has no free parameter to choose. WF used the parameters for step length adaption as described above.

Figure B.2 shows the results of the reconstructions after 200 iterations for each algorithm. The reconstructions obtained by RAAR and AP show in this setting the best quality and they are by eyeball norm indistinguishable. In the RAAR/AP reconstructions the medium-sized compartments of the phantom are already distinguishable at $\mu = 10$. Note, the column with the RAAR results basically reproduces the results of Chapter 3. HIO shows an improvement in quality with increasing μ , but the overall quality lags behind the one of RAAR/AP. For $\mu = 2000$ ph./px. the object reconstructions of HIO shows equal resolution as RAAR/AP but it shows flawed low spatial frequencies. The WF reconstructions start quite noisy, but with increasing μ the noise vanishes. Note, that the fluence has been split up uniformly over all 21 measurements for WF.

As a quantitative measure the Fourier ring correlation (FRC) to the original phantom has been used. Figure B.3 shows the calculated FRC curves. For the calcu-

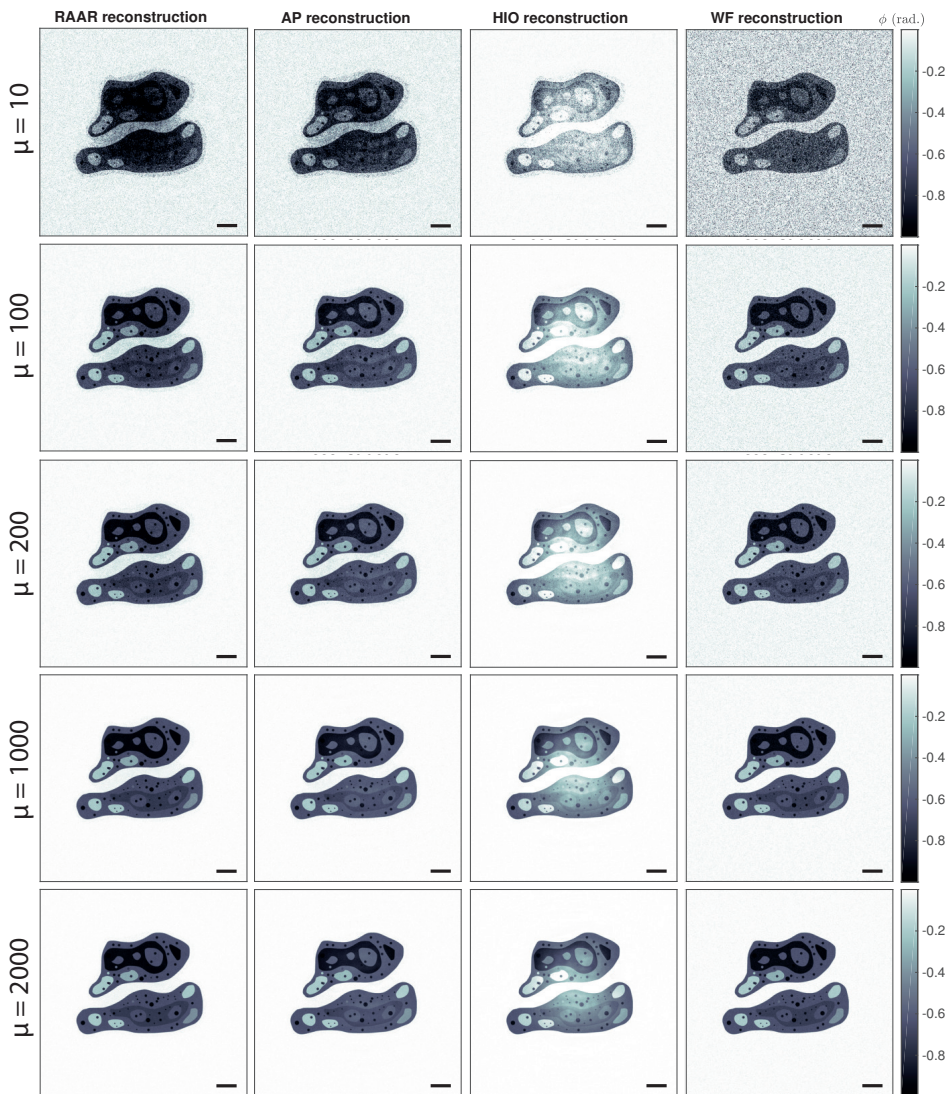


Figure B.2.: Comparison of the reconstruction quality for iterative phase-retrieval methods for varying photon fluence μ (rows). The first columns show the reconstructions obtained by RAAR, HIO, AP and WF, respectively.

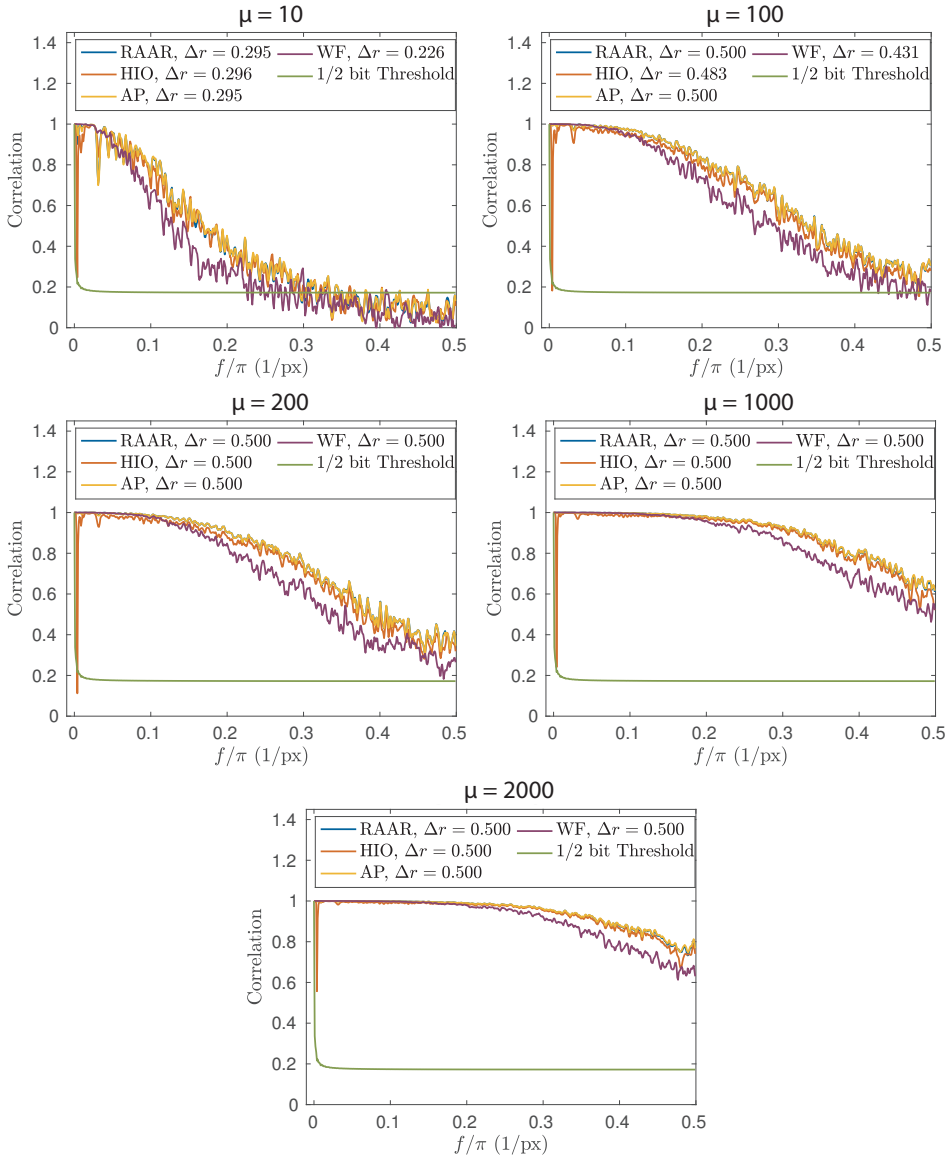


Figure B.3.: The corresponding Fourier ring correlations to the reconstructions shown in Fig. B.2.

lation of this, the values only inside the support have been taken into account. The FRC has for all algorithms a continuous increase in resolution for increased μ . RAAR and AP yield the same high resolution results. HIO yields comparably high resolution but we note a drop in the FRC at low frequencies, as observed in the reconstructions. The visible inspection of the WF reconstructions exhibits no visible difference to RAAR/AP but the FRC reveals that higher spatial frequencies are recovered slightly worse.

The equal quality of RAAR/AP can be explained by the observation, that RAAR acts as accelerator for the reconstruction. RAAR finds the same minimum as AP but with fewer iterations (for certain choice of β). This is illustrated in Fig. B.4 (a,b). In this case RAAR and AP have been iterated only for 30 iterations. The RAAR parameters have been adapted to $\beta_s = 10$ and $\beta_{\max} = 0.5$. The RAAR reconstruction (a) shows at this point already optimal recovery, while the AP reconstruction lacks the lower spatial frequencies. This property is of interest if a large amount of data has to be processed, e.g. a tomographic data set consisting of hundreds of measurements.

Thus a strategy on real data is: First test if a reconstruction with AP works and then use RAAR as an accelerator. If the reconstruction with AP fails, still use RAAR for its better convergence properties.

The experimental feasibility of WF to x-ray imaging seems to be questionable. Since high quality phase masks are required in order to reach high image quality. In the visible regime WF has been applied successfully to Fourier ptychography [172], without the need of masks.

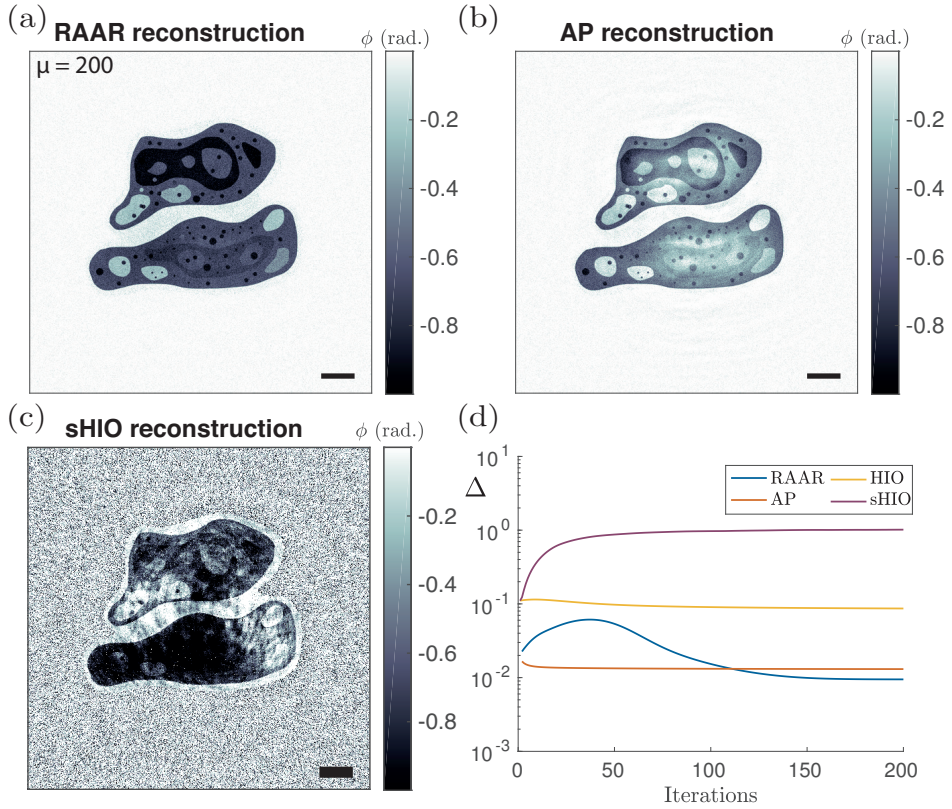


Figure B.4.: Variation of Algorithm parameters at $\mu = 200$ ph./px. (a) and (b) show the object reconstruction after 30 iterations for RAAR and AP, respectively. The RAAR parameter were chosen as $\beta_s = 10$ and $\beta_{\max} = 0.5$. (c) HIO Reconstruction for the standard magnitude projector (sHIO). (d) Comparison of reconstruction errors at $\mu = 200$ ph./px.

C. Matlab Routines

Programming is an art and every artist has its own style. The following describes the structure of a typical simulation script and lists some of the developed functions for MATLAB.

Despite the availability of auto completion for variables there are some commonly used abbreviations in the scripts: ax – axis, tmp – temporary (never trust the value of this variables), p – parameters, pha – phase, amp – amplitude, filt – filter (for an image), holo – hologram, rec(-on) – reconstruction, id – ideal.

The structure of script is given next:

Structure of a typical numerical experiment.

```
%% Setup defaults for matlab
2 % The almighty IRP toolbox
TB_path = '/home/AG_Salditt/Projects_X-ray_Imaging/Toolbox/release/';
4 addpath(genpath(TB_path))
% More defaults for figures
6 ...
%% Set parameters
8 ...
% see below for an example
10 ...
%% Prepare inputs
12 ...
% see section "Data generation" below
14 ...
%% Run simulation / reconstruction
16 ...
% excute a fancy reconstruction algorithm or simulation
18 ...
%% Data analysis/plot results
20 ...
% see section "Data analysis" and "Data presentation" below
```

The values stored in the parameters structure `p` are mostly single value variables. These set a certain physical parameter or toggle a specific action during the numerical experiment. `p` is used throughout the scripts.

An exemplary collection of parameters p.

```

%% Simulation parameters
2 % Size of the actual phantom image
  p.width = 512;
4 p.height = 512;
  % Padding for e.g. data generation
6 p.width2 = 2048;
  p.height2 = 2048;
8 % The actual reconstruction size can differ again.
  p.rec_width = 1024;
10 p.rec_height = 1024;

12 % Fresnel number
  p.F = 1e-3;
14
  % fluence for Poisson noise
16 p.num_photons = 10;

18 % RAAR algorithm parameters
  p.b_0 = 0.99;
20 p.b_m = 0.75;
  p.b_s = 150;
22 p.num_iterations = 200;

24 % support mask
  p.supp = ones(p.rec_height, rec_width);
26
  % Amp_valid is a mask to discriminate deffect pixels (real data...)
28 p.Amp_valid = logical(true(p.rec_height, p.rec_width));

```

C.1. List of Routines

Data generation

This list contains some functions to setup wave fields and simulate multiple distance holographic data sets.

```
[beam] = prepare_probe(pha_path, amp_path, lower_phase, upper_phase,
  lower_amp, upper_amp, p, gauss_filt_fwhm)
```

This function prepares a wave field (probe or object) from two given images. The function reads the images from the given paths and converts them to gray scale. The gray values are interpreted as amplitude and phase in the given

ranges. The images are scaled to size $p.height \times p.width$ px² and then smoothly padded with `pad_fadeout`. The output is of size $p.height2 \times p.width2$.

Example:

```
probe = prepare_probe([TB_path, 'phantoms/mandrill.png'], [TB_path, 'phantoms/
durer.png'], -0.4, 0.4, 0.8, 1.2, p, 1); % the authors preferred choice
```

```
[f_constraints] = multiple_beam_distances(object, probe, F, p, weights, noise)
```

This function simulates measurements for the given wave fields `object` and `probe` at multiple Fresnel numbers `F`. `probe` is a cell-array for a multi modal probe. `weights` holds the occupation numbers for the modes. `noise` is a boolean to switch on noise measurements. The number of photons per pixel is given via `p.num_photons`.

Example:

```
f_constraints = multiple_beam_distances(sample, probe, p.F, p, p.mode_weight,
p.use_noise);
```

```
PropagatorGPU(fresnelx, fresnely, nx, ny, f)
```

`PropagatorGPU` implements the Fresnel propagator given in Eq. 1.2. It is a class returning an object of type `PropagatorGPU`. The calculation is carried out by calling an external CUDA-kernel. It is possible, that the kernel needs recompiling, then the script `toolbox/propagators/compile_kernel.sh` needs to be run. The parameter `f` chooses a padding factor for the propagation. Note: due to the limited RAM on a GPU be careful with large ($n_x > 8192$ px) arrays. This can change with future hardware. A CPU variant with the same behavior is thus available under the name `Propagator`.

Example:

```
prop = PropagatorGPU(1e-3, 1e-3, 2048, 2048, 2); % only once
sample = phantom(2048);
holo = prop.propTF(sample); % can be used as often as needed
```

```
res = pad_fadeout(im_in, N_out, transition_length, padval, method)
```

This function has been written by *Simon Marezke*. It smoothly pads a given image `im_in` to the size `N_out`, given as tuple. The transition length can be chosen in units of pixels by `transition_length` and the target value after the transition zone by `padval`.

Example:

```
padded_img = pad_fadeout(amp, [p.height2, p.width2],(p.width2-p.width)*0.03, 1)
```

```
out = mid(in, m, n) OR out = mid(in, p)
```

This function returns the middle quadrant of size $m \times n$ of an image $M \times N$ image. In a second form `mid` takes the parameter object `p`

Example:

```
A = rand(2048);  
B = mid(A, 512, 512);
```

```
out = copy_mid(im1, im2, m, n)
```

This function copies the $m \times n$ middle pixels of matrix `im1` to the $m \times n$ middle pixels of matrix `im2`.

Example:

```
a = randn([6 6]); b = randn([6 6]);  
copy_mid(a,b, 2,2);
```

Data analysis

The functions presented here are used to calculate metrics on a reconstruction or input data.

```
offsets = find_phase_offset_for_modes(recons, phantom, p)
```

This function determines the global phase offset from a reconstruction `recons` to a given phantom `phantom`. By minimizing the ℓ^2 difference with the use of `lsqnonlin`.

Example:

```
offsets = find_phase_offset_for_modes(reconstruction, probe, p);
```

```
[stat] = analyze_noise(method)
```

This function analyzes the noise in the current figure. It calculates the histogram and Gaussian fit for an image region selected by mouse. It returns a histogram plot and statistics (max, mean, standard deviation and FWHM). `method` chooses the fit type (`hist`, `gaussian` or `poisson`);

Example:

```
figure; imagesc(imnoise(uint16(ones(2048)*200), 'poisson'))
analyze_noise
```

```
[J, g, counter, d_range, time] = calc_J2(mode1, F, norm, p)
```

This function calculates the mutual optical intensity J Eq. (4.4) on a given mode `mode1`. By the choice of `F` the propagated J can be calculated. The result can be normalized or not (`norm`). In order to get J for an ensemble of modes, J has to be calculated for each mode and summed.

Example:

```
A = rand(p.width); F = inf; % no propagation
[J, g, counter, d_range, time] = calc_J2(A, F, 'norm', p);
```

```
[g_ges, counter_ges] = calc_g_from_J(J, bin_size, x1_start, x1_end, p)
```

This function takes J as input and carries out the normalization to yield g or j as defined by Eq. (4.5). Next the binning of values for bins of size `bin_size` is carried out. `x1_start`, `x1_end` give start and end index, respectively, for the computation. This can be `x1_start = 1`, `x1_end = p.width`, that calculation can take a while. An efficient way of evaluating this function is shown in the example.

Example:

This example is more complex, but it demonstrates the efficient parallel evaluation of this function, making use of `parfeval`.

```

jj = 1; % counts currently running evaluations
2 max_num_evaluations = 10; %maximal number of concurrent
  evaluations
pool = parpool(max_num_evaluations); % pool of workers
4 pctRunOnAll maxNumCompThreads(5) %number of threads per
  evaluation
chunk_size = 13;
6 x1_start = 1:chunk_size:p.width;
  x1_end = chunk_size:chunk_size:p.width;
8 if(x1_end(end) ~= p.width)
  x1_end = [x1_end p.width];
10 end
for ii = 1:numel(x1_start)
12   if(jj < max_num_evaluations)
     f(jj) = parfeval(pool, @calc_g_from_J, 2, J, bin_size,
x1_start(ii), x1_end(ii), p);
14     jj = jj + 1;
  else
16     fprintf('fetching results\n')
     for idx = 1:numel(f)
18         [completedIdx, this_g, this_counter] = fetchNext(f);
         counter_ges = counter_ges + this_counter;
20         g_ges = g_ges + this_g;
     end
22     jj = 1;
  end
24 end

```

The for-loop in line 11 runs over all chunks of 1 to `p.width`, here `x1_start`. If fewer evaluations than `max_num_evaluations` run, a new evaluation is started (line 13). If the maximum number of evaluations is reached we wait and fetch results (line 17) with `fetchNext` and add these to the global results `counter_ges`, `g_ges`. The evaluations counter is reset in line 22 then we continue with the next batch of calculations.

```
[result, goodness_of_fit]=fit_gauss(x, y, domain, FWHM_g, b, mu, za, zc, show_plot)
```

MATLAB's standard Gaussian fit model is not that, one wants to use in most cases. `fit_gauss` sets up a fit according to the function

$$f(\text{FWHM_g}, b, \mu, z_a, z_c, x) = b \cdot \exp\left(\frac{-(x - \mu)^2 \cdot 8 \cdot \log(2)}{\text{FWHM_g}^2}\right) + z_a \cdot x + z_c,$$

this is a fit of a Gaussian function depending on the full width at half maximum (FWHM), not the standard deviation, with linear $z_a \cdot x$ and constant offset z_c . The function requires as inputs the x -coordinates x and corresponding measured values y . Data points outside `domain = [x_min x_max]` will be excluded from the fit. `b`, `mu`, `za`, `zc` can be optionally used to pass initial guesses for these parameters.

Example:

```
fit_foc = fit_gauss(x', data', [-3 3], 1.6645, 1, 0, 0, 0, p.show);
```

Data presentation

The following functions are used for data presentation.

```
len = jscalebar(length, pixelsize, posx, posy, color, sbtext)
```

This function adds a scale bar to figures. The coordinates `posx`, `posy` are given relative to the figure's size, thus it is insensitive to size changes. Length and pixel size have the same unit e.g. 5 μm =5000 nm in 10 nm pixel. `sbtext` adds a label to the scale bar. The `color` is given in standard MATLAB specifiers.

Example:

```
figure; imagesc(rand(2048));
jscalebar(100, 1, 0.95, 0.95, 'w'); %scale bar of 100 px
```

```
colorbar_label(label, varargin)
```

Adds a label to the colorbar in the current figure. While changing the color bar label has become comparatively easy in recent MATLAB versions, it still requires some code for each figure. This function encapsulates these code snippets and makes them reusable. `label` contains the (L^AT_EX-)label string. `varargin` controls properties of the label for example: `FontSize`, `position` (in pt.), `HorizontalAlignment`. Properties are given as property-value pair, the list of supported properties can be extended.

Example:

```
figure; imagesc(rand(512));
colorbar_label('$\phi$ (rad.)');
```

```
side_by_side(im1, im2, varargin)
```

`side_by_side` plots two images vertically or horizontally next to each other. This is well suited for comparisons. `im1` is the left/upper and `im2` the right/lower half of the composite image. `varargin` controls properties of the figure for example: `range` (tuple of lower and upper percentile of plotted value range), `orientation` (h,v), `lw` (line width of separator), `line_position` (percent of image), `figure_handle` (for reuse of figure). Properties are given as property-value pair, the list of supported properties can be extended.

Example:

```
side_by_side(rand(512), rand(512)) % standard options
side_by_side(rand(512), rand(512), 'range', [20 80], 'orientation', 'v', 'lw',
3, 'line_position', 0.3)
```


C.2. Implementation of RAAR

Here the implementation of RAAR with near-field propagation is shown which has been used for reconstruction in App. B. The actual algorithm has a length of only a few lines, but the actual implementation is, as always, lengthened by initializations, error control, etc. In the implementation shown below the projections and in particular the constraints (pure phase constraint and single distance magnitude constraint) are hard coded. The structure of the projection algorithms written in fix point notation shows already, that they are perfectly suited for a templated implementation. This allows easy substitution of constraints without rewriting the algorithm, which can basically stay untouched. In MATLAB this can be achieved by implementing the projectors as functions and then calling these via `feval`. An implementation of this approach exists in the ProxToolbox [173].

The C++ approach to this problem is to use templated classes with the projectors implemented as functors. This framework is called T-RAX (templated reconstruction algorithms for x-ray imaging) [174].

MATLAB implementation of RAAR as it has been used for the simulations in App. B.

```

function [result, error, gap] = RAAR_nf(M, psi, iterations, F, p)
2 % inputs:
% M           - measurement (amplitudes)
4 % psi        - initial guess
% iterations  - number of iterations
6 % F          - Fresnel number for propagation
% p           - parameters
8 if(isfield(p, 'progress_bar') == 1)
    if p.progress_bar
10     h = waitbar(0, 'progress');
        progress_bar = 1;
12     else
        progress_bar = 0;
14     end
else
16     h = waitbar(0, 'progress');
        progress_bar = 1;
18 end

20 % errors & gap
error = (zeros(iterations, 1));
22 gap = (zeros(iterations, 1));
% get input arrays and put them on GPU
24 M = gpuArray(M);
M_squared = (M.^2); % measured intensity - for error calc

```

```

26 %is used in support constraint to ensure energy conservation
mean_amplitude = mean(M(:));
28 supp = gpuArray(logical(p.supp));

30 % Amp_valid can be used to discriminate bad pixels
Amp_valid = gpuArray(p.Amp_valid);
32 psi = gpuArray(psi);
P_S = psi;
34

% Propagator objects
36 if(isfield(p,'oversample') == 0)
    warning('using default oversampling factor = 1.');
```

38 oversample = 1;

```

else
40     oversample = p.oversample;
end
42 prop = PropagatorGPU(F, F, size(M,2), size(M,1), oversample);
prop_back = PropagatorGPU(-F, -F, size(M,2), size(M,1), oversample);
44

%relaxation parameters
46 b_0 = p.b_0; b_m = p.b_m; b_s = p.b_s;

48 for ii = 1:iterations
    if progress_bar
50     waitbar(ii / iterations, h, ...
        sprintf('%d / %d',ii, iterations));
52     end
    % relaxation parameter for current iteration
54     b = exp(-(ii/b_s)^3)*b_0 + (1 - exp(-(ii/b_s)^3))*b_m;
    psi_old = psi;
56     % P_M
    psi = prop.propTF(psi);
58

    % calculation of measurement error
60     if(isfield(p,'do_errors') == 1)
        if p.do_errors == 1
62             if ii > 1
                err_val = ...
64                 norm(mid(P_M,p)-(mid(P_S,p)), 'fro')./(p.height*p.width);
                err_val = sqrt(err_val);
66                 error(ii) = gather(err_val);
            else
68                 error(ii) = 0;
                end
70             end
        end
72     % carry out adaption on measurements

```

```

74     psi(Amp_valid) = M(Amp_valid) .* exp(1i.*angle(psi(Amp_valid)));
75     P_M = prop_back.propTF(psi);
76
77     % calculation of gap
78     if(isfield(p,'do_errors')== 1)
79         if ii > 1 %calculation of gap, actually this is the valuefor
80         the last iteration
81             % project on S - pure phase constraint
82             P_S(supp) = mean_amplitude .* exp(1i.*angle(P_M(supp)));
83             % support and negativity constraint
84             P_S(~supp | angle(P_M) > 0) = mean_amplitude;
85             % gap = |P_M(psi) - P_S(psi)|
86             err_val = ...
87                 norm(mid(P_M,p)-(mid(P_S,p)),'fro')./(p.height*p.width);
88             err_val = sqrt(err_val);
89             gap(ii) = gather(err_val);
90         end
91     end
92     % Reflection on M
93     R_M = 2 * P_M - psi_old;
94     % project S - pure phase constraint
95     psi(supp) = mean_amplitude .* exp(1i.*angle(R_M(supp)));
96     % support and negativity constraint
97     psi(~supp | angle(psi) > 0) = mean_amplitude;
98     % Reflect on S
99     psi = 2*psi - R_M;
100    % new RAAR iterate
101    psi = (b/2) * (psi + psi_old) + (1-b)*P_M;
102    end
103    % final projection on M P_M
104    psi = prop.propTF(psi);
105    psi(Amp_valid) = M(Amp_valid) .* exp(1i.*angle(psi(Amp_valid)));
106    psi = prop_back.propTF(psi);
107    result = gather(psi);
108    if progress_bar
109        close(h);
110    end
111    end

```


Bibliography

- [1] M. Osterhoff. “Wave optical simulations of x-ray nano-focusing optics”. PhD thesis. Universität Göttingen, 2012.
- [2] T. Salditt, M. Osterhoff, M. Krenkel, R. N. Wilke, M. Priebe, M. Bartels, S. Kalbfleisch, and M. Sprung. “Compound focusing mirror and X-ray waveguide optics for coherent imaging and nano-diffraction”. In: *J. Synchrotron Rad.* 22.4 (2015), pp. 867–878.
- [3] H. Neubauer. “Ein Verfahren zur Herstellung zweidimensionaler Röntgenwellenleiter”. PhD thesis. Universität Göttingen, 2012.
- [4] S. Hoffmann-Urlaub. “X-ray waveguide optics: Beyond straight channels”. PhD thesis. Universität Göttingen, 2016.
- [5] D. Gabor. “A New Microscopic Principle”. In: *Nature* 161 (1948), pp. 777–778.
- [6] K. Giewekemeyer. “A study on new approaches in coherent x-ray microscopy of biological specimens”. PhD thesis. Georg-August University School of Science (GAUSS) Göttingen, 2011.
- [7] M. Bartels. “Cone-beam x-ray phase contrast tomography of biological samples Optimization of contrast, resolution and field of view”. PhD thesis. Universität Göttingen, 2013.
- [8] M. Krenkel. “Cone-beam x-ray phase-contrast tomography for the observation of single cells in whole organs”. PhD thesis. Universität Göttingen, 2015.
- [9] A.-L. Robisch. “Phase retrieval for object and probe in the optical near-field”. PhD thesis. Universität Göttingen, 2016.
- [10] D. R. Luke. “Phase Retrieval, What’s New?” In: *SIAM SIAG/OPT Views and News* 25.1 (2017), pp. 1–6.
- [11] W. Hoppe. “Beugung im inhomogenen Primärstrahlwellenfeld. I. Prinzip einer Phasenmessung von Elektronenbeugungsinterferenzen”. In: *Acta Crystallogr. A* 25.4 (1969), pp. 495–501.

- [12] P. Thibault, M. Dierolf, A. Menzel, O. Bunk, C. David, and F. Pfeiffer. “High-Resolution Scanning X-ray Diffraction Microscopy”. In: *Science* 321.5887 (2008), pp. 379–382.
- [13] M. Stockmar, P. Cloetens, I. Zanette, B. Enders, M. Dierolf, F. Pfeiffer, and P. Thibault. “Near-field ptychography: phase retrieval for inline holography using a structured illumination”. In: *Sci. Rep.* 3 (2013), p. 1927.
- [14] A.-L. Robisch, K. Kröger, A. Rack, and T. Salditt. “Near-field ptychography using lateral and longitudinal shifts”. In: *New J. Phys.* 17.7 (2015), p. 073033.
- [15] R. N. Wilke, M. Priebe, M. Bartels, K. Giewekemeyer, A. Diaz, P. Karvinen, and T. Salditt. “Hard X-ray imaging of bacterial cells: nano-diffraction and ptychographic reconstruction”. In: *Opt. Express* 20.17 (2012), pp. 19232–19254.
- [16] M. Krenkel, M. Töpferwien, M. Bartels, P. Lingor, D. Schild, and T. Salditt. “X-ray phase contrast tomography from whole organ down to single cells”. In: *Proc. SPIE* 9212 (2014), 92120R.
- [17] J. Miao, P. Charalambous, J. Kirz, and D. Sayre. “Extending the methodology of X-ray crystallography to allow imaging of micrometre-sized non-crystalline specimens”. In: *Nature* 400.6742 (1999), pp. 342–344.
- [18] G. Kellström. “Experimentelle Untersuchungen über Interferenz- und Beugungserscheinungen bei langwelligen Röntgenstrahlen”. *Nova acta Regiae Societatis Scientiarum Upsaliensis*. PhD thesis. University of Uppsala, 2016.
- [19] S. Aoki and S. Kikuta. “X-Ray Holographic Microscopy”. In: *Japanese J. Appl. Phys.* 13.9 (1974), p. 1385.
- [20] P. Cloetens, W. Ludwig, J. Baruchel, D. Van Dyck, J. Van Landuyt, J. P. Guigay, and M. Schlenker. “Holotomography: Quantitative phase tomography with micrometer resolution using hard synchrotron radiation x rays”. In: *Appl. Phys. Lett.* 75.19 (1999), pp. 2912–2914.
- [21] P. Kirkpatrick and A. V. Baez. “Formation of Optical Images by X-Rays”. In: *J. Opt. Soc. Am.* 38.9 (1948), pp. 766–773.
- [22] A. Snigirev, V. Kohn, I. Snigireva, A. Souvorov, and B. Lengeler. “Focusing high-energy x rays by compound refractive lenses”. In: *Appl. Opt.* 37.4 (1998), pp. 653–662.

- [23] C. G. Schroer and G. Falkenberg. “Hard X-ray nanofocusing at low-emittance synchrotron radiation sources”. In: *J. Synchrotron Rad.* 21.5 (2014), pp. 996–1005.
- [24] F. Seiboth et al. “Perfect X-ray focusing via fitting corrective glasses to aberrated optics”. In: *Nat. Commun.* 8 (2017), p. 14623.
- [25] M. Altarelli et al. “The European X-Ray Free-Electron laser: Technical Design Report”. In: *European XFEL project team, Hamburg, Germany* (2007).
- [26] C. Pellegrini. “The history of X-ray free-electron lasers”. In: *Eur. Phys. J. H* 37.5 (2012), pp. 659–708.
- [27] E. Allaria et al. “The FERMI seeded-FEL facility: Status and perspectives”. In: *AIP Conf. Proc.* 1741.1 (2016), p. 020006.
- [28] T. Ishikawa et al. “A compact X-ray free-electron laser emitting in the sub-angstrom region”. In: *Nat Photon* 6.8 (2012), pp. 540–544.
- [29] P. F. Tavares, S. C. Leemann, M. Sjöström, and Å. Andersson. “The MAXIV storage ring project”. In: *J. Synchrotron Rad.* 21.5 (2014), pp. 862–877.
- [30] Z. Huang and R. D. Ruth. “Laser-Electron Storage Ring”. In: *Phys. Rev. Lett.* 80 (5 1998), pp. 976–979.
- [31] E. Eggl, S. Schleede, M. Bech, K. Achterhold, R. Loewen, R. D. Ruth, and F. Pfeiffer. “X-ray phase-contrast tomography with a compact laser-driven synchrotron source”. In: *Proc. Natl. Acad. Sci. U.S.A.* 112.18 (2015), pp. 5567–5572.
- [32] W. S. Graves, F. X. Kärtner, D. E. Moncton, and P. Piot. “Intense Super-radiant X Rays from a Compact Source Using a Nanocathode Array and Emittance Exchange”. In: *Phys. Rev. Lett.* 108 (26 2012), p. 263904.
- [33] R. Neutze, R. Wouts, D. van der Spoel, E. Weckert, and J. Hajdu. “Potential for biomolecular imaging with femtosecond X-ray pulses”. In: *Nature* 406.6797 (2000), pp. 752–757.
- [34] G. Schmahl, D. Rudolph, B. Niemann, and O. Christ. “Zone-plate X-ray microscopy.” In: *Q. Rev. Biophys.* 13.3 (1980), pp. 297–315.
- [35] C. Eberl et al. “Fabrication of laser deposited high-quality multilayer zone plates for hard X-ray nanofocusing”. In: *Appl. Surf. Sci.* 307.0 (2014), pp. 638–644.
- [36] M. Osterhoff, C. Eberl, F. Döring, R. N. Wilke, J. Wallentin, H.-U. Krebs, M. Sprung, and T. Salditt. “Towards multi-order hard X-ray imaging with multilayer zone plates”. In: *J. Appl. Crystallogr.* 48.1 (2015).

- [37] R. Barrett, R. Baker, P. Cloetens, C. Morawe, R. Tucoulou, and A. Vivo. “Reflective Optics for Hard X-ray Nanofocusing Applications at the ESRF”. In: *Synchrotron Radiation News* 29.4 (2016), pp. 10–15.
- [38] C. G. Schroer, O. Kurapova, J. Patommel, P. Boye, J. Feldkamp, B. Lengeler, M. Burghammer, C. Riekel, L. Vincze, A. van der Hart, et al. “Hard x-ray nanoprobe based on refractive x-ray lenses”. In: *Appl. Phys. Lett.* 87.12 (2005), p. 124103.
- [39] F. Pfeiffer, C. David, M. Burghammer, C. Riekel, and T. Salditt. “Two-Dimensional X-ray Waveguides and Point Sources”. In: *Science* 297.6, 063709 (2002), p. 230.
- [40] M. Born and E. Wolf. *Principles of optics: electromagnetic theory of propagation, interference and diffraction of light*. Cambridge University Press, 1999.
- [41] D. J. Griffiths. *Introduction to Electrodynamics*, 3rd ed. Prentice Hall, Upper Saddle River, New Jersey, 1999, p. 576.
- [42] J. D. Jackson. *Classical electrodynamics*. Wiley, 1999.
- [43] J. W. Goodman. *Introduction to Fourier Optics*. Roberts & Company: Englewood, Colorado, 2005.
- [44] D. M. Paganin. *Coherent X-Ray Optics*. New York: Oxford University, 2006.
- [45] *CXRO - The Center for X-ray Optics*. <http://cxro.lbl.gov/>. 2017.
- [46] G. Schmahl, D. Rudolph, and P. Guttman. “Phase Contrast X-Ray Microscopy – Experiments at the BESSY Storage Ring”. In: *X-ray microscopy II*. Springer, 1988, pp. 228–232.
- [47] F. Zernike. “Das Phasenkontrastverfahren bei der mikroskopischen Beobachtung”. In: *Z. tech. Phys* 16 (1935), pp. 454–457.
- [48] T. Butz. *Fouriertransformation für Fußgänger*. Vieweg+Teubner Verlag / Springer Fachmedien Wiesbaden GmbH, Wiesbaden, 2012.
- [49] D. G. Voelz and M. C. Roggemann. “Digital simulation of scalar optical diffraction: revisiting chirp function sampling criteria and consequences”. In: *Appl. Opt.* 48.32 (2009), pp. 6132–6142.
- [50] D. Voelz. *Computational Fourier Optics: A MATLAB tutorial*. Vol. TT89. Tutorial Texts in Optical Engineering. SPIE - the International Society for Optical Engineering, 2011.

- [51] L. Melchior. *PyPropagate*. <https://github.com/TheLartians/PyPropagate>. 2016.
- [52] V. Katkovnik, A. Migukin, and J. Astola. “Backward discrete wave field propagation modeling as an inverse problem: toward perfect reconstruction of wave field distributions”. In: *Appl. Opt.* 48.18 (2009), pp. 3407–3423.
- [53] J. Hagemann, A.-L. Robisch, D. R. Luke, C. Homann, T. Hohage, P. Cloetens, H. Suhonen, and T. Salditt. “Reconstruction of wave front and object for inline holography from a set of detection planes”. In: *Opt. Express* 22.10 (2014), pp. 11552–11569.
- [54] C. Homann, T. Hohage, J. Hagemann, A.-L. Robisch, and T. Salditt. “Validity of the empty-beam correction in near-field imaging”. In: *Phys. Rev. A* 91 (1 2015), p. 013821.
- [55] R. Mokso, P. Cloetens, E. Maire, W. Ludwig, and J. Buffiere. “Nanoscale zoom tomography with hard x rays using Kirkpatrick-Baez optics”. In: *Appl. Phys. Lett.* 90 (2007), p. 144104.
- [56] M. Krenkel, A. Markus, M. Bartels, C. Dullin, F. Alves, and T. Salditt. “Phase-contrast zoom tomography reveals precise locations of macrophages in mouse lungs”. In: *Sci. Rep.* 5 (2015), p. 09973.
- [57] M. Bartels, M. Krenkel, P. Cloetens, W. Möbius, and T. Salditt. “Myelinated mouse nerves studied by X-ray phase contrast zoom tomography”. In: *J. of Structural Biology* (2015), pp. –.
- [58] J. Stangl, C. Mocuta, V. Chamard, and D. Carbone. *Nanobeam X-ray Scattering: Probing matter at the nanoscale*. John Wiley & Sons, 2013.
- [59] A. M. Maiden and J. M. Rodenburg. “An improved ptychographical phase retrieval algorithm for diffractive imaging”. In: *Ultramicroscopy* 109.10 (2009), pp. 1256–1262.
- [60] P. Thibault, M. Dierolf, O. Bunk, A. Menzel, and F. Pfeiffer. “Probe retrieval in ptychographic coherent diffractive imaging”. In: *Ultramicroscopy* 109.4 (2009), pp. 338–343.
- [61] A. Schropp et al. “Hard x-ray nanobeam characterization by coherent diffraction microscopy”. In: *Appl. Phys. Lett.* 96.9 (2010), p. 091102.
- [62] C. M. Kewish et al. “Reconstruction of an astigmatic hard X-ray beam and alignment of K-B mirrors from ptychographic coherent diffraction data”. In: *Opt. Express* 18.22 (2010), pp. 23420–23427.

- [63] D. J. Vine, G. J. Williams, B. Abbey, M. A. Pfeifer, J. N. Clark, M. D. de Jonge, I. McNulty, A. G. Peele, and K. A. Nugent. “Ptychographic Fresnel coherent diffractive imaging”. In: *Phys. Rev. A* 80.6 (2009), p. 063823.
- [64] S. Marchesini, H. Krishnan, D. A. Shapiro, T. Perciano, J. A. Sethian, B. J. Daurer, and F. R. Maia. “SHARP: a distributed, GPU-based ptychographic solver”. In: *arXiv* 1602.01448 (2016).
- [65] M. Stockmar, I. Zanette, M. Dierolf, B. Enders, R. Clare, F. Pfeiffer, P. Cloetens, A. Bonnin, and P. Thibault. “X-Ray Near-Field Ptychography for Optically Thick Specimens”. In: *Phys. Rev. Applied* 3 (1 2015), p. 014005.
- [66] S. Kalbfleisch. “A Dedicated Endstation for Waveguide-based X-Ray Imaging”. PhD thesis. Universität Göttingen, 2012.
- [67] L. Allen and M. Oxley. “Phase retrieval from series of images obtained by defocus variation”. In: *Opt. Commun.* 199 (2001), pp. 65–75.
- [68] L. Loetgering, R. Hammoud, L. Juschkin, and T. Wilhein. “A phase retrieval algorithm based on three-dimensionally translated diffraction patterns”. In: *Europhys. Lett.* 111.6 (2015), p. 64002.
- [69] T. E. Gureyev and K. A. Nugent. “Rapid quantitative phase imaging using the transport of intensity equation”. In: *Optics Communications* 133.1 (1997), pp. 339–346.
- [70] M. Krenkel, M. Bartels, and T. Salditt. “Transport of intensity phase reconstruction to solve the twin image problem in holographic x-ray imaging”. In: *Opt. Express* 21.2 (2013), pp. 2220–2235.
- [71] M. Osterhoff and T. Salditt. “Partially coherent x-ray beam simulations: mirrors and more”. In: *Proceedings of SPIE, the International Society for Optical Engineering*. Society of Photo-Optical Instrumentation Engineers, 2011.
- [72] K. Yamauchi, H. Mimura, K. Inagaki, and Y. Mori. “Figuring with subnanometer-level accuracy by numerically controlled elastic emission machining”. In: *Rev. Sci. Instrum.* 73.11 (2002), pp. 4028–4033.
- [73] D. R. Luke. “Relaxed Averaged Alternating Reflections for Diffraction Imaging”. In: *Inverse Prob.* 21.1 (2005), p. 37.
- [74] D. R. Luke, J. V. Burke, and R. G. Lyon. “Optical wavefront reconstruction: Theory and numerical methods”. In: *SIAM review* 44.2 (2002), pp. 169–224.
- [75] M. Guizar-Sicairos, S. T. Thurman, and J. R. Fienup. “Efficient subpixel image registration algorithms”. In: *Opt. Lett.* 33.2 (2008), pp. 156–158.

- [76] A.-L. Robisch and T. Salditt. “Phase retrieval for object and probe using a series of defocus near-field images”. In: *Opt. Express* 21.20 (2013), pp. 23345–23357.
- [77] P. Langehanenberg, B. Kemper, and G. von Bally. “Autofocus algorithms for digital-holographic microscopy”. In: *Biophotonics 2007: Optics in Life Science*. Optical Society of America, 2007, p. 663313.
- [78] C. G. Schroer, P. Boye, J. M. Feldkamp, J. Patommel, A. Schropp, A. Schwab, S. Stephan, M. Burghammer, S. Schoder, and C. Riekkel. “Coherent X-Ray Diffraction Imaging with Nanofocused Illumination”. In: *Phys. Rev. Lett.* 101.9, 090801 (2008), p. 090801.
- [79] M. Bartels, M. Krenkel, J. Haber, R. N. Wilke, and T. Salditt. “X-Ray Holographic Imaging of Hydrated Biological Cells in Solution”. In: *Phys. Rev. Lett.* 114 (4 2015), p. 048103.
- [80] H. Neubauer, S. Hoffmann, M. Kanbach, J. Haber, S. Kalbfleisch, S. P. Krüger, and T. Salditt. “High aspect ratio x-ray waveguide channels fabricated by e-beam lithography and wafer bonding”. In: *J. Appl. Phys.* 115.21 (2014), p. 214305.
- [81] L. Allen, H. Faulkner, K. Nugent, M. Oxley, and D Paganin. “Phase retrieval from images in the presence of first-order vortices”. In: *Physical Review E* 63.3 (2001), p. 037602.
- [82] Q Shen, I Bazarov, and P. Thibault. “Diffractive imaging of nonperiodic materials with future coherent x-ray sources”. In: *J. Synchrotron Rad.* 11 (2004), pp. 432–438.
- [83] M. Howells et al. “An assessment of the resolution limitation due to radiation-damage in X-ray diffraction microscopy”. In: *Journal of Electron Spectroscopy and Related Phenomena* 170.1-3 (2009), pp. 4–12.
- [84] J. Kirz, D. Sayre, and J. Dilger. “Comparative Analysis of X-ray Emission for Biological Specimen”. In: *Ann. N.Y. Acad. Sci.* 306.1 (1978), pp. 291–305.
- [85] A. Schropp and C. G. Schroer. “Dose requirements for resolving a given feature in an object by coherent x-ray diffraction imaging”. In: *New Journal of Physics* 12.3 (2010), p. 035016.
- [86] R. Henderson. “The potential and limitations of neutrons, electrons and X-rays for atomic resolution microscopy of unstained biological molecules”. In: *Q. Rev. Biophys.* 28.02 (1995), pp. 171–193.

- [87] X. Huang, H. Miao, J. Steinbrener, J. Nelson, D. Shapiro, A. Stewart, J. Turner, and C. Jacobsen. “Signal-to-noise and radiation exposure considerations in conventional and diffraction x-ray microscopy”. In: *Opt. Express* 17.16 (2009), pp. 13541–13553.
- [88] M. R. Howells, J. Kirz, and M. A. Iarocci. “Experiments in x-ray holographic microscopy using synchrotron radiation”. In: *J. Opt. Soc. Am. A* 3.12 (1986), pp. 2171–2178.
- [89] A. Snigirev, I. Snigireva, V. Kohn, S. Kuznetsov, and I. Schelokov. “On the possibilities of x-ray phase contrast microimaging by coherent high-energy synchrotron radiation”. In: *Rev. Sci. Instrum.* 66.12 (1995), pp. 5486–5492.
- [90] I. Robinson and J. Miao. “Three Dimensional Coherent X-ray Diffraction Microscopy”. In: *MRS Bulletin* 29 (2004), pp. 177–181.
- [91] P. Villanueva-Perez, B. Pedrini, R. Mokso, M. Guizar-Sicairos, F. Arcadu, and M. Stampanoni. “Signal-to-noise criterion for free-propagation imaging techniques at free-electron lasers and synchrotrons”. In: *Opt. Express* 24.4 (2016), pp. 3189–3201.
- [92] R. N. Wilke, J. Wallentin, M. Osterhoff, D. Pennicard, A. Zozulya, M. Sprung, and T. Salditt. “High Flux Ptychographic Imaging Using the New 55 μm -Pixel Detector ‘Lambda’ Based on the Medipix3 Readout Chip”. In: *Acta Crystallogr. A* 70 (2014), pp. 552–562.
- [93] M. W. Jones et al. “Rapid, low dose X-ray diffractive imaging of the malaria parasite *Plasmodium falciparum*”. In: *Ultramicroscopy* 143.0 (2014), pp. 88–92.
- [94] V. Elser and S. Eisebitt. “Uniqueness transition in noisy phase retrieval”. In: *New J. Phys.* 13.2 (2011), p. 023001.
- [95] T. Jahn, R. N. Wilke, Y. Chushkin, and T. Salditt. “How many photons are needed to reconstruct random objects in coherent X-ray diffractive imaging?” In: *Acta Crystallogr. A* 73.1 (2017).
- [96] G. Harauz and M. van Heel. “Exact filters for general geometry three dimensional reconstruction”. In: *Proceedings of the IEEE Computer Vision and Pattern Recognition Conf.* Vol. 73. 1986, pp. 146–156.
- [97] M. van Heel and M. Schatz. “Fourier shell correlation threshold criteria”. In: *J. Struct. Biol.* 151.3 (2005), pp. 250–262.

- [98] K. Giewekemeyer, S. P. Krüger, S. Kalbfleisch, M. Bartels, C. Beta, and T. Salditt. “X-ray propagation microscopy of biological cells using waveguides as a quasipoint source”. In: *Phys. Rev. A* 83.2 (2011), p. 023804.
- [99] P. Thibault and A. Menzel. “Reconstructing state mixtures from diffraction measurements”. In: *Nature* 494.7435 (2013), pp. 68–71.
- [100] K. A. Nugent. “The measurement of phase through the propagation of intensity: an introduction”. In: *Contemporary Physics* 52.1 (2011), pp. 55–69.
- [101] L. Mandel and E. Wolf. *Optical Coherence and Quantum Optics*. Cambridge University, 1995.
- [102] B. J. Thompson and E. Wolf. “Two-beam interference with partially coherent light”. In: *J. Opt. Soc. Am.* 47.10 (1957), pp. 895–902.
- [103] J. Cheng and S. Han. “Phase imaging with partially coherent x rays”. In: *Opt. Lett.* 24.3 (1999), pp. 175–177.
- [104] C. T. Koch. “A flux-preserving non-linear inline holography reconstruction algorithm for partially coherent electrons”. In: *Ultramicroscopy* 108.2 (2008), pp. 141–150.
- [105] B. Abbey et al. “Lensless imaging using broadband X-ray sources”. In: *Nat. Photonics* 5.7 (2011), pp. 420–424.
- [106] C. Q. Tran, A. G. Peele, A. Roberts, K. A. Nugent, D. Paterson, and I. McNulty. “Synchrotron beam coherence: a spatially resolved measurement”. In: *Opt. Lett.* 30.2 (2005), pp. 204–206.
- [107] S. Flewett, H. M. Quiney, C. Q. Tran, and K. A. Nugent. “Extracting coherent modes from partially coherent wavefields”. In: *Opt. Lett.* 34.14 (2009), pp. 2198–2200.
- [108] D. Pelliccia, A. Y. Nikulin, H. O. Moser, and K. A. Nugent. “Experimental characterization of the coherence properties of hard x-ray sources”. In: *Opt. Express* 19.9 (2011), pp. 8073–8078.
- [109] T. Salditt, S. Kalbfleisch, M. Osterhoff, S. P. Krüger, M. Bartels, K. Giewekemeyer, H. Neubauer, and M. Sprung. “Partially coherent nano-focused x-ray radiation characterized by Talbot interferometry”. In: *Opt. Express* 19.10 (2011), pp. 9656–9675.
- [110] M. Lyubomirskiy, I. Snigireva, and A. Snigirev. “Lens coupled tunable Young’s double pinhole system for hard X-ray spatial coherence characterization”. In: *Opt. Express* 24.12 (2016), pp. 13679–13686.

- [111] A. Singer, I. A. Vartanyants, M. Kuhlmann, S. Duesterer, R. Treusch, and J. Feldhaus. “Transverse-Coherence Properties of the Free-Electron-Laser FLASH at DESY”. In: *Phys. Rev. Lett.* 101 (2008), p. 254801.
- [112] T. Mey, B. Schäfer, K. Mann, B. Keitel, M. Kuhlmann, and E. Plönjes. “Wigner distribution measurements of the spatial coherence properties of the free-electron laser FLASH”. In: *Opt. Express* 22.13 (2014), pp. 16571–16584.
- [113] D. D. Mai, J. Hallmann, T. Reusch, M. Osterhoff, S. Duesterer, R. Treusch, A. Singer, M. Beckers, T. Gorniak, and T. Senkbeil. “Single pulse coherence measurements in the water window at the free-electron laser FLASH”. In: *Opt. Express* 21.11 (2013), pp. 13005–13017.
- [114] A. S. Ostrovsky. In: *Coherent-Mode Representations in Optics*. SPIE. 2006.
- [115] B. Enders, M. Dierolf, P. Cloetens, M. Stockmar, F. Pfeiffer, and P. Thibault. “Ptychography with broad-bandwidth radiation”. In: *Appl. Phys. Lett.* 104.17 (2014), p. 171104.
- [116] P. M. Pelz, M. Guizar-Sicairos, P. Thibault, I. Johnson, M. Holler, and A. Menzel. “On-the-fly scans for X-ray ptychography”. In: *Appl. Phys. Lett.* 105.25, 251101 (2014).
- [117] D. J. Batey, D. Claus, and J. M. Rodenburg. “Information multiplexing in ptychography”. In: *Ultramicroscopy* 138.0 (2014), pp. 13–21.
- [118] P. Li, T. Edo, D. Batey, J. Rodenburg, and A. Maiden. “Breaking ambiguities in mixed state ptychography”. In: *Opt. Express* 24.8 (2016), pp. 9038–9052.
- [119] M. Bartels, V. H. Hernandez, M. Krenkel, T. Moser, and T. Salditt. “Phase contrast tomography of the mouse cochlea at microfocus x-ray sources”. In: *Appl. Phys. Lett.* 103.8, 083703 (2013), p. 083703.
- [120] M. Töpperwien, M. Krenkel, F. Quade, and T. Salditt. “Laboratory-based x-ray phase-contrast tomography enables 3D virtual histology”. In: *Proc. SPIE* 9964 (2016), p. 99640I.
- [121] D. H. Larsson, W. Vågberg, A. Yaroshenko, A. Ö. Yildirim, and H. M. Hertz. “High-resolution short-exposure small-animal laboratory x-ray phase-contrast tomography”. In: *Sci. Rep.* 6 (2016), p. 39074.
- [122] J. Hagemann, A.-L. Robisch, M. Osterhoff, and T. Salditt. “Probe reconstruction for holographic X-ray imaging”. In: *J. Synchrotron Rad.* 24.2 (2017), pp. 498–505.

- [123] E. Wolf. *Introduction to the Theory of Coherence and Polarization of Light*. Cambridge [u.a.]: Cambridge University, 2007, XIV, 222 S.
- [124] W. H. Press, S. A. Teukolsky, W. T. Vetterling, and B. P. Flannery. *Numerical Recipes : The Art of Scientific Computing*. third. Cambridge University, 2007.
- [125] J. V. Neumann. “On Rings of Operators. Reduction Theory”. In: *Ann. Math.* 50.2 (1949), pp. 401–485.
- [126] NVIDIA Corporation. *CUDA Technology*. <http://www.nvidia.com/>. 2007.
- [127] J. Hagemann. *Reconstructing mode mixtures in the optical near-field: Algorithm and simulation scripts*. <https://doi.org/10.5281/zenodo.581301>. 2017.
- [128] A. Rack, M. Scheel, L. Hardy, C. Curfs, A. Bonnin, and H. Reichert. “Exploiting coherence for real-time studies by single-bunch imaging”. In: *J. Synchrotron Rad.* 21.4 (2014), pp. 815–818.
- [129] A. Schropp et al. “Imaging Shock Waves in Diamond with Both High Temporal and Spatial Resolution at an XFEL”. In: *Sci. Rep.* 5 (2015), p. 11089.
- [130] R. Horisaki, Y. Ogura, M. Aino, and J. Tanida. “Single-shot phase imaging with a coded aperture”. In: *Opt. Lett.* 39.22 (2014), p. 6466.
- [131] P. Tafforeau, R. Boistel, E. Boller, A. Bravin, M. Brunet, Y. Chaimanee, P. Cloetens, M. Feist, J. Hozzowska, and J.-J. Jaeger. “Applications of X-ray synchrotron microtomography for non-destructive 3D studies of paleontological specimens”. In: *Applied Physics A* 83.2 (2006), pp. 195–202.
- [132] B. D. Metscher. “Biological applications of X-ray microtomography: imaging microanatomy, molecular expression and organismal diversity”. In: *Microsc Anal (Am Ed)* 27.2 (2013).
- [133] T. van de Kamp, P. Vagovič, T. Baumbach, and A. Riedel. “A biological screw in a beetle’s leg”. In: *Science* 333.6038 (2011), pp. 52–52.
- [134] J. Moosmann, A. Ershov, V. Altapova, T. Baumbach, M. S. Prasad, C. LaBonne, X. Xiao, J. Kashef, and R. Hofmann. “X-ray phase-contrast in vivo microtomography probes new aspects of *Xenopus* gastrulation”. In: *Nature* 497.497 (2013), pp. 374–377.
- [135] S. Hoffmann-Urlaub, P. Höhne, M. Kanbach, and T. Salditt. “Advances in fabrication of X-ray waveguides”. In: *Microelectron. Eng.* 164 (2016), pp. 135–138.
- [136] M. Osterhoff and T. Salditt. “Coherence filtering of x-ray waveguides: analytical and numerical approach”. In: *New J. Phys.* 13.10 (2011), p. 103026.

- [137] M. Töpperwien, M. Krenkel, K. Müller, and T. Salditt. “Phase-contrast tomography of neuronal tissues: from laboratory-to high resolution synchrotron CT”. In: 9967 (2016), 99670T.
- [138] O. Bunk, M. Dierolf, S. Kynde, I. Johnson, O. Marti, and F. Pfeiffer. “Influence of the overlap parameter on the convergence of the ptychographical iterative engine”. In: *Ultramicroscopy* 108.5 (2008), pp. 481–487.
- [139] J. Rodenburg. “Ptychography and Related Diffractive Imaging Methods”. In: *Advances in Imaging and Electron Physics* Volume 150 (2008). Ed. by Hawkes, pp. 87–184.
- [140] J. Hagemann and T. Salditt. “Reconstructing mode mixtures in the optical near-field”. In: *Opt. Express* 25.13 (2017), pp. 13973–13969.
- [141] J. Hagemann and T. Salditt. “The fluence–resolution relationship in holographic and coherent diffractive imaging”. In: *J. Appl. Crystallogr.* 50.2 (2017), pp. 531–538.
- [142] H. N. Chapman et al. “Femtosecond diffractive imaging with a soft-X-ray free-electron laser”. In: *Nat. Phys.* 2.12 (2006), pp. 839–843.
- [143] H. N. Chapman et al. “Femtosecond X-ray protein nanocrystallography”. In: *Nature* 470.7332 (2011), pp. 73–77.
- [144] J. M. J. Madey. “Stimulated Emission of Bremsstrahlung in a Periodic Magnetic Field”. In: *J. Appl. Phys.* 42.5 (1971), pp. 1906–1913.
- [145] P. Thibault, M. Dierolf, A. Menzel, O. Bunk, C. David, and F. Pfeiffer. “High-Resolution Scanning X-ray Diffraction Microscopy: Supporting Online Material”. In: *Science* 321.5887 (2008), pp. 379–382.
- [146] T. Osaka, M. Yabashi, Y. Sano, K. Tono, Y. Inubushi, T. Sato, S. Matsuyama, T. Ishikawa, and K. Yamauchi. “A Bragg beam splitter for hard x-ray free-electron lasers”. In: *Opt. Express* 21.3 (2013), pp. 2823–2831.
- [147] W. Roseker, H. Franz, H. Schulte-Schrepping, A. Ehnes, O. Leupold, F. Zontone, S. Lee, A. Robert, and G. Grübel. “Development of a hard X-ray delay line for X-ray photon correlation spectroscopy and jitter-free pump-probe experiments at X-ray free-electron laser sources”. In: *J. Synchrotron Rad.* 18.3 (2011), pp. 481–491.
- [148] J. Hagemann and T. Salditt. *Divide and Update: Towards Single-Shot Object and Probe Retrieval for Near-Field Holography: Algorithm and simulation scripts*. <https://doi.org/10.5281/zenodo.838005>. 2017.

- [149] M. V. Heel. “Angular reconstitution: A posteriori assignment of projection directions for 3D reconstruction”. In: *Ultramicroscopy* 21.2 (1987), pp. 111–123.
- [150] A.-L. Robisch, J. Wallentin, A. Pacureanu, P. Cloetens, and T. Salditt. “Holographic imaging with a hard x-ray nanoprobe: ptychographic versus conventional phase retrieval”. In: *Opt. Lett.* 41.23 (2016), pp. 5519–5522.
- [151] G. Kutyniok, W.-Q. Lim, and R. Reisenhofer. “ShearLab 3D: Faithful Digital Shearlet Transforms Based on Compactly Supported Shearlets”. In: *ACM Trans. Math. Softw.* 42.1 (2016), 5:1–5:42.
- [152] S. Looock and G. Plonka. “Phase retrieval for Fresnel measurements using a shearlet sparsity constraint”. In: *Inverse Problems* 30.5 (2014), p. 055005.
- [153] A. Pein, S. Looock, G. Plonka, and T. Salditt. “Using sparsity information for iterative phase retrieval in x-ray propagation imaging”. In: *Opt. Express* 24.8 (2016), pp. 8332–8343.
- [154] M. Stockmar et al. “X-ray nanotomography using near-field ptychography”. In: *Opt. Express* 23.10 (2015), pp. 12720–12731.
- [155] P. Thibault, V. Elser, J. C., S. D., and D. Sayre. “Reconstruction of a yeast cell from X-ray diffraction data”. In: *Act. Cryst. A* 62 (2006), pp. 248–261.
- [156] G. Kutyniok, D. Labate, W.-Q. Lim, M. Leitheiser, R. Reisenhofer, and X. Zhuang. *ShearLab*. <http://www.shearlab.org/>. 2017.
- [157] S. Mallat. *A Wavelet Tour of Signal Processing: The Sparse Way*. 3rd. Academic Press, 2008.
- [158] S. Montresor and P. Picart. “Quantitative appraisal for noise reduction in digital holographic phase imaging”. In: *Opt. Express* 24.13 (2016), pp. 14322–14343.
- [159] S. C. Kramer, J. Hagemann, L. Künneke, and J. Lebert. “Parallel Statistical Multiresolution Estimation for Image Reconstruction”. In: *SIAM J. Sci. Comput.* 38.5 (2016), pp. C533–C559.
- [160] J. C. H. Spence. *High-Resolution Electron Microscopy*. Oxford Press, 2013.
- [161] G. N. Tran, G. A. van Riessen, and A. G. Peele. “Modal approach for partially coherent diffractive imaging with simultaneous sample and coherence recovery”. In: *Opt. Express* 25.10 (2017), pp. 10757–10764.

- [162] K. Moreland. “Diverging Color Maps for Scientific Visualization”. In: *Advances in Visual Computing: 5th International Symposium, ISVC 2009, Las Vegas, NV, USA, November 30-December 2, 2009. Proceedings, Part II*. Ed. by G. Bebis et al. Berlin, Heidelberg: Springer Berlin Heidelberg, 2009, pp. 92–103.
- [163] D. H. Larsson, U. Lundström, U. K. Westermark, M. Arsenian Henriksson, A. Burvall, and H. M. Hertz. “First application of liquid-metal-jet sources for small-animal imaging: High-resolution CT and phase-contrast tumor demarcation”. In: *Medical Physics* 40.2 (2013), p. 021909.
- [164] M. Krenkel, M. Töpperwien, C. Dullin, F. Alves, and T. Salditt. “Propagation-based phase-contrast tomography for high-resolution lung imaging with laboratory sources”. In: *AIP Advances* 6.3, 035007 (2016), p. 035007.
- [165] M. Töpperwien, M. Krenkel, D. Vincenz, F. Stöber, A. M. Oelschlegel, J. Goldschmidt, and T. Salditt. “Three-dimensional mouse brain cytoarchitecture revealed by laboratory-based x-ray phase-contrast tomography”. In: *Sci. Rep.* 7 (2017), p. 42847.
- [166] J. R. Fienup. “Reconstruction of an object from the modulus of its Fourier transform”. In: *Opt. Lett.* 3.1 (1978), pp. 27–29.
- [167] E. J. Candès, X. Li, and M. Soltanolkotabi. “Phase Retrieval via Wirtinger Flow: Theory and Algorithms”. In: *IEEE Transactions on Information Theory* 61.4 (2015), pp. 1985–2007.
- [168] K. Giewekemeyer, P. Thibault, S. Kalbfleisch, A. Beerlink, C. M. Kewish, M. Dierolf, F. Pfeiffer, and T. Salditt. “Quantitative biological imaging by ptychographic x-ray diffraction microscopy”. In: *PNAS* 107.2 (2010), pp. 529–534.
- [169] H. H. Bauschke, P. L. Combettes, and D. R. Luke. “Phase retrieval, error reduction algorithm, and Fienup variants: a view from convex optimization”. In: *J. Opt. Soc. Am. A* 19.7 (2002), pp. 1334–1345.
- [170] H. H. Bauschke, P. L. Combettes, and D. R. Luke. “Hybrid projection-reflection method for phase retrieval”. In: *J. Opt. Soc. Am. A* 20.6 (2003), pp. 1025–1034.
- [171] E. J. Candès, X. Li, and M. Soltanolkotabi. *Wirtinger flow implementation*. <http://www-bcf.usc.edu/soltanol/PRWF.html>. 2015.

-
- [172] Z. Bian, S. Dong, and G. Zheng. “Adaptive system correction for robust Fourier ptychographic imaging”. In: *Opt. Express* 21.26 (2013), pp. 32400–32410.
- [173] R. D. Luke. *ProxToolbox, A toolbox of algorithms and projection operators for implementing fixed point iterations based on the Prox operator*. 2012.
- [174] J. Hagemann. “On the Reconstruction of the Empty Beam in X-Ray Propagation Imaging”. MA thesis. Universität Göttingen, 2013.

Authors Contribution

In this section detailed information about the particular contributions of the author JH in the publications is given. The three peer-reviewed articles reprinted in Chapters 2–4 fulfill the requirements to be considered in a cumulative thesis according to the doctoral degree regulations of the PhD program **ProPhys** in the Georg-August University School of Science (GAUSS) Göttingen:

- (1) J. Hagemann, A.-L. Robisch, M. Osterhoff, and T. Salditt, “Probe Reconstruction for Holographic X-ray Imaging”, *Journal of Synchrotron Radiation* **24**, 2, 498—505 (2017).
- (2) J. Hagemann and T. Salditt, “The Fluence-Resolution Relationship in Holographic and Coherent Diffractive Imaging”, *Journal of Applied Crystallography* **50**, 531—538 (2017).
- (3) J. Hagemann and T. Salditt, “Reconstructing Mode Mixtures in the Optical Near Field”, *Optics Express* **25**, 13973—13969 (2017).

In (1) the probe characterization of the GINIX-setup has been carried out. The experiment was conducted by all authors. In particular ALR performed the measurements and reconstruction for NFP and JH performed the measurements and reconstruction for MMP and data analysis for both schemes. MO supported with experimental instrumentation and data analysis. The results were discussed by all authors of (1). JH (1–3), ALR(1) and TS(1–3) elaborated the physical question and principal design. JH implemented and carried out the simulation and analysis for (1–3). The manuscripts of the publications (1–3) were written by JH and TS.

Own publications

- (1) J. Hagemann and T. Salditt, “Divide and Update: Towards Single-Shot Object and Probe Retrieval for Near-Field Holography”, *Optics Express* **25**, 20953–20968 (2017).
- (2) J. Hagemann and T. Salditt, “Reconstructing Mode Mixtures in the Optical Near Field”, *Optics Express* **25**, 13973–13969 (2017).
- (3) J. Hagemann and T. Salditt, “The Fluence-Resolution Relationship in Holographic and Coherent Diffractive Imaging”, *Journal of Applied Crystallography* **50**, 531–538 (2017).
- (4) J. Hagemann, A.-L. Robisch, M. Osterhoff, and T. Salditt, “Probe Reconstruction for Holographic X-ray Imaging”, *Journal of Synchrotron Radiation* **24**, 2, 498–505 (2017).
- (5) C. Y. J. Hémonnot, C. Ranke, O. Saldanha, R. Graceffa, J. Hagemann, and S. Köster, “Following DNA compaction during the cell cycle by x-ray nanodiffraction”, *ACS Nano* **10**, 10661–10670 (2016).
- (6) S. C. Kramer, J. Hagemann, L. Künneke, and J. Lebert, “Parallel Statistical Multiresolution Estimation for Image Reconstruction”, *SIAM J. Sci. Comput.* **38**, C533–C559 (2016).
- (7) S. C. Kramer and J. Hagemann, “SciPAL: Expression Templates and Composition Closure Objects for High Performance Computational Physics with CUDA and OpenMP”, *ACM Trans. Parallel Comput.* **1**, 1–31 (2015).
- (8) C. Homann, T. Hohage, J. Hagemann, A.-L. Robisch, and T. Salditt, “Validity of the empty-beam correction in near-field imaging”, *Phys. Rev. A* **91**, 013821 (2015).
- (9) J. Hagemann, A.-L. Robisch, D. R. Luke, C. Homann, T. Hohage, P. Cloetens, H. Suhonen, and T. Salditt, “Reconstruction of wave front and object for inline holography from a set of detection planes”, *Opt. Express* **22**, 11552–11569 (2014).
- (10) S. C. Kramer, J. Hagemann, and D. R. Luke, “Real-Time Phase Masks for Interactive Stimulation of Optogenetic Neurons”, arXiv arXiv:1302.0120 (2013).

Danksagung

Zuallererst möchte ich mich bei Prof. Dr. Tim Salditt bedanken. Tim, ohne deinen Einsatz, Interesse und Motivationsvermögen wären Bachelor-, Master- und Doktorarbeit nicht möglich gewesen. Die intensiven, interessanten und auch lustigen Stunden, in denen diese Arbeiten bei Diskussionen und Paper schreiben entstanden sind, sind unzählig. Ich danke Dir für alles, was ich dabei gelernt habe.

Des Weiteren möchte ich Prof. Dr. Russell Luke danken, nicht nur für das Anfertigen des Zweitgutachtens sondern auch für die interessanten Diskussionen über die Tücken der Projektionsalgorithmen.

Bei Prof. Dr. Simone Techert, Prof. Dr. Stefan Dreizler, Prof. Dr. Claus Roppers und Dr. Klaus Mann bedanke ich mich, dass sie sich bereit erklärt und die Zeit genommen haben, der Prüfungskommission beizutreten.

Hat man eine akute Frage, muss man im IRP nicht lange suchen um ein offenes Ohr zu finden, mit dem man diskutieren kann. Danke für diese tolle Atmosphäre! Besonders möchte ich die folgenden Personen hervorheben:

Meinen langjährigen Kollegen Aike Ruhlandt und Jan-David Nicolas danke ich für alle Diskussionen von Bachelor bis Doktor. Mareike Töpferwien und Malte Vassholz danke ich für die Hilfe und Diskussionen, in Bezug auf die praktische Umsetzung und Datenauswertung der Experimente.

Dr. Markus Osterhoff danke ich für die kohärente Klärung wichtiger Fragen von Physik bis Typographie und natürlich auch für die Benutzung der Büchersammlung. Die Zeit unseres „kurzen Dienstweges“ über die Monitore hinweg habe ich sehr genossen.

Aber auch der aktuellen Bürobesetzung Dr. Sophie Charlotte August und Jakob Soltau danke ich für die gute Stimmung und anregende Diskussionen im Büro.

Bei den „Altdoktoranden“ Dr. Anna-Lena Robisch, Dr. Martin Krenkel und Dr. Robin Wilke bedanke ich mich, dass sie mir in Diskussionen ihr Wissen und Erfahrungen weiter gegeben haben.

Jan Goeman danke ich für den IT-Support, ohne laufende Rechenknechte, wäre auch in dieser Arbeit nichts gelaufen.

```
template<typename... Ts> class Danke {};  
Danke<C++, CUDA, gemeinsame Projekte, Grillen> Stephan_Kramer();  
Danke<SciPAL, Rechner fragen> Thomas_Köhler();
```

Ich danke Sabine Balder, Eva Hetzel, Kerstin Pluschke, Michaela Ständer, Christine Wilke-Feist für die Unterstützung bei der Bewältigung administrativer Aufgaben.

Für das Korrekturlesen der Arbeit danke ich Dr. Anna-Lena Robisch, Malte Vassholz und Mareike Töpferwien.

Der Rockharz Crew danke ich für die nötige Ablenkung vor der Abgabe dieser Arbeit 🙌.

Im Weiteren gilt mein Dank auch den Personen, die außerhalb des Instituts mein Leben in den letzten Jahren bereichert haben: den Bogenschützen des Unisports, der Kletter- und Bouldergruppe, Christian Viöl, meiner Familie und Vanessa Rothkegel.

Diese Arbeit wurde aus den Projekten *05K16MGB-WeKokUbs: Wellenfront- und Kohärenzkontrolle an undulatorbasierten Strahlquellen zur Optimierung bildgebender Verfahren* des Bundesministeriums für Bildung und Forschung und DFG *SFB 755 – Nanoscale Photonic Imaging* mit finanziellen Mitteln unterstützt.

Curriculum Vitae

Personal Information

Johannes Hagemann

Born: 07. April 1988 in Hildesheim

Nationality: German

Studies

since 02/2014

Doctoral student in physics,
Institut für Röntgenphysik,
Group of Prof. Tim Salditt
Georg-August-Universität, Göttingen

11/2013

Master's thesis: „On the Reconstruction of the Empty Beam
in X-ray Propagation Imaging”

10/2011 – 11/2013

Master of science in physics with major in biophysics and complex systems
Georg-August-Universität, Göttingen

09/2011

Bachelor's thesis: „Numerical and Experimental Characterization of Coherence in the X-Ray Regime”

10/2008 – 09/2011

Bachelor of science in physics
Georg-August-Universität, Göttingen

08/2000–06/2007

Gymnasium Michelsenschule, Hildesheim